SIMULATION OF AEROTHERMAL AND CHEMICAL CONCENTRATIONS FOR AN RDX EXPLOSION

THESIS

Alison M. Ceranski, Captain, USAF

AFIT-ENY-MS-17-M-250

DEPARTMENT OF THE AIR FORCE
AIR UNIVERSITY

AIR FORCE INSTITUTE OF TECHNOLOGY

Wright-Patterson Air Force Base, Ohio

AFIT-ENY-MS-17-M-250

SIMULATION OF AEROTHERMAL AND CHEMICAL CONENTRATIONS FOR AN RDX EXPLOSION

THESIS

Presented to the Faculty

Department of Aeronautics and Astronautics

Graduate School of Engineering and Management

Air Force Institute of Technology

Air University

Air Education and Training Command

In Partial Fulfillment of the Requirements for the

Degree of Master of Science in Aeronautical Engineering

Alison M. Ceranski, BS, ME

Captain, USAF

March 2017

AFIT-ENY-MS-17-M-250

SIMULATION OF AEROTHERMAL AND CHEMICAL CONCENTRATIONS FOR AN RDX EXPLOSION

Alison M. Ceranski, BS, ME

Captain, USAF

Committee Membership:

Dr. R. B. Greendyke
Chair

Dr. K. C. Gross
Member

Lt Col C. S. Hale, PhD
Member

Dr. B. J. Steward
Member

Abstract

The aerothermal and chemical concentrations of an RDX explosive were simulated using VULCAN, a NASA owned and operated program. The Chapman-Jouguet properties for an RDX explosion were obtained using pure RDX at theoretical maximum density in Cheetah®. The density, temperature, volume, and detonation velocity values obtained from Cheetah® were used to determine the inner radius of the grid used in VULCAN as well as the required time to run the explosive's products into the grid. Four different types of axisymmetric simulations were run in VULCAN. The simulation of 500 kg, 1000 kg, and 2000 kg of RDX using the Runge-Kutta solving scheme were three of those four simulations. The last simulation was of a 500 kg RDX using Diagonalized Approximation Factorization solving scheme.

The aerothermal and chemical results showed several errors in the results. One error was a massive spike in Mach numbers found in all four simulations. The second error was the addition of CO and H_2O in both the 1000 kg and 2000 kg results. However, these errors occurred due to the numerical results not being able to keep up with the physical. In the future, smaller time steps will be required to keep these errors from occurring. The research successfully developed a framework for simulating the aerothermal and chemical concentrations for an explosion.

Acknowledgments

I would like to express my sincere appreciation to my faculty advisor, Dr. Robert Greendyke, for his guidance and support throughout the course of this thesis effort. Thank you for deciding not to retire when you really wanted to. I would, also, like to thank my friends and family for keeping me sane during my time at AFIT.

Alison M. Ceranski

Table of Contents

Page

List of Figures

Page

List of Tables

Page

SIMULATION OF AEROTHERMAL AND CHEMICAL CONCENTRATIONS FOR AN RDX EXPLOSION

I. Introduction

Background

Explosives have become a common topic in today's news. With the help of the Internet, the ingredients and steps needed to build an explosive have become easily accessible. The knowledge about building explosives has allowed terrorist groups such as ISIS to deploy explosive weapons for attacks on coalition forces. In the October 2016 fight for Mosul, Iraq, ISIS used car bombs, improvised explosive devices (IEDs), and suicide bombers to disrupt the advancing Iraqi army and Kurdish Peshmerga fighters [1]. The use of explosives is not something new to war. Since World War I (WWI), artillery has become the dominating force in warfare [2]. With time, the different types of artillery have increased significantly with the aid of new technology. Knowledge regarding enemy force's explosive weapons is a key component to battle strategy that helps to decide a battles victory or defeat. However, the ability to obtain this knowledge first-hand has become difficult. The difficulty in obtaining first-hand knowledge of the enemy's weapons has led to a need for obtaining this information from afar—also known as remote sensing.

Remote sensing is defined as "the acquisition of information about an object without being in physical contact with it. Information is acquired by detecting and measuring changes that the object imposes on the surround field." [3] The Department of Defense (DoD) uses remote sensing to help with battlefield management, battlespace

characterization, technical intelligence, and threat identification [4]. For example, the photographic sensor was first deployed by the United States (US) Army Air Corps in WWI to monitor and establish troop movements [4]. Today, the DoD employs different types of devices to conduct their remote sensing missions. Some of those devices include satellites, unmanned aerial vehicles, and manned aircraft.

After a US military aircraft employs a weapon, it is common operating procedure to remote sense and record the weapon's impact and detonation. These videos are used to analyze if the weapon detonated, hit in the correct location, and destroyed the target. This type of analysis should be taken one step forward. It would be of great benefit to the DoD to use remote sensing, particularly in the infrared spectrum, on explosives created by enemy forces. Looking at the characteristics of the infrared signature could lead to the knowledge of the type of explosive used on the battlefield.

The Need

Sun Tzu said, "If you know the enemy and know yourself you need not fear the results of a hundred battles." [5] A key part of knowing the enemy is understanding the type of weapons they possess. One of the deadliest weapons is one that contains high explosives (HE), because it has high damage to a small-size ratio. With the enemy's ability to create explosives easily, it is important for the DoD to remotely determine which type of explosives the enemy is making and employing.

One problem the military faces in collecting forensic evidence is the opportunity to gather specimens of the exploded weapon. When the weapon explodes, it is often during an altercation or battle, so the warfighter focuses on returning fire and movement

to contact. There is no time to stop and collect any pieces produced from the explosion. After the battle has concluded, there may be time to go back and gather the specimens, but it is often difficult to find the original site and/or the pieces may be mixed with other debris created during the fight.

A second problem the military faces in obtaining information about the explosive used is the ability to gather the remains of the weapon. With HE weapons, shrapnel from the weapon can be scattered a great distance, if in an open area. Metal fragments from an exploding propane tank, which reacts similarly to a HE explosive, have been known to travel up to a half mile away from the source [6]. Additionally, if in a closed area, there is the potential to have a significant amount of debris, created from the explosion, covering the blast zone. These conditions would make it difficult to collect all the relevant pieces required to reverse engineer the weapon.

The ability to ascertain real-time information regarding the enemy's explosives could assist with the battle victory. This knowledge would be important in battlespace characterization. Battlespace characterization is the ability to understand and predict adversary capabilities, tactics, techniques and procedures, threat dispositions, and courses of actions within the context of the operating environment to provide indications and warning, identify potential vulnerabilities to forces, and identify opportunities to achieve combat objectives [7]. Additionally, it could help aid the combat commander in battle management; allowing for a smoothly run operation.

Problem Statement

The need for battlespace characterization and technical intelligence is an important requirement for the DoD and directly affects the warfighter. The simulation of infrared signatures produced from an explosive is an example of battlespace characterization and technical intelligence. It has been experimentally shown that a unique identification technique could provide battlespace knowledge of explosive type (e.g. RDX, TNT, etc.) [4]. The objective of this thesis was to develop a framework for the simulation of aerothermal and chemical concentrations of an explosion.

This thesis will focus on simulating the thermophysics of an explosive's shock wave interacting with the surrounding atmosphere. Specifically, it will look at aerothermal (pressure, temperature, and Mach number) and chemical (CO, CO_2, and H_2O) concentrations throughout time. The explosive's product gasses will create a characteristic hemispherical profile, which results in an infrared signature. Additionally, the DoD's potential uses for this infrared signature will be discussed.

This thesis is an early step in predicting infrared signatures for different explosives, so it will focus on pure cyclonite or hexogen (RDX) as the explosive. RDX was chosen due to being the widest used of the HE [8]. Three different masses of RDX will be simulated to illustrate a difference between the infrared signatures. The three masses were chosen based on trying to deal with a known amount of explosive found in different weapons. It is assumed the explosive is a ground detonation at standard sea-level conditions. Additionally, the explosive is not encased, so there are no metal blast fragments at detonation.

This thesis used several different computer programs to complete the required simulations needed to find the infrared signature. The first step was to determine the initial detonation characteristics from the explosive using Cheetah®, which is a thermochemical code that solves thermodynamic equations to find chemical equilibrium between product species [9]. The program was chosen for its ability to predict detonation performance. These characteristics (e.g. temperature and detonation velocity) were used for the starting condition of the shock wave when propagating outwards. VULCAN was used to simulate and determine the aerothermal and chemical interactions that occurred after detonation of the explosive. VULCAN is a turbulent, non-equilibrium, finite-rate chemical kinetics, Navier-Stokes flow solver [10]. The grid created to capture the characteristic hemispherical profile was made in Pointwise®, which is mesh generating software for use in computational fluid dynamics problems. Finally, the results from VULCAN were displayed in Tecplot 360® to visualize the aerothermal and chemical concentrations throughout time.

Preview

This chapter provided an overview of what the thesis will entail, and why it is important to pursue the research. Chapter II will provide a literature review and demonstrate the gaps in knowledge that this thesis will help fill. Chapter III will discuss in detail the method used to simulate the aerothermal and chemical concentrations of an RDX explosive. Chapter IV presents and analyzes the results from the simulations. Chapter V will state conclusions and offer recommendations for future study.

II. Literature Review

Chapter Overview

The purpose of this chapter is to describe the known information relative to explosives, computer programs used, infrared, and detonation signatures. This chapter will also discuss the gaps found in these areas that are needed to simulate an explosive shock wave moving through the air. The first section describes the basics of explosives. Additionally, it will discuss shock waves and their propagation through air. The second section describes how Cheetah® and VULCAN operate. The third section describes the principles behind infrared technology. The final section addresses the ability to detect detonation signatures.

Explosives

Explosions involve chemistry and physics under extreme conditions and are mechanistically complex [4]. The most common type of explosives used are organic rather than inorganic. Organic, or CHNO, explosives consist of four basic building blocks: carbon, hydrogen, nitrogen, and oxygen. RDX ($C_3H_6N_6O_6$) is a common example of an organic explosive. The structure of the RDX molecule is shown in Figure 1.

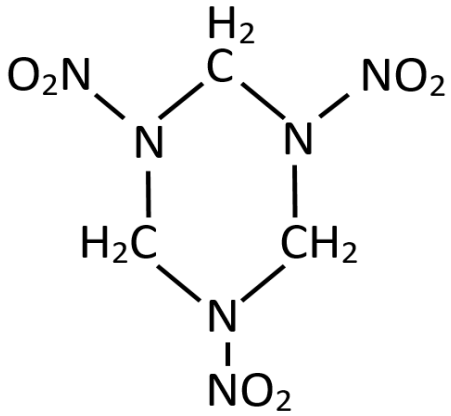

Figure 1. RDX Molecular Structure

The first phase of an explosion is initiation. A detonation occurs when the decomposition reaction caused by the initiation in the explosive occurs at shock velocities [8]. A detonation is a shock wave with a rapid exothermic chemical reaction occurring just behind the shock front. Decomposition reaction consists of the breakdown of chemical bonds holding the explosive molecule together. The explosive produces both fuels (C or CH_2) and oxidizers (O or NO_2) in their gaseous states after decomposition. The oxidizers react or burn the fuels, which releases a substantial amount of heat. The increase in heat causes the gaseous mixture's temperature and pressure to increase significantly. This increase allows the gaseous mixture to expand and create a pressure pulse emanating outward from the explosive [4].

When an explosive is detonating, the reactant molecule is broken down to its individual component atoms. These atoms then recombine to form the final products of the reaction. Detonation reactions consist of over 150 species [4]. However, the oxidation process is usually simplified down to a few molecules, due to the rapid rate these reactions occur. During oxidation, an atom or compound changes because it loses an electron. The typical products formed from explosives are nitrogen, water, carbon

monoxide, and carbon dioxide [8]. Following the simple product hierarchy for CHNO explosives, the oxidation reaction for RDX is:

$$C_3H_6N_6O_6 \rightarrow 3N_2 + 3H_2O + 3CO \quad (2.1)$$

Carbon monoxide will always try to react with another oxygen and create carbon dioxide, so carbon is in its highest oxidation state. If an explosive has any carbon or carbon monoxide left over, a secondary oxidation can occur. This secondary reaction is commonly known as afterburn. The afterburn of RDX is primarily from the reaction of:

$$3CO + 1.5O_2 \rightarrow 3CO_2 \quad (2.2)$$

A detonation has several general phenomena that applies to all explosives. One phenomenon is that the wave speed is continuous through the explosive. This phenomenon means the shock velocity does not speed up or slow down after the explosive has been initiated. Another phenomenon is the detonation wave speed increases with increasing diameter until, at some maximum diameter, there is no longer an increase, when detonating a cylinder along the axial direction. In an ideal detonation, the cross section of the explosive does not have a diameter effect [8]. Additionally, if the reaction media is essentially infinite and chemical equilibrium is achieved, a steady-state or ideal detonation occurs. An ideal detonation wave can be simplified to solely be governed by thermodynamics and hydrodynamics, which allows the wave's properties to be modeled [11]. The ZND model, named after Zeldovich, Von Neumann, and Deering, is the most common model used to calculate different detonation characteristics [8].

In a ZND model, the detonation is a shock wave moving through the explosive. As the shock moves through the explosive, it compresses and heats the explosive, which causes a chemical reaction to occur. This exothermic reaction is completed instantly, in

theory, and the energy released feeds the shock front to drive it forward. Additionally, the gaseous products behind the shock wave expand—causing a rarefaction wave to move forward into the shock. This wave is also known as the Taylor wave (see Figure 2). Taylor was the individual who developed the equations of state that describe the wave [8]. The Taylor wave changes based on a combination of isentrope for expansion of the detonation gases, the charge size, and the degree of confinement. The Chapman-Jouguet (CJ) point is the steady-state detonation condition for the explosive. The Von Neuman spike is a pressure spike caused by the energy found in the reaction. However, this energy is negligible compared to the energy in the fully reacted products. When the shock front, chemical reaction, and leading edge of the rarefaction are in equilibrium, they all move at the same speed, also known as the detonation velocity (D).

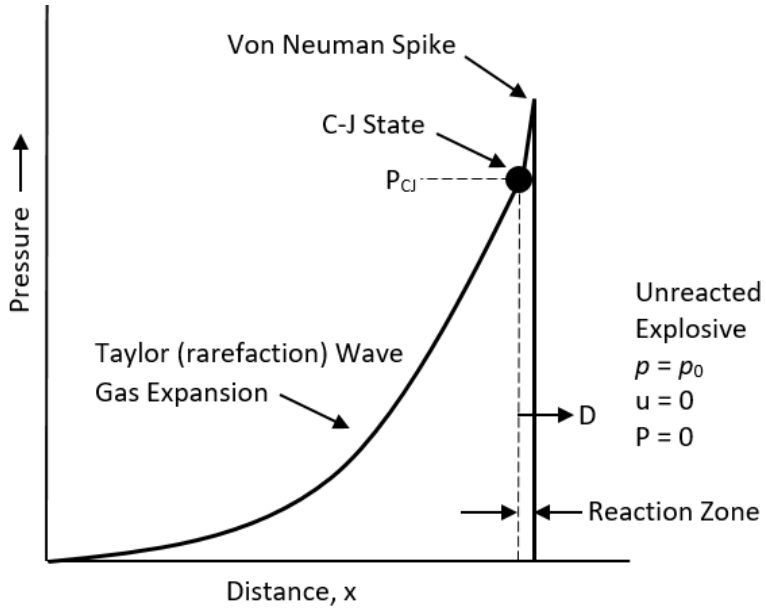

Figure 2. Pressure-distance Diagram of a Detonation Wave

A pressure versus specific volume (Hugoniot) diagram is often used to better visualize the detonation jump condition, which can be seen in Figure 3.

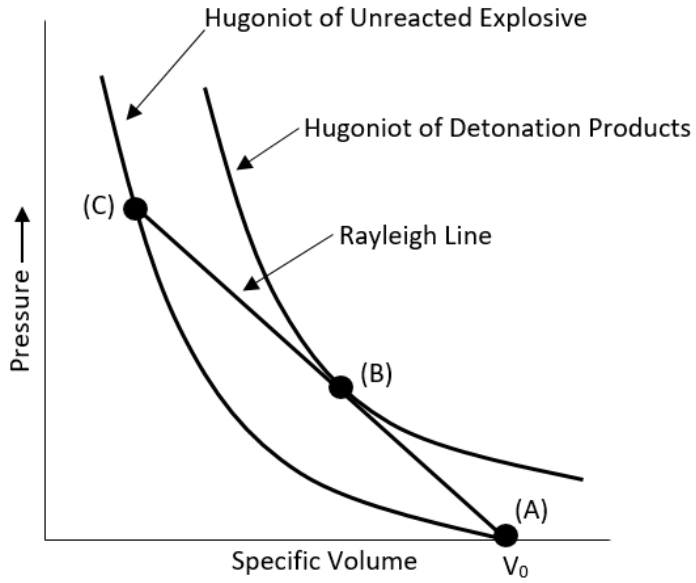

Figure 3. Hugoniot Curves

The two Hugoniot curves show the different properties for both the unreacted and reacted explosive. Point A, in Figure 3, shows the initial state of the explosive. Point C is the fully shocked but unreacted explosive condition. Once these two points are found, a straight line is drawn to connect the two dots—forming the Rayleigh line. Point B is the location where the Rayleigh line intercepts the reacted explosive. Point B is also known as the CJ point. The CJ point is important, because it describes the characteristics of the products behind the detonation front and the main goal in solving the ZND model equations [8].

Extensive research has gone into finding the CJ conditions for different types of explosives. However, the data calculated are only applicable to the initial explosive density and their detonation velocity. The two most important CJ values are density and pressure. By using the known data, several equations were created to estimate these values given a certain explosive density, see Equations 2.3 and 2.4 [8].

$$p_{CJ} = 1.386 p_o^{0.96} \quad (2.3)$$

Where:

p_{CJ} = Chapman-Jouguet density
p_o = Initial density

$$P_{CJ} = p_o D^2 (1 - 0.7125 p_o^{0.04}) \quad (2.4)$$

Where:

P_{CJ} = Chapman-Jouguet pressure
D = Detonation velocity

These conditions, along with the temperature and detonation velocity, are what define the shock wave that propagates from the explosive through the air.

Scientists and engineers have been interested in the processes of generation and transmission of blast waves from explosives beginning in the late nineteenth century [12]. Since then, a significant amount of research has focused on understanding detonation and shock phenomena in explosives [8], [11], [13]–[15]. To obtain different air characteristics before, during, and after a blast wave moves through a zone, the blast wave must be simplified down to an ideal blast wave. Several assumptions must be made to reach this state. The first assumption is the existence of a homogenous atmosphere. The second assumption is that the explosive source is spherically symmetric. These two assumptions allow the characteristics of the blast wave to be functions of only distance from the center of the source and time [12]. The pressure profile of an ideal blast wave can be seen in Figure 4.

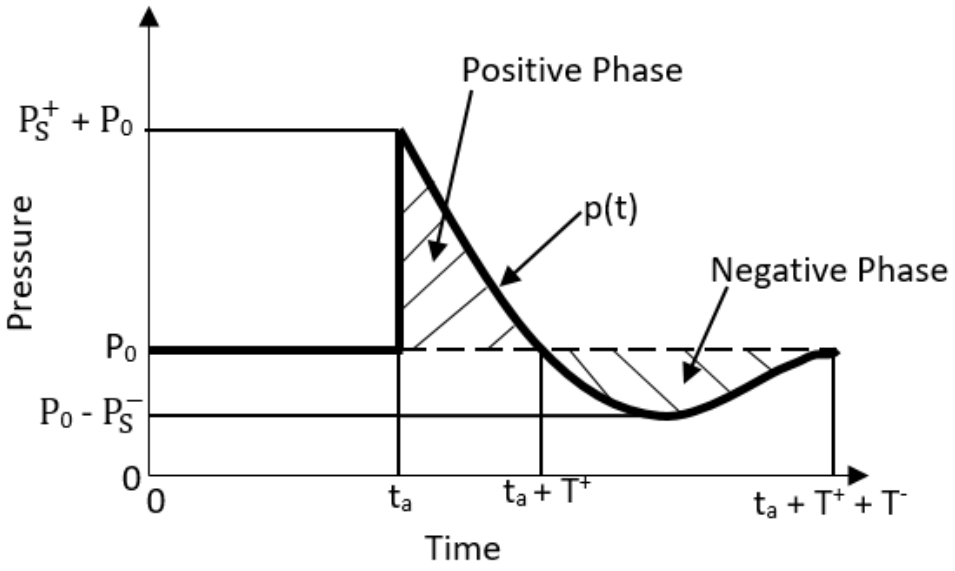

Figure 4. Ideal Blast Wave

The first section of the figure shows when the air is at ambient condition and there is no blast wave. At time, t_a (time after explosion), the pressure spikes abruptly, due to the blast waving moving through the location. As the blast wave moves forward, the pressure at the location will then decay until it reaches ambient pressure again. However, the pressure will continue to decrease until it reaches the partial vacuum pressure value. Finally, the pressure increases again, until it reaches ambient temperature and remains there.

Computer Programs

With the advance of computer's processing ability, several programs have been created to handle complex computation problems. These programs have successfully been utilized for a number of different systems including combustion and scramjet engines [16]. VULCAN, one of the computational fluid dynamics (CFD) programs, is a turbulent, non-equilibrium, finite-rate chemical kinetics, Navier-Stokes flow solver for

different grids [10]. The program is maintained by the Hypersonic Air Breathing Propulsion Branch of the NASA Langley Research Center.

VULCAN handles turbulent reacting and non-reacting flows for subsonic to hypersonic speeds [10]. VULCAN uses special turbulent wall treatments, multi-grid methods for elliptic and space marching schemes, and conditioning of the governing equations to reduce numerical stiffness to limit the computational cost of propulsion flow analysis. VULCAN has the ability to simulate two-dimensional, axi-symmetric, or three-dimensional problems on structured multi-block grid systems. An advantage of using VULCAN is its flexibility with geometry. "Boundary conditions can be imposed on any boundary or boundary subsets and the code has continuous and non-continuous block-to-block interface capabilities." [10] VULCAN is also flexible in the type of thermodynamic and kinetic model specification frameworks used. During a simulation, VULCAN can simulate a calorically perfect single component gas, a mixture of thermally perfect gases, or a mixture of gases in thermodynamic non-equilibrium.

Cheetah®, another program created to handle complex computation problems dealing with explosives, guns, and rockets, is a thermochemical code created by Lawrence Livermore National Laboratory (LLNL) [9]. It is a descendant of both the TIGER and Ruby thermochemical codes and inspired by the CHEQ code. Cheetah® was first used in the 1990s, and it has been updated several times with improvement in function-ability. One of Cheetah®'s standard capabilities includes detonation performance prediction. For detonation prediction, Cheetah® solves thermodynamic equations to find the chemical equilibrium between product species. Cheetah® can predict detonation properties by using the CJ theory, which "states that the detonation

point of an explosive is a state in thermodynamic and chemical equilibrium." [9] Thermodynamic states where the pressure and temperature are not explicitly stated can also be calculated using other known thermodynamic quantities, e.g. volume and entropy. Overall, Cheetah® balances "the chemical potentials while keeping the total moles of each element fixed." [9]

Infrared

Detection of electromagnetic energy, one form of remote sensing, is a means by which information is transmitted from an object to a sensor [3]. Wavelength is an important parameter for electromagnetic radiation [17]. The radiation wavelength is broken up into several different regions -- one of which is infrared. The infrared band covers the spectral region from 1 mm to 0.7 μm [3]. This region has been found to be well suited for detecting ordnance detonations for several reasons. The first reason is the center frequency of spectral emission is centered in the infrared region for the afterburn and decay. Orson calculated the approximate range of the emitted spectra, the maximum wavelength (λ_m), and the total emittance (M) of the three temporal signatures of a typical detonation event (see Table 1) [4].

Table 1. Spectral Range of Explosive Emitted Radiation

Feature	Upper Bound (μm)	Lower Bound (μm)	λ_m (μm)	M (w/cm_2)
Initiation	20+	0.4	1.61	59.50
Afterburn	20+	0.8	2.63	8.30
Decay	20+	3.0	9.66	0.05

The second reason is the time window is much larger for afterburn and decay features compared to the initiation. The time window is important when using satellite imaging for remote sensing, because a satellite can only refresh at a certain rate. This rate is too slow to capture the milliseconds it takes for an explosive to initiate. Finally, there is a large contrast in emittance between a detonation and the corresponding infrared background [4].

The spectral background is comprised of emitted and reflected radiation [4]. The emission sources, along with the different ranges within infrared, can be seen in Figure 5.

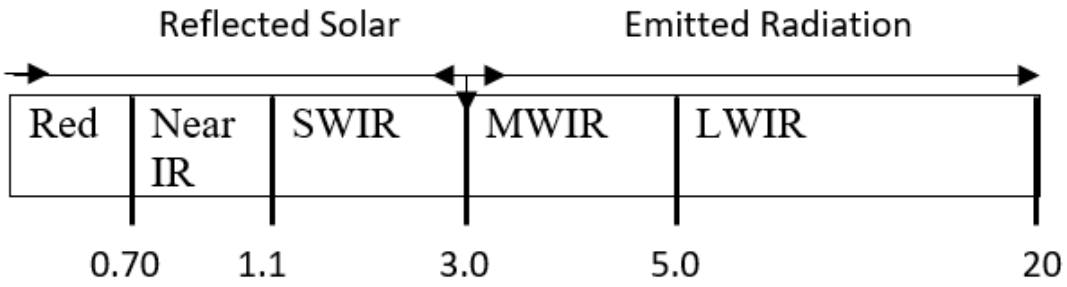

Figure 5. Infrared Spectral Regions (μm)

Where SWIR is short-wave infrared, MWIR is mid-wave infrared, and LWIR is long-wave infrared. The different background emissions vary throughout the course of a day. SWIR is made of emitted and reflected solar radiation, the latter which is only found during the day. MWIR consists of both reflected and emitted radiation during the day, but during the night it is only emitted. The LWIR is always dominated by emitted radiation [4].

Electromagnetic energy transports intensity or energy information. The electromagnetic radiation and its interaction with matter are commonly characterized by a

variety of qualities. Radiant energy is important in explosive detonation signatures [4]. Radiant energy is the "energy carried by an electromagnetic wave. It is the measure of the capacity of the wave to do work by moving an object by force, heating it, or changing its state." [3]

When electromagnetic energy propagates through the atmosphere, it is affected by atmospheric absorption and scattering. Each molecule that makes up the atmosphere absorbs different frequencies of electromagnetic radiation, due to quantum mechanical interactions. In quantum mechanical interactions, the molecule can either be in an electronic, vibrational, or rotational mode. However, vibrational and rotational modes are the typical modes observed in the infrared spectrum for the temperatures and species considered in this thesis [4]. Several molecules can absorb electromagnetic radiation in the infrared spectrum. Water and carbon dioxide are two of those molecules, which are also two of the products produced in an explosion.

Water and carbon dioxide concentrations are dependent on atmospheric conditions; therefore, the concentrations change from day-to-day. The amount of absorption is a function of the concentration of particulate matter and the distance to the source. Atmospheric absorption is related to a transmission coefficient between zero (completely attenuated) and one (no attenuation) [4].

Absorption and scattering are combined to find the total attenuation of the atmosphere. The particulate's cross-sectional area and frequency of the source radiation determine the amount of scattering [4]. Particulates in the atmosphere with radii between 0.1 and 10 μm are able to obscure visibility in the visual, near infrared, and short-wave infrared regions [3]. Examples of these particulate types include clouds, smoke, and dust.

Detonation Signatures

Two DoD priorities are battle-space characterization and technical intelligence [4]. An example of battle-space characterization is the study of infrared signatures of conventional munitions deployed in field conditions. Radiant Brass, a Navy TENCAP sponsored munitions detonation test, was conducted between 1998 and 1999 to obtain information on infrared signatures of conventional munitions deployed in field conditions [4].

> The first test of Radiant Brass was designed to "obtain well calibrated, radiometric, optical signatures on these bombs together with accurate, well documented data on the devices themselves, the nature of explosive events and their effects and the atmospheric characteristics along the observer-to-target line of sight." [4]

However, the data were inconclusive.

Orson conducted research to further advance the inconclusive work of Radiant Brass [4]. The objective of Orson's thesis was to "collect robust infrared spectral signatures of detonation events, discern spectral bands that best discriminate the ordnance, and to possibly provide insight into the identification of ordnance or event conditions." [4] Through his research, the possibility of identifying explosives and event conditions in the battle-space was proven.

Gross examined explosive signatures from a phenomenological perspective [16]. He determined, from examining a subset of data from Orson's work, that classification could be improved. This improvement would be achieved by better understanding the non-Planckian nature of fireball emissions in the MWIR. Through Gross's work, a physics-based model was developed to characterize emissions in terms of fireball size,

temperature, soot, and gas concentrations of various emitting species. His research showed an effective method to discriminate between classes of explosives was possible. Additionally, forensic information on the composition of the explosive material could be obtained from the hydrogen-to-carbon ratios derived from the physics-based model.

Gordon investigated the shock dynamics and fireball temperatures resulting from explosive detonation [18]. His research collected and observed shock propagation using high speed imagery. Gordon then used point blast theory to model the shock expansion, which allowed for detonation efficiency and shock velocity to be estimated. Additionally, fireball temperature was empirically modeled. Gordon's results showed a high correlation between fireball temperature rate of decay and heat released in afterburning combustion. This result leads to another potential for using as discriminator for determining explosives.

Summary

This chapter discussed the information known about explosives, Cheetah® and VULCAN programs, infrared, and detonation signatures. Organic explosives are comprised of carbon, hydrogen, nitrogen, and oxygen. Once an explosive is detonated, it produces nitrogen, water, and carbon dioxide as well as a pressure wave. These products expand outwards in an assumed symmetric hemisphere and interact with the atmosphere. The infrared band is ideal for observing water and carbon dioxide, which are among two of the products created from a detonated explosive. Research has proven it is possible to discriminate between explosive classes using data found in the infrared spectrum.

III. Methodology

Chapter Overview

The purpose of this chapter is to describe the methodology of creating and displaying a simulation of the aerothermal and chemical concentrations of an RDX explosion. The first section will discuss how the initial properties of the shock wave were obtained. The second section will describe the steps taken to design the grid. Next, details pertaining to running the simulation will be explained. Finally, the last section will explain how the aerothermal, and chemical concentration results will be shown.

Initial Properties

The first step in simulating the explosive shock wave through the air was determining the initial properties of the shock wave. To obtain this information, version 7.0 of Cheetah® was utilized. Using the detonation standard run in Cheetah®, the detonation properties of RDX were found. The standard run was based on the CJ detonation theory [9]. By using the CJ theory, several simplifying assumptions about detonation could be applied. Two of the most important assumptions were the detonation was one dimensional and the transformation of the explosive products was extremely fast compared with typical hydrodynamic timescales. Because of these two assumptions, the state immediately behind the shock front aligned with the shock Hugoniot of the chemically equilibrated detonation products. Using CJ theory and the hypothesis that "steady state detonation corresponds to the point of tangency between the shock Hugoniot and the Rayleigh line" [9], the CJ velocity could be found by looking for the

smallest shock velocity that corresponded to the detonation products in full chemical equilibrium.

Once the CJ state was determined, Cheetah® calculated the expansion of the detonation products from the CJ state to a pressure of one atm [9]. Since the expansion occurs on timescales of 10's of microseconds, the expansion is adiabatic. By being adiabatic, every state along the expansion path was at the same entropy. Cheetah® then performed a series of calculations at preset expansion volumes until a pressure of one atm or a temperature of 298 K was reached to determine the total energy of the detonation. These results in turn define the mechanical and thermal contributions for the explosion. Finally, the adiabat found in the previous step were fit into a Jones-Wilkins-Lee (JWL) equation of state (EOS) to produce the final results. JWL EOS is widely used in modeling the detonation products of HE.

This thesis focused on RDX exclusively as the explosive, so 100% mass fraction of RDX was added to the initial composition window in Cheetah®. The theoretical maximum density (TMD) for RDX, 1.816 g/cc, was used as the explosive's density in the calculations. TMD is mass per unit volume of a single crystal [8]. With the above two inputs, Cheetah® calculated the detonation properties for pure RDX. See Appendix A for Cheetah® output file for RDX. The variables of interest generated from Cheetah® were the detonation velocity (8.862 km/s), molecular weight (222.117 grams), pressure (33.459 GPa), volume (0.421 cc/g), density (2.373 g/cc), and temperature (3434.3 K). These values were used to aid with the grid design, as well as in the simulation input file, which will be further described in the next two sections.

Grid Design

The second step in simulating an explosive's shock wave through the air was designing and creating the grid in Pointwise®. One of the assumptions for this thesis was that the explosive detonated on the ground at sea level. This assumption meant the shock wave from the explosive would be in the shape of a hemisphere, see Figure 6.

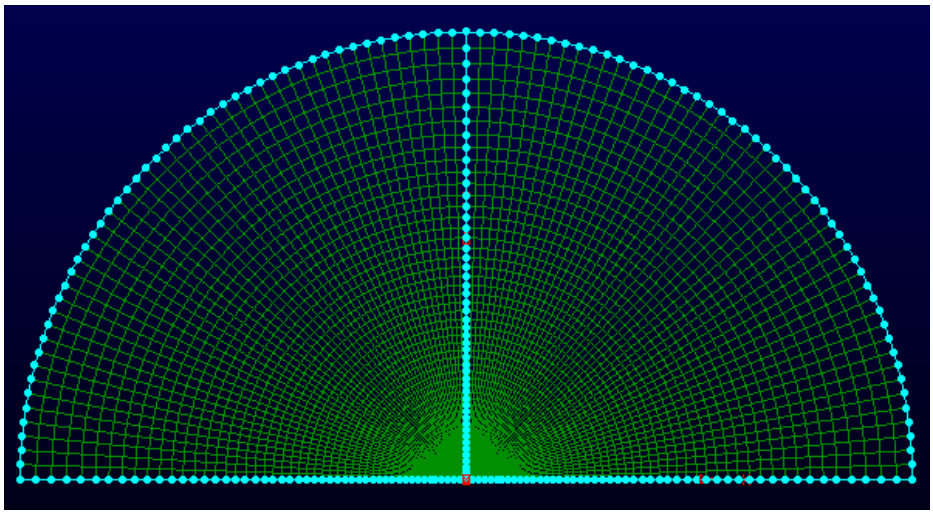

Figure 6. Explosive's Hemisphere

A plane of symmetry was found, so the grid design used in the simulation only consisted of the right half of the hemisphere, see Figure 7 and 8.

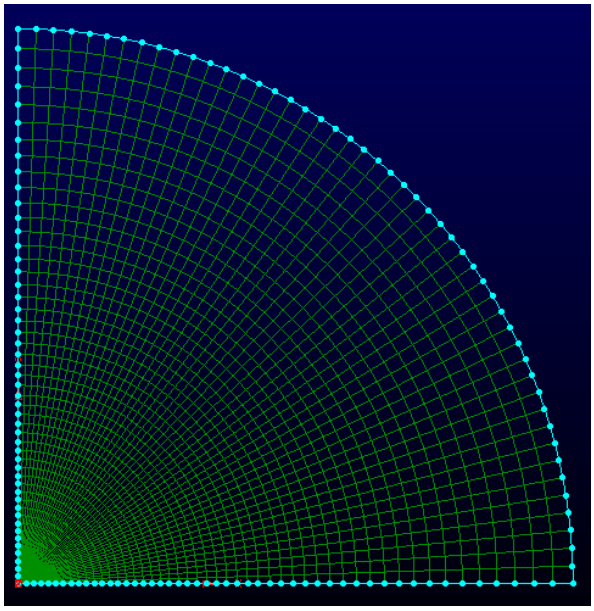

Figure 7. Half-Hemisphere Grid

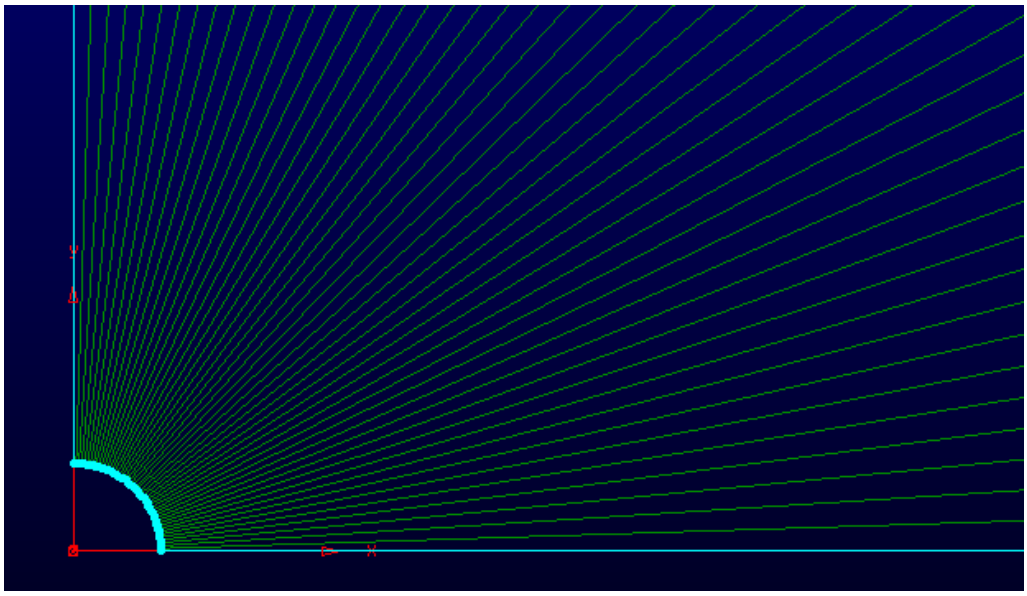

Figure 8. Close-up of Origin on Half-Hemisphere Grid

To calucate the initial radius of the explosive's hemisphere (see Equation 3.1), the hemisphere volume equation was used. The value for the volume used in Equation 3.1 was determined by multiplying Cheetah®'s calcuated CJ volume by the mass of the

explosive (see Equation 3.2). A MATLAB code was created to calcuate these values (see Appendix B).

$$r = \sqrt[3]{\frac{V}{2/3\pi}} \tag{3.1}$$

Where:

r = Radius of detonated explosive
V = Volume of detonatted explosive

$$V = V_{CJ} * m \tag{3.2}$$

Where:

V_{CJ} = Chapman-Jouget volume
m = Mass of explosive

The initial radius of the explosive's hemisphere was used to create the smaller radius of the grid used in the simulation. For the 500 kg, 1000 kg, and 2000 kg grids, their radius were 46.5 cm, 58.6 cm, and 73.8 cm, respectfully. An overall length of 800 m was used for the x-axis and y-axis for the test 500 kg grid design. The results from the test simulation run of 75 milliseconds for the 500 kg explosive showed the pressure wave still under 200 m, so the x-axis and y-axis lines were reduced to 300 m for the rest of the simulations for all three masses to reduce the amount of computer run time for the simulations. The larger radius of the grid used in the simulation was created by connecting the x-axis and y-axis lines.

A structured grid was used in the explosive's grids, due to the nature of shock waves moving outwards from the source evenly. The radius located at the origin had a grid spacing of 0.737 cm for the 500 kg grid, 0.46 cm for the 1000 kg grid, and 0.582 cm for the 2000 kg grid. The larger radius had a grid spacing of 4.77 m for the 500 kg grid

and 2.37 m for the 1000 kg and 2000 kg grids. A spacing of 0.1 m was chosen for the points at the origin on the x-axis and y-axis lines. This spacing was determined by executing a grid convergence study with varying spacing at the origin for the 1000 kg grid to see where the results converged. As shown in Figure 9 to Figure 11, both results for spacing of 0.09 m and 0.1 m are the same, while the results for 0.2 m spacing were slightly different. There was a difference of 8 cm between the 0.2 m spacing and 0.1 m spacing pressure results.

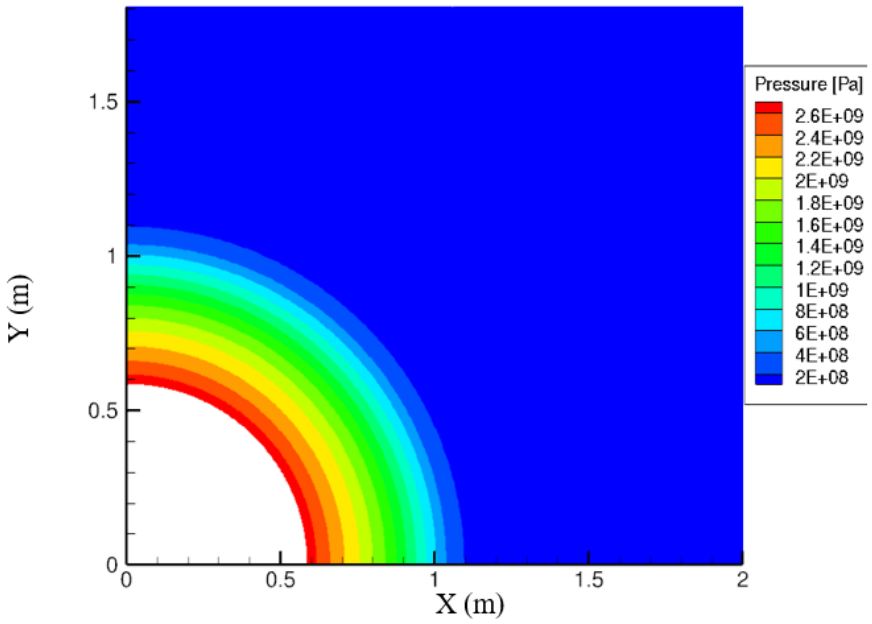

Figure 9. Pressure Distribution at 44.1 µs with Spacing of 0.09 m for 1000 kg

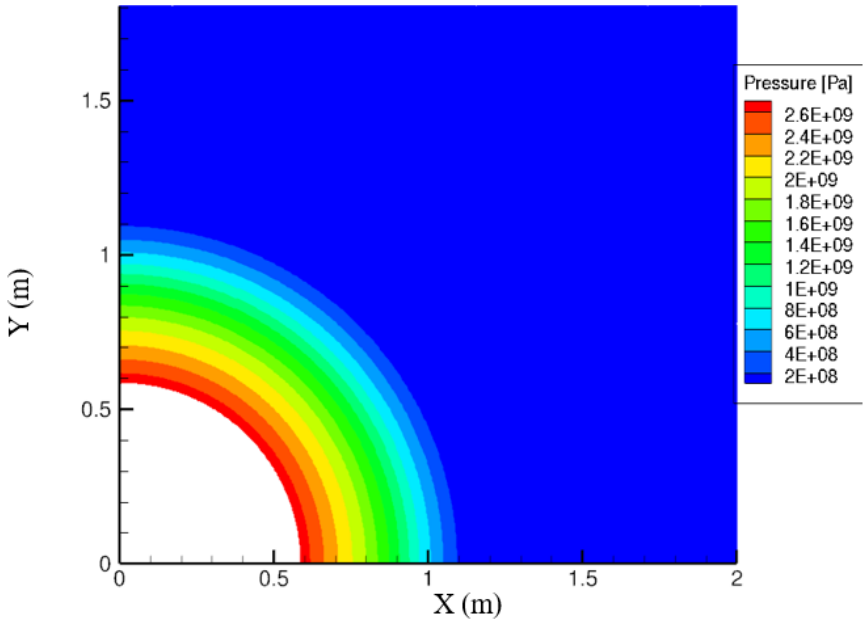

Figure 10. Pressure Distribution at 44.1 µs with Spacing of 0.1 m for 1000 kg

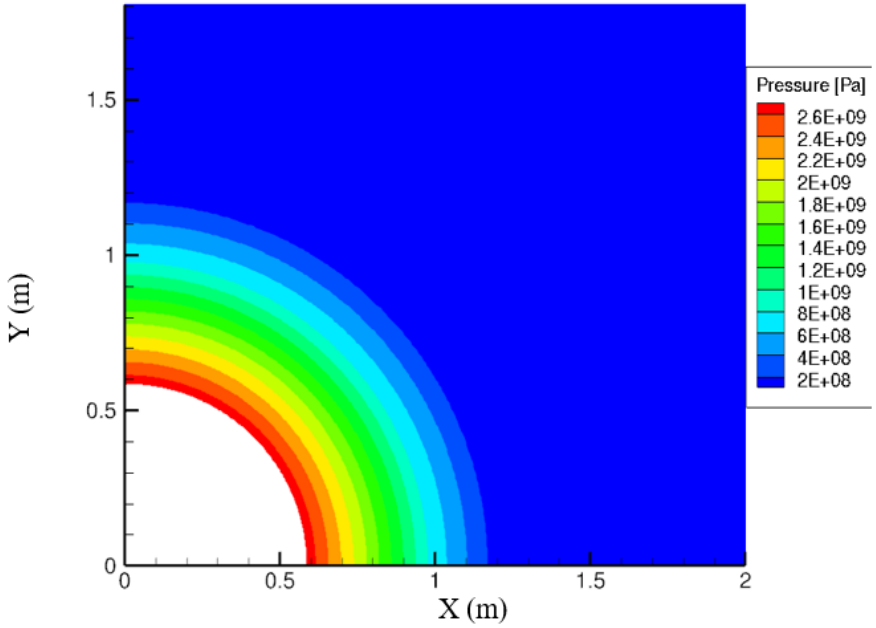

Figure 11. Pressure Distribution at 44.1 µs with Spacing of 0.2 m for 1000 kg

The test 500 kg grid contained 500 points along both the x-axis and y-axis lines. This cell count was based on having a grid spacing around 8 m at the outer end of the 800

m lines. For the 500 kg, 1000 kg, and 2000 kg grids used in the simulations, 404 points were used on the x-axis and y-axis lines. This number was calculated by taking the 500 kg's 800 m line and splitting it at the 300 m mark. This number allowed for the spacing of the shorter grid to be the same as the spacing found in the original 500 kg grid along these lines. This consistency in grid spacing allows for comparison of results between all three masses. These grids were then exported to a .grd file, so they could be used in the simulation run in VULCAN.

Simulation

The third step in simulating the explosive shock wave through the air was compiling and running the simulation code. The program VULCAN was used to simulate the shock wave moving through the air and its subsequent reactions, because it can handle supersonic flow. VULCAN uses an input file to control the calculations it is required to complete. VULCAN's input file "provides many options for defining a computational domain, setting boundary conditions, initializing the flow, controlling the solution process, and selecting information to be post-processed for plotting." [10]

Two different VULCAN input files were created for this thesis (see Appendix C and Appendix D). The first input file (explosion) ran a simulation to show the explosive's products being released from the explosive. The second input file (wave) simulated the explosive being expended and the after effects of the explosion. The two input files were similar in information provided except for the boundary conditions, using a restart file, the size of the time steps, and run time.

The boundary conditions for the grid were defined in the VULCAN input file. The smaller radius line was the only axis different between the two input files to account for the explosive being completely expended. The x-axis line, bottom, was assigned as an axisymmetric center-line, because VULCAN only allowed a boundary aligned with the x-axis to be this type of boundary. This meant the y-axis line, called left in the file, had to be the wall instead. The left boundary was assigned as a standard Euler wall boundary with pressure extrapolated in the wall to represent the ground. The large radius line, outflow, was labeled as a supersonic outflow boundary with zeroth order extrapolation of all variables, since it is just representing the air. In the explosion input file, the smaller radius line, exp-in, was a supersonic inflow boundary condition. A second code line was used to describe the conditions of the inflow. The input values for temperature, velocity, and density were taken, to describe the explosive's conditions, from the Cheetah® output. The mass fractions for N_2 (0.378), CO (0.378), and H_2O (0.244) were also located in this line. Only the products of RDX were used in the simulation because of the short time frame it takes for them to be produced. An average sensing device would not have the ability to capture the decomposition of the explosive because it occurs on a nano- to micro-second timescales [16]. In the wave input file, the smaller radius line became the same boundary type as the y-axis line, a wall.

The first information found in VULCAN's input file was the dimension of the problem and the input control data. This thesis focused on the axisymmetric simulation of an RDX explosion, so the problem was calculated in VULCAN by solving the governing equations for axisymmetric flow without swirl. The axisymmetric grid created in Pointwise® was called into the program in the input control data section of the input

file. This section also contained the name of the restart file used and the name of restart file created at the end of the simulation. Both the explosion and wave input files output a restart file, but only the wave input file used a restart file in its simulation. The wave input file used the restart file output from the explosion input simulation, so VULCAN would simulate the aerothermal and chemical concentrations created from the expenditure of the explosive. The explosion input file did not use a restart file, because its simulation was the overall start for the complete simulation run.

The second set of information found in VULCAN's input file was the output control data. This section contained the information the simulation would output and how often. Density, Mach number, pressure, temperature, and mass fractions were the aerothermal results output in this thesis. The chemical results that were chosen to output were the mass fraction of every species used in the simulation. The species consisted of N, N_2, O, O_2, NO, CO, CO_2, and H_2O. The explosion input file output this information after every 10 to 20 iterations to show the progression of the aerothermal and chemical concentrations. However, the wave input file only output this information after 1,000 to 5,000 iterations to not overload the memory storage on the computer.

The third set of information included the equation set, gas and thermodynamic, and chemistry model data. The equation set data described the type of equations to be used in the simulation, which in this research was the Navier-Stokes equations. Navier-Stokes equations were chosen over Euler equations, so viscous flow could be incorporated into the thermophysic simulations. The gas and thermodynamic data informed the program that a mixture of thermally perfect gases would be used for the gas and thermodynamic model. The decision to use thermally perfect over calorically perfect

gases was made based on the high Mach number used for gas flow causing the specific heat capacity to be a function of temperature. The chemistry model data contained the information regarding the chemical kinetics model used and the treatment of the source term in species transport equations. A finite rate chemical kinetics model was used in this thesis, so chemical reactions could occur between the explosive's products and the air. Additionally, analytical Jacobian was used for the implicit treatment of the source term in species transport equations. Analytical and numerical Jacobian results have been proven to be virtually identical, so analytical Jacobian was chosen because it is faster [19].

The fourth set of information was the chemical species information. Eight chemical species (N, N_2, O, O_2, NO, CO, CO_2, and H_2O) were used in this simulation to describe the makeup of the air and the explosive's products. The gas model used was one of the files provided from the VULCAN software. Additionally, another provided file, the reaction model file of NASA Kang and Dunn five species/five reaction air kinetic model, was used [10]. However, the reaction model file did not contain information regarding CO_2 reactions, so two additional reactions were added to the reaction model file. The CO_2 reaction information regarding the reaction mechanism and Arrhenius values were taken from NASA's LAURA [20] and FUN3D [21] codes. The simplified version of air was used in this thesis to match with the reaction model file. The mass fraction of 0.7686 for N_2 and 0.2314 for O_2 were used for air.

The fifth set of information in the input file was the reference condition data. This data were used to set up the initial conditions within the grid. Since it was assumed the explosion occurred at sea level, values used in the simulations were based on standard

sea level conditions. Those values were a Mach number of 0.01, a total temperature of 288.15 K, and a total pressure of 101,325 Pa. A Prandtl number of 0.72 and turbulent Prandtl number of 0.90 were used to match with the required numbers used in the Wilcox 1988 k-ω turbulence model, since this turbulence model was used in the simulation.

The sixth set of information consisted of the turbulence model data and the Runge-Kutta integration control. Since an explosion is a violent event, a turbulent model was used during the simulation. A blended Wilcox 1988 k-ω and Jones Launder k-ε two-equation model of Menter was used. The blended two equation model of Menter was chosen over the other turbulence models, because it was one of the most prominent two-equation models in turbulence modeling. The Runge-Kutta data defined how many stages used and the type of smoothing that occurred. The Runge-Kutta values used came from a previous VULCAN input code (shock_tube_rk.dat) that was ideal for evaluating shock-capturing characteristics.

The seventh set of information regarded the boundary and cut controls. This section described how to treat the grid and boundaries. The data told VULCAN there were 4 different boundary condition groups, since all 4 sides would need to act as different boundaries. The boundary data also told VULCAN that there was only one box (i.e. grid) in the simulation. The ability to have turbulence and reactions to occur was also set in this section. Turbulence was turned on in the simulation, because an explosive event is known to be turbulent. Additionally, reactions were turned on, so the explosive's products could react with the air (e.g. CO to CO_2). Finally, the command to plot the information found in the grid was turned on in this section.

The next set of information involved the solution methodology. The important information in the first line contained the type of solver used in the simulation. The solver chosen for this thesis were an elliptic active solver. Elliptic was chosen over parabolic, so the simulation could be time accurate. The most important information found in the second line was the number of iterations to be run during the simulation. Line three, multi-grid control data, found in this section did not contain any important variables because only one grid was used. The turbulence model control data, line four, contained information on the order of accuracy and the wall turbulence boundary conditions. The highest order, second order, of accuracy was used to treat convective terms of the turbulence to obtain more accurate results. Additionally, the input file told VULCAN to solve to the wall to get a complete view of the turbulence found in the simulation. The final line found in the solution methodology section was the most important. It contained the information that controlled the time stepping scheme for the simulation. Both Runge-Kutta and Diagonalized Approximate Factorization (DAF) were used for this thesis. Runge-Kutta was chosen for the baseline, because it is a well-known and accurate method used in many computer packages. Simulations for 500 kg, 1000 kg, and 2000 kg all used the Runge-Kutta scheme as the baseline. DAF was used in a second simulation of the 500 kg to compare results, so the results for the Runge-Kutta simulation could be further validated. The type of method used for the time step was the specified time step scheme, Δt, so the simulations would be time accurate.

Time accurate methods were used in the simulation to provide time accurate results. To determine the time steps in each simulation, the time it took for the explosive to be expended had to be calculated. The first step in solving for the time was to

calculate the mass flow rate for the explosive (Equation 3.3). Once the mass flow was calculated, the time could be solved (Equation 3.4).

$$\dot{m} = p_{CJ} * D_{CJ} * \pi * r^2 \quad (3.3)$$

Where:

$\dot{m}$ = Mass flow rate

$$t = \frac{m * 1000}{\dot{m}} \quad (3.4)$$

Where:

t = Time required for explosive material to be completely expended

Using the MATLAB code previously talked about, the explosive was completely expended after 35 microseconds for 500 kg, 44.1 microseconds for 1000 kg, and 55.6 microseconds for 2000 kg. These numbers were then divided by 100 for the 500 kg run and 200 for the 1000 kg and 2000 kg runs to obtain the time steps for the explosion input file. The variation of the same time step (0.25 microseconds) was used in all wave input files, so the results could be compared accurately across the different runs.

VULCAN output a variety of files after completing its calculations. However, only three types of files were important for this thesis. The first files output were the restart files. These files were important in setting up the wave simulation. The second file included the grid file created from VULCAN, because it could be used in Tecplot 360® to help visualize the results. The final type of file was the function file. The function file contained the results for the different variables requested in the input file. The function files could then be used in Tecplot 360® to help visualize the results.

Display

The final step in simulating an explosive's shock wave through the air was visually displaying the results gained from VULCAN. The grid and function files produced from VULCAN were input into Tecplot 360®. The contour option was utilized to display the different values for temperature, pressure, and Mach at one of the output time steps. An xy graph was used to graph the mass fractions for the different species to more easily visualize their distributions. Chapter IV (see pg. 34) will go into more detail about what the results showed.

Summary

This chapter described in detail the methodology used in this thesis to computationally model an explosion. Using Cheetah®, Pointwise®, VULCAN, and Tecplot 360®, this thesis simulated the aerothermal and chemical concentrations of an RDX explosion. Cheetah® produced the initial properties of the RDX's explosive shock wave. These values, in turn, were used to help design the grid and the simulation input file. VULCAN calculated the reaction that occurred between the air and the shock wave, as it moved through the grid. Lastly, Tecplot 360® was utilized to graphically visualize the results produced from VULCAN.

IV. Analysis and Results

Chapter Overview

This chapter details the results from the three different simulations of the thermophysics of an explosive shock wave traveling through the air. Chapter IV will first report aerothermal results (pressure, temperature, and Mach number) and then chemical results (CO, CO_2, and H_20 mass fractions) for a 500 kg, 1000 kg, and 2000 kg RDX explosion. Since results were output for a significant amount of time steps and were nearly identical, only a portion of the data collected will be shown in this chapter.

Aerothermal Results

The first type of important results of the thermophysics simulations was aerothermal results. This thesis specifically looked at pressure, temperature, and Mach number. Pressure and Mach number were chosen in order to visualize the shock wave and its propagation away from the explosive. Temperature was chosen because it could help identify heat signature as well as determining if it was possible for chemical reactions to still occur.

500 kg Runge-Kutta

For the 500 kg Runge-Kutta explosion, the final products from the RDX explosive, N_2, CO, and H_2O, were reported for a total of 35 microseconds, using 0.35 microsecond time steps, to show the complete expenditure of the explosive material. The pressure wave created from the completion of the explosion traveled a distance of around 0.85 cm from the center of the explosive, 0 m (see Figure 12).

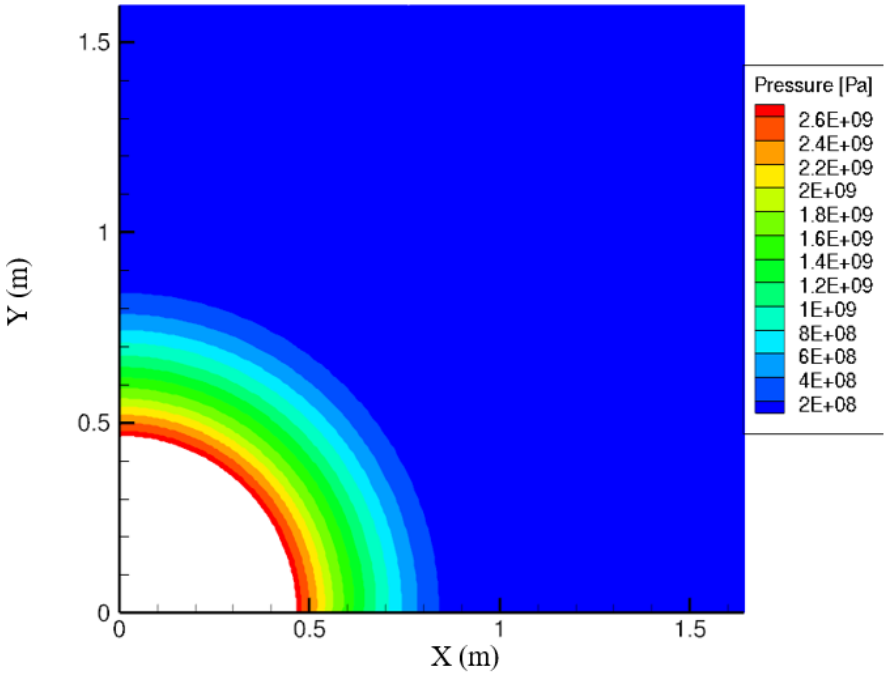

Figure 12. Pressure Distribution at 35 μs for 500 kg R-K

The highest pressure value, at 35 microseconds, was located at the origin with a value of 2.6 GPa. The highest pressure layer was located closest to the origin. The value decreased when moved outwards from the origin. The difference found between the highest pressure value and lowest pressure value within the pressure profile was around 2 GPa.

The temperature profile created from the complete expenditure of the explosive can be seen in Figure 13.

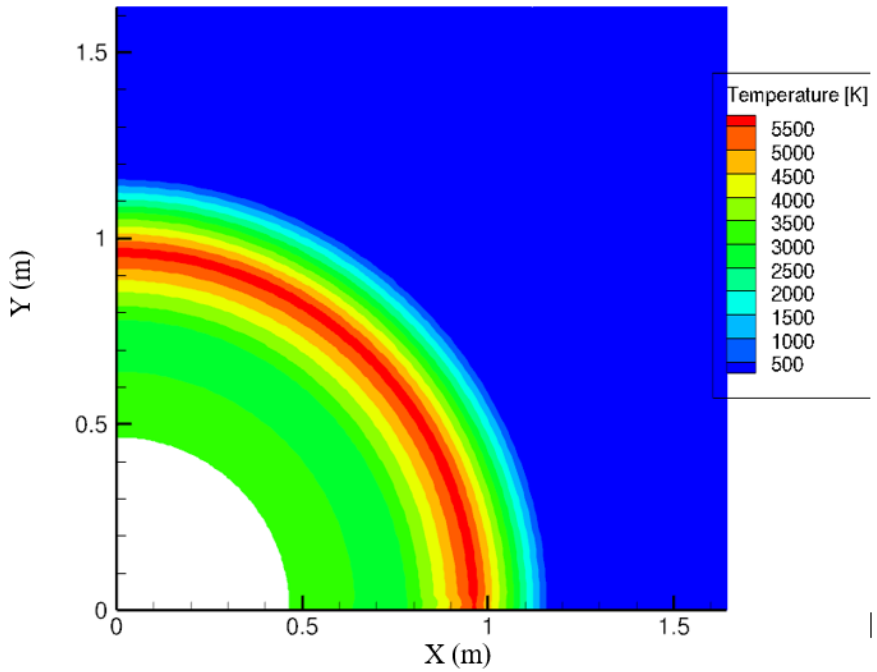

Figure 13. Temperature Distribution at 35 μs for 500 kg R-K

The temperature profile traveled a distance of around 1.14 m from the center of the explosive. The temperature profile varied from the pressure profile in that the highest temperature value, 5500 K, was located closer to outer edge of the profile.

The Mach Number profile for the 500 kg Runge-Kutta case is shown in Figure 14.

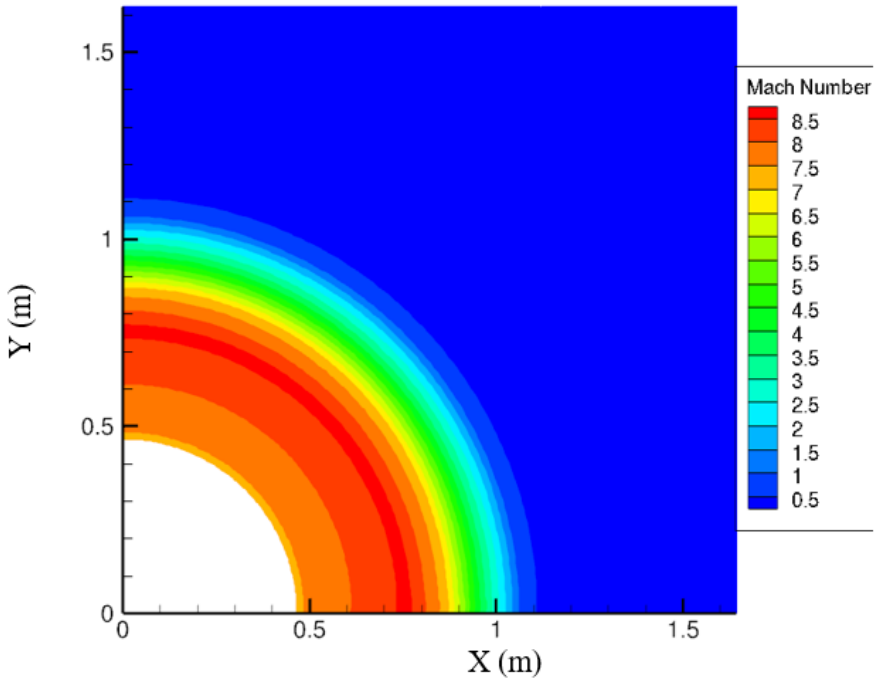

Figure 14. Mach Number Distribution at 35 μs for 500 kg R-K

The Mach number profile traveled a distance of around 1.1 m. The Mach number profile contained the highest value, 8.5, in the middle of the profile. When following the profile towards the origin, the Mach number was slightly higher (Mach 7.5) compared to the numbers on the outer side (Mach 2.5) of the profile.

After the explosion simulation was complete, the wave input file was simulated. In the wave simulation, a time step of 0.25 microseconds was utilized. The total run time of the simulation was 25 milliseconds, because it took a week to be completely run. The first set of results shown from the 500 kg Runge-Kutta wave simulation are at the 0.5 millisecond time frame. This time was chosen to show results at a time very close to the end of the explosive expending but with enough time for the aerothermal profiles to have moved away from the origin. Additionally, the results at this time step could be compared to the 500 kg DAF, 1000 kg R-k, and 2000 kg R-K results.

The pressure profile at 0.5 milliseconds had traveled a distance of 5.5 m from the center of the explosive (see Figure 15).

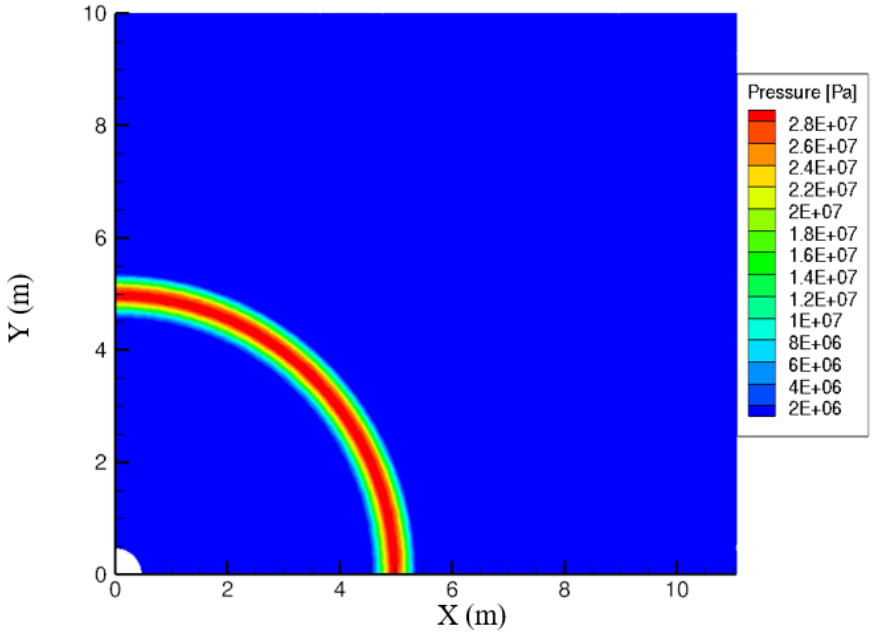

Figure 15. Pressure Distribution at 0.5 ms for 500 kg R-K

The highest pressure value, 28 GPa, zone moved from inner side of the profile to the middle of the profile. The pressure distributions on either side of the highest pressure zone were the same, with the pressure decreasing from the center outwards.

The second time frame shown below was at 1.25 milliseconds. This time was chosen to show the final transition in where the highest pressure layer was located in the pressure profile. The pressure profile from this time step can be seen in Figure 16.

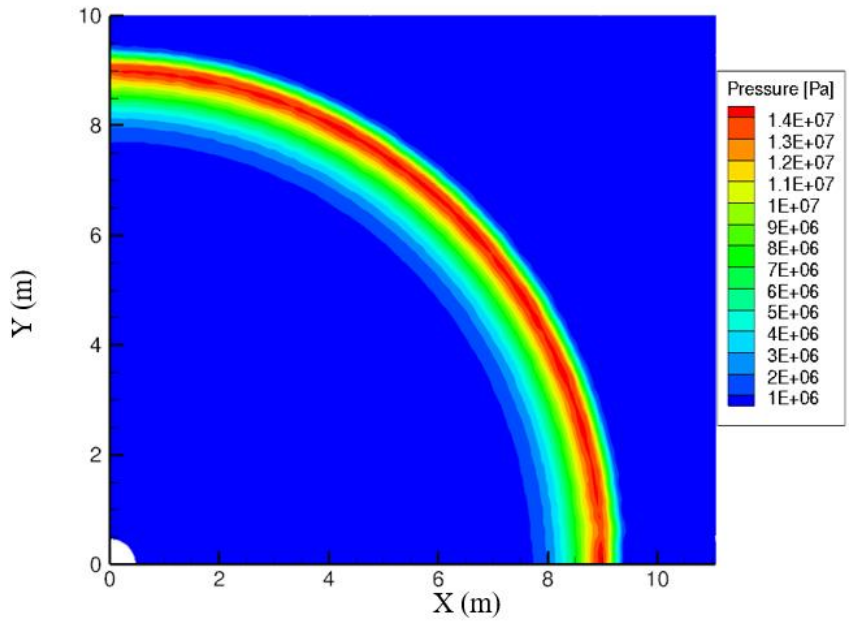

Figure 16. Pressure Distribution at 1.25 ms for 500 kg R-K

At 1.25 milliseconds, the pressure wave reached 9 meters from the center of the explosive. The highest pressure layer, 14 MPa, moved towards the front of the profile after 1.25 milliseconds. This pressure distribution is similar to what an ideal blast wave would look like, as discussed in Chapter II. The overall pressure values found within the pressure profile decreased compared to the origin pressure values. It is expected that the pressure found within the wave would decrease overtime as it interacted with the lower pressure ambient air.

The pressure distribution results up to 5 milliseconds followed the same pattern found at 0.5 milliseconds into the wave simulation. However, at 5 milliseconds a second pressure profile appeared at the origin (see Figure 17).

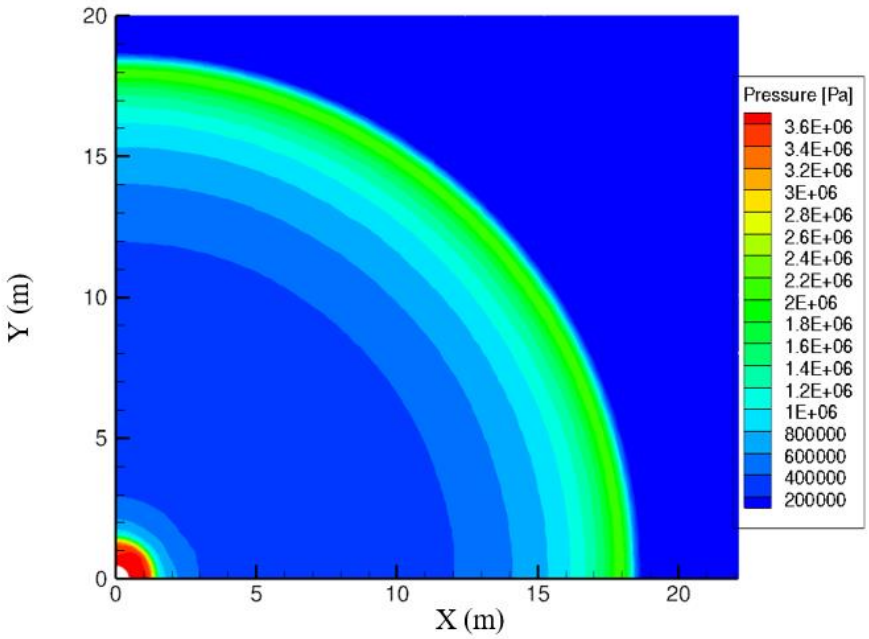

Figure 17. Pressure Distribution at 5 ms for 500 kg R-K

This second pressure distribution at the origin looked similar to the pressure distribution found at the end of the explosion simulation. However, the pressure values found within the 5 milliseconds pressure profile were lower. A secondary reaction or afterburn of the RDX would explain the second pressure profile. This conclusion was further backed by the chemistry results discussed later in the chapter.

The first pressure profile continued to behave similar to the 0.5 millisecond pressure profile throughout the 25 millisecond simulation. After the emergence of the second pressure profile, the second pressure profile followed the behavior that the first pressure profile exhibited during the simulation. At 25 milliseconds, the second pressure profile decreased the distance between the two profiles from 9 m down to 2 m (see Figure 18).

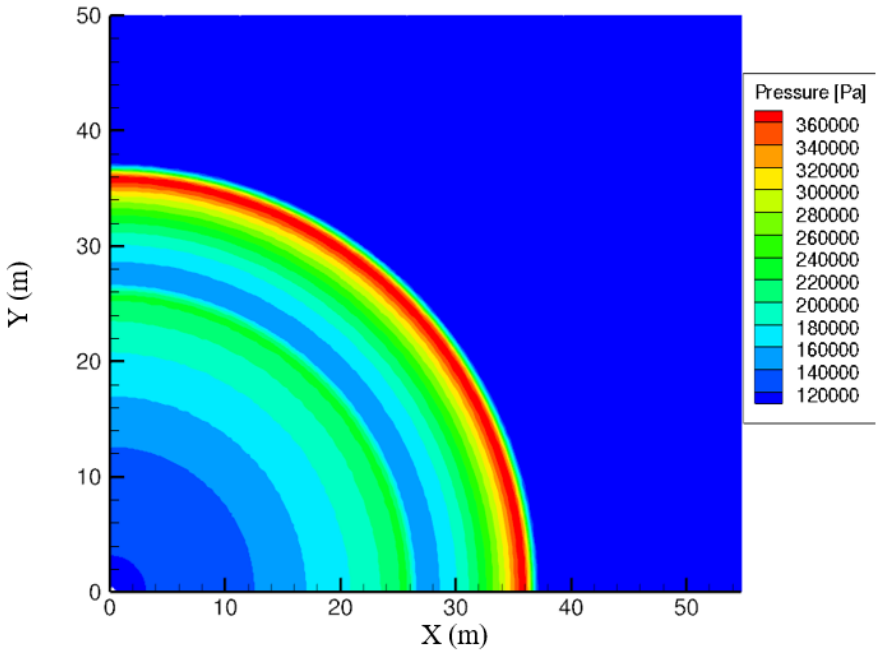

Figure 18. Pressure Distribution at 25 ms for 500 kg R-K

The temperature profile followed the same transitions that the pressure profile did at 0.5 milliseconds. The temperature distribution found at 0.5 milliseconds can be seen below in Figure 19.

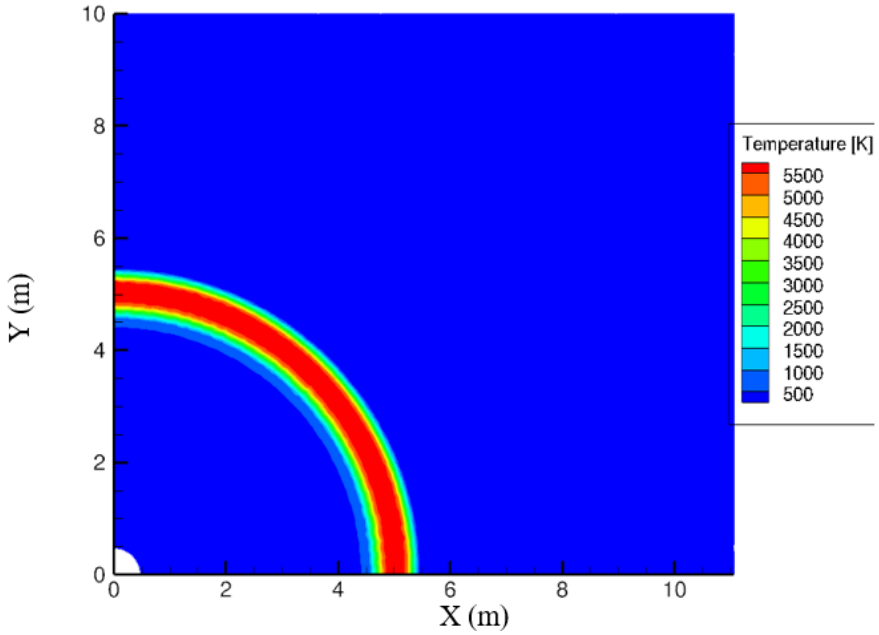

Figure 19. Temperature Distribution at 0.5 ms for 500 kg R-K

The temperature file traveled the same distance as the pressure profile at 0.5 milliseconds. Additionally, the highest temperature value, 5500 K, zone was found in the center of the temperature profiles. The temperature values decreased, when moving outwards from the highest temperature zone.

The temperature profiled at 1.25 milliseconds can be seen below in Figure 20.

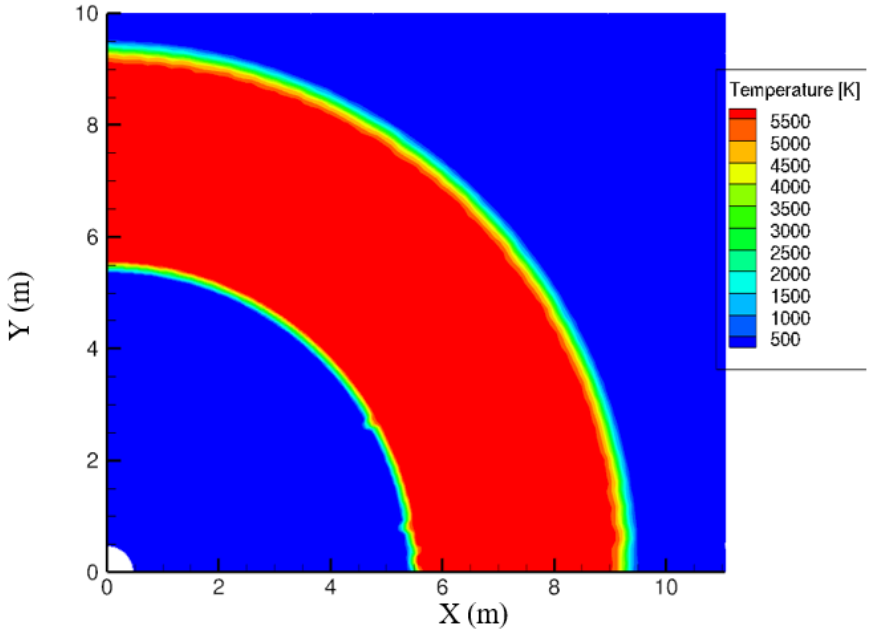

Figure 20. Temperature Distribution at 1.25 ms for 500 kg R-K

The temperature profile reached the same distance from the center of the explosive as the pressure profile. However, the temperature profile's thickness was double the thickness of the pressure profile and measured approximately 4 m. Additionally, the highest temperature value, 5500 K, remained the same as the value found at the completion of the RDX material being expended. The highest temperature layer also took up most of the temperature's profile thickness.

The temperature distribution at 2.5 milliseconds was different than the previous 1.25 millisecond results (see Figure 21).

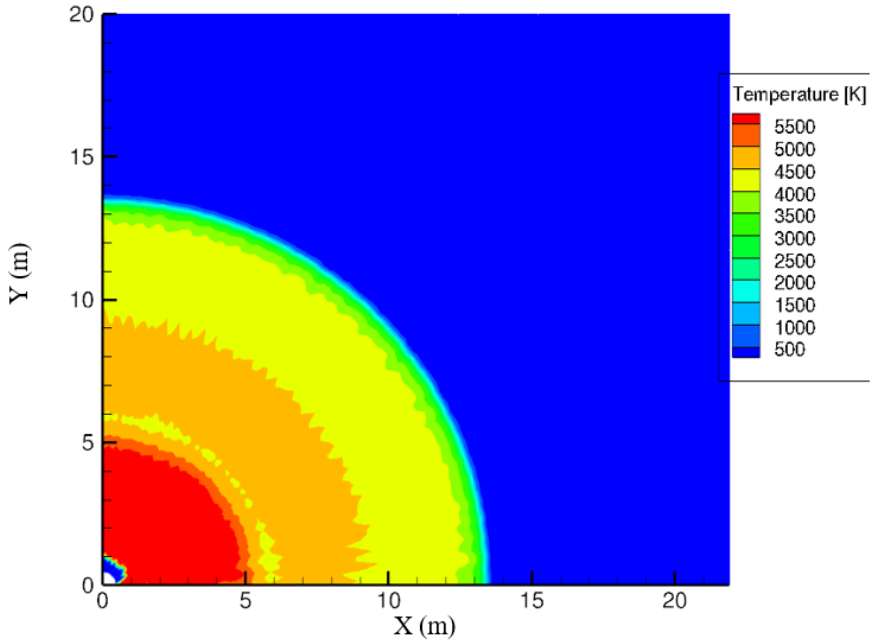

Figure 21. Temperature Distribution at 2.5 ms for 500 kg R-K

The temperature distribution reached the same distance as the pressure distribution after 2.5 milliseconds, but its profile took up the entire distance to the 13.5 meters. The hottest temperatures were located near the origin and slowly decreased in temperature when moving outward from the origin. Additionally, the hottest temperature value, 5500 K, remained the same as when the explosion had just been completely expended.

The temperature distribution found in the 2.5 millisecond time frame continued to remain the same overall shape for the rest of the wave simulation (see Figure 22).

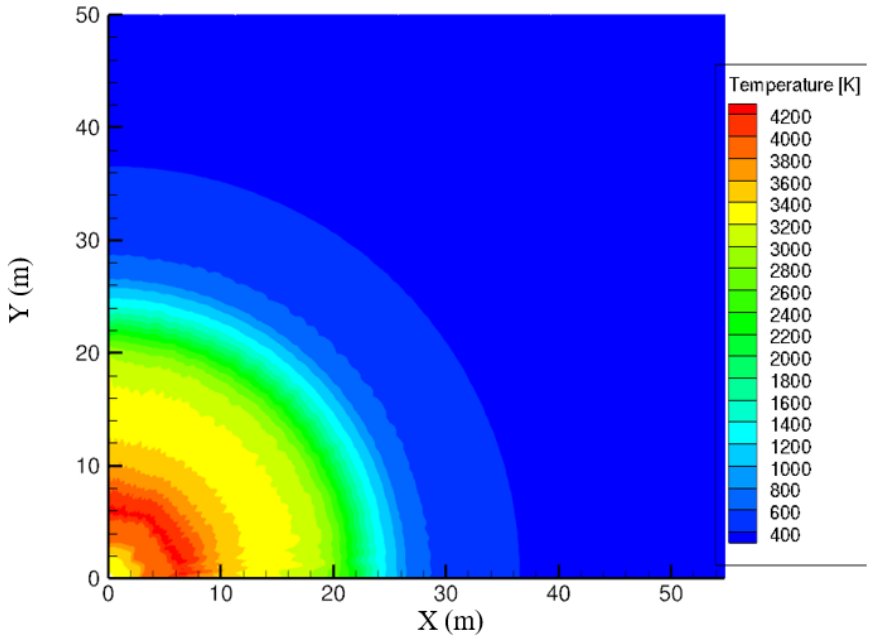

Figure 22. Temperature Distribution at 25 ms for 500 kg R-K

The temperature profile continued to travel outwards from the origin following the same pattern as the pressure profile. At 25 milliseconds, the overall temperature values found in the profile decreased, with the highest value being 4200 K.

The Mach number distribution at 0.5 milliseconds drastically changed compared to the end Mach number results from the explosion simulation (see Figure 23).

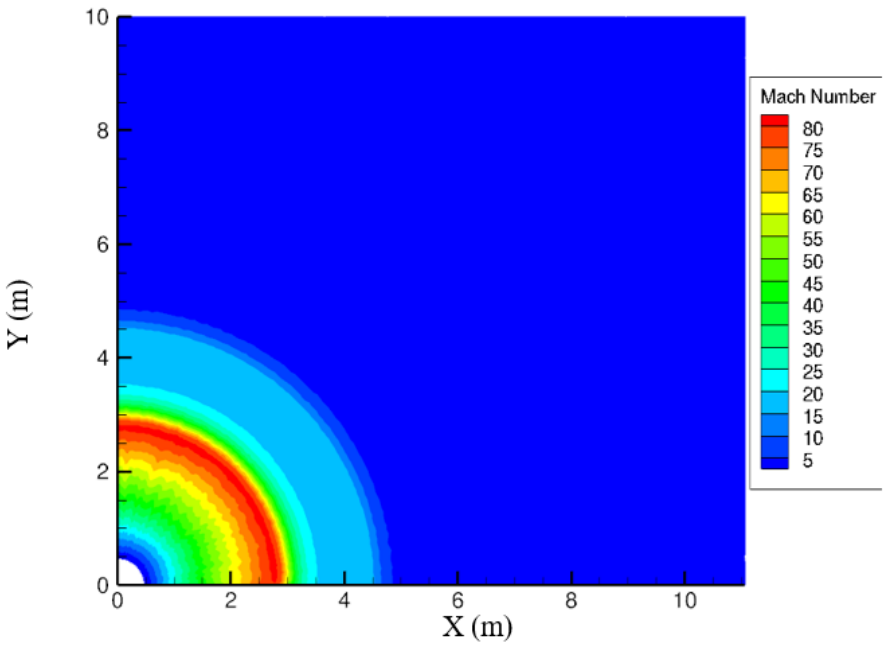

Figure 23. Mach Distribution at 0.5 ms for 500 kg R-K

The Mach number values after 0.5 milliseconds were not close to the values found after the expenditure of the RDX material. The Mach number values, Mach 80 being the highest, were extremely too high to be accurate. The error in Mach number occurred because the physical results were traveling faster than the numerical results.

The high Mach number values continued into the 1.25 millisecond results (see Figure 24).

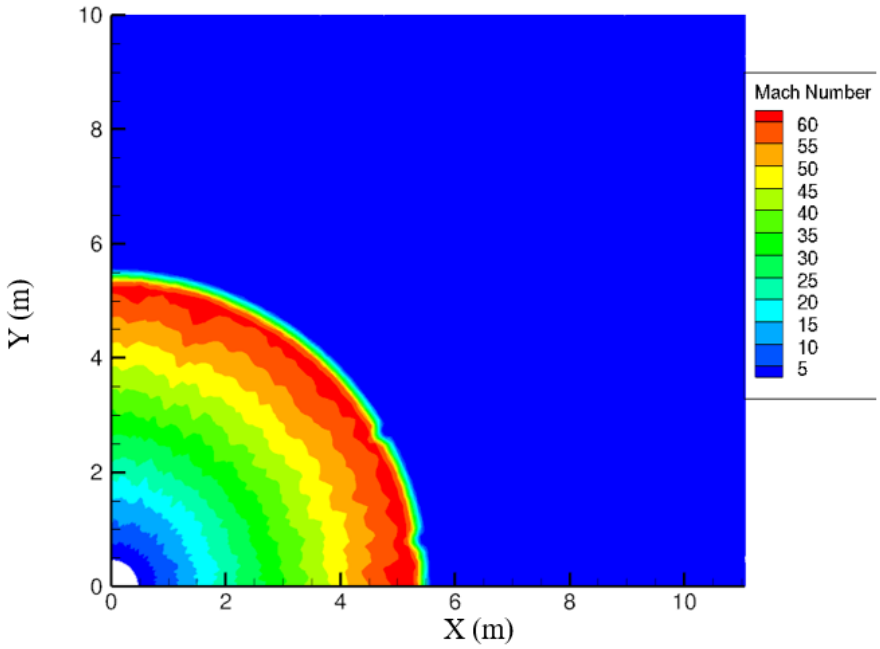

Figure 24. Mach Distribution at 1.25 ms for 500 kg R-K

However, the Mach numbers did start to decrease in value compared to the previous times results. The outer edge of Mach number profile was located at a distance shorter than the pressure wave at the same time frame.

The high Mach number results found during the previous time frames did not continue with the rest of the Mach number results found in the 500 kg Runge-Kutta wave simulation. The highest Mach number value found in the first Mach number profile at 2.5 milliseconds was Mach 2 (see Figure 25). Additionally, the first Mach profile's outer edge realigned to the same distance from the explosive's center as the pressure profile's outer edge.

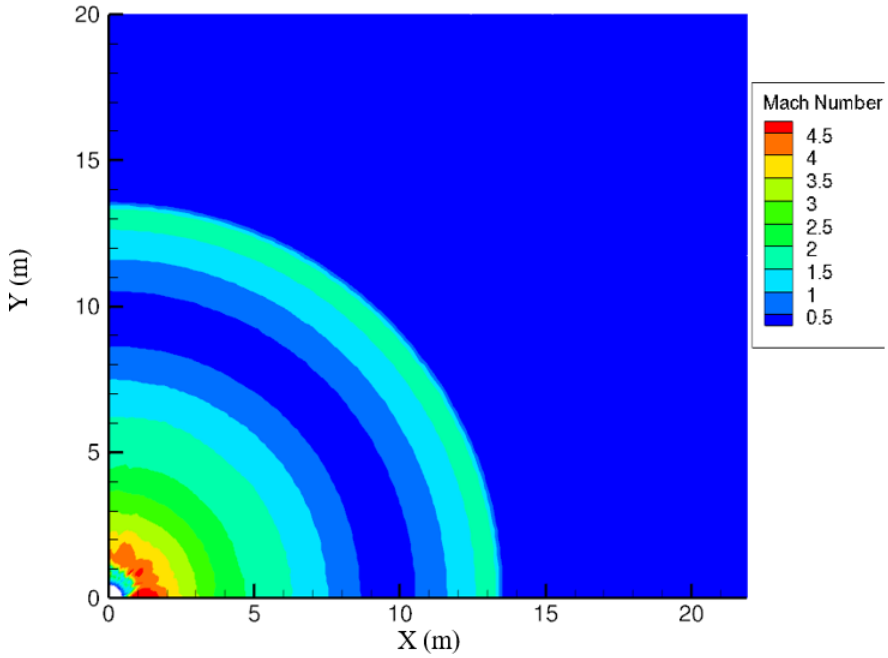

Figure 25. Mach Number Distribution at 2.5 ms for 500 kg R-K

The Mach number distribution broke up into two distinct profiles at 2.5 milliseconds. The two Mach number profiles could be explained by a secondary reaction or afterburn occurring after the explosion. However, the second Mach number profile would have appeared at 5 milliseconds to match with the pressure results. Therefore, the split was caused from the propagation of the error that occurred in the previous time step.

By 10 milliseconds, both Mach number profiles' outer edges realigned with the two pressures' outer edges. Additionally, the distance between the two profiles at 25 milliseconds was the same as the distance found between the two pressure profiles. Both profiles continued to behave similarly with Mach number values decreasing steadily as the profiles traveled outwards from the origin over time (see Figure 26).

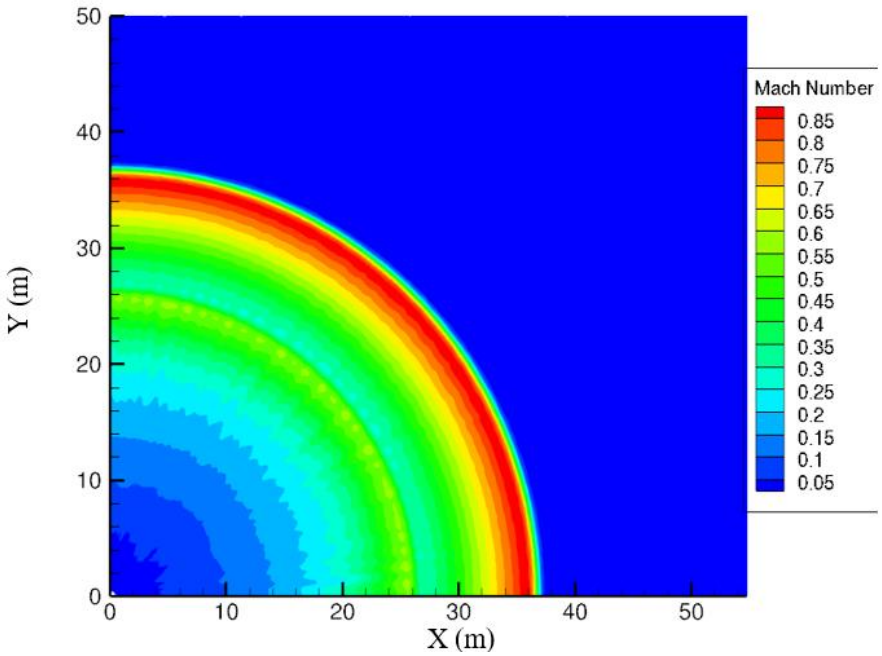

Figure 26. Mach Number Distribution at 25 ms for 500 kg R-K

500 kg Diagonalized Approximate Factorization

The 500 kg explosive was also run using DAF as the solving scheme instead of Runge-Kutta. The DAF scheme was used to further validate the results found using the Runge-Kutta solving scheme. The explosion simulation ran for a total of 35 microseconds with a time step of 0.175 microseconds to show the complete expenditure of the explosive material. The small time step used in DAF compared to the 0.35 microseconds used in Runge-Kutta was required to get VULCAN to run.

Both the pressure and Mach number distributions were similar to those from the Runge-Kutta run (see Figure 27 and Figure 29). However, the temperature distribution had more of a difference between the two (see Figure 28).

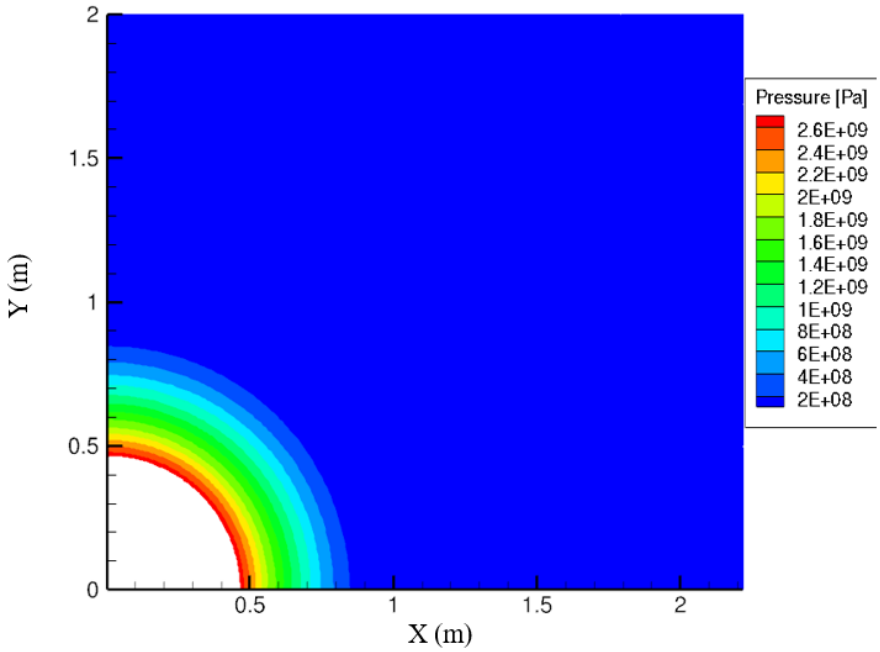

Figure 27. Pressure Distribution at 35 μs for 500 kg DAF

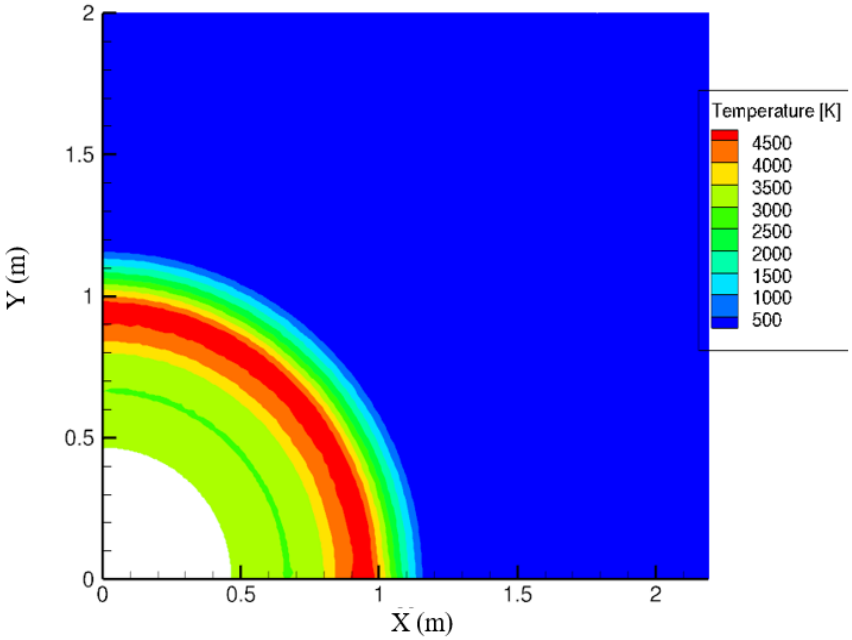

Figure 28. Temperature Distribution at 35 μs for 500 kg DAF

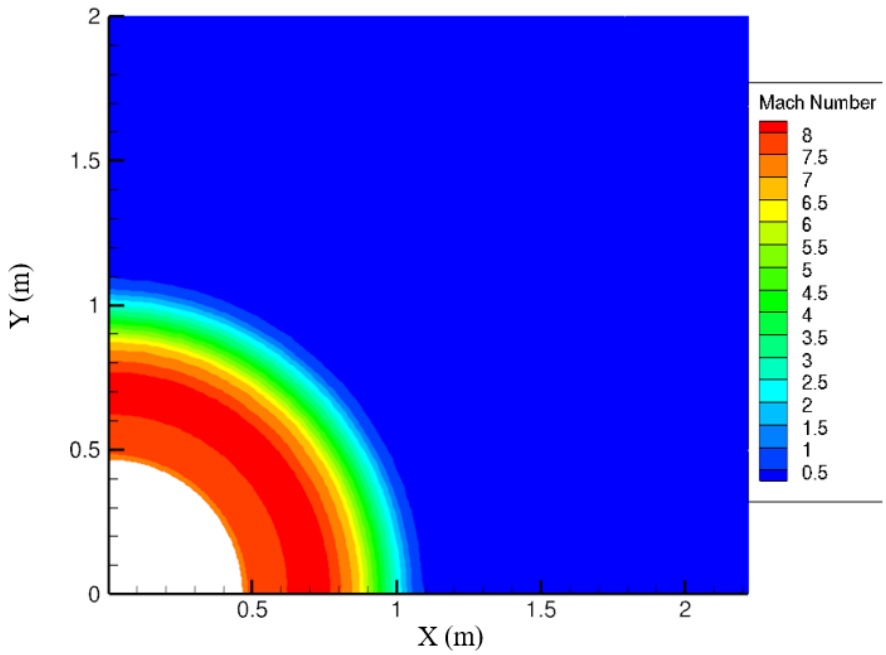

Figure 29. Mach Distribution at 35 μs for 500 kg DAF

There were two major differences between the DAF and Runge-Kutta temperature results. The first major difference was the temperature profile highest value, 4500 K, was lower than the Runge-Kutta results by 1000 K. The second major difference was the additional layer of temperature in the origin area under the highest temperature layer. These differences were caused because only one time step was used during the DAF simulations. Two time steps should be used in future DAF simulations to achieve more similar results.

The wave simulation used a time step of 2.5 nanoseconds and ran for 1.25 milliseconds. This smaller run time was required to remain within the one week computation time frame. The below figures show the pressure, temperature, and Mach number distributions at 0.5 milliseconds. At 0.5 milliseconds, the highest pressure layer was still in the middle of pressure profile matching with the Runge-Kutta results (see Figure 30). Likewise, the highest Mach number layer was also located towards the

middle of the Mach number profile (see Figure 31). The extremely high Mach numbers were also seen during this time. The increase in Mach number started at 25 microseconds with Mach 9.5. The Mach number rapidly increased until 62.5 microseconds where it peaked at Mach 85 before slowly decreasing. This error was caused by the same error seen in the 500 kg Runge-Kutta simulation. The temperature profile at 0.5 milliseconds matched the profile layout of the 500 kg Runge-Kutta at the same time frame (see Figure 32).

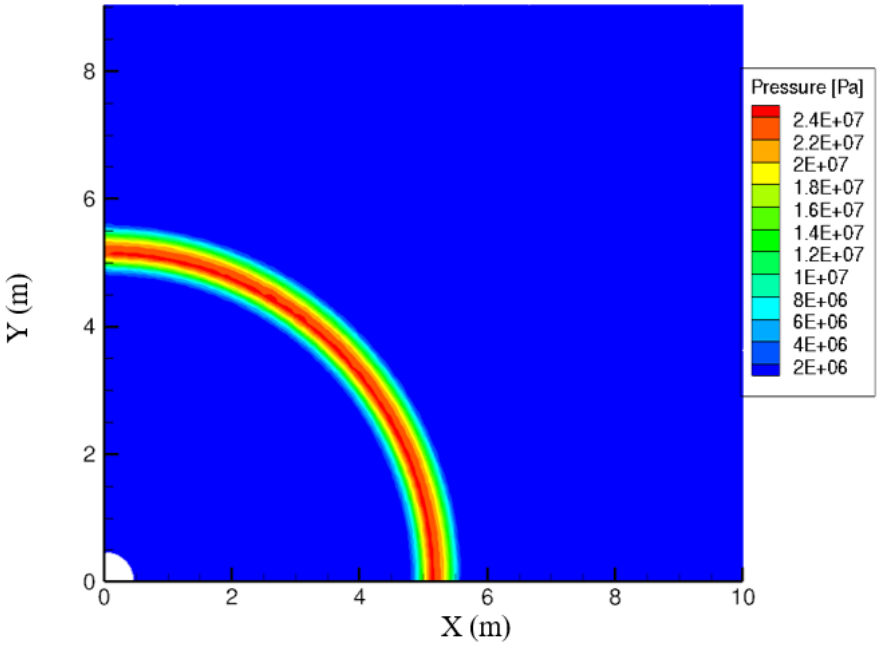

Figure 30. Pressure Distribution at 0.5 ms for 500 kg DAF

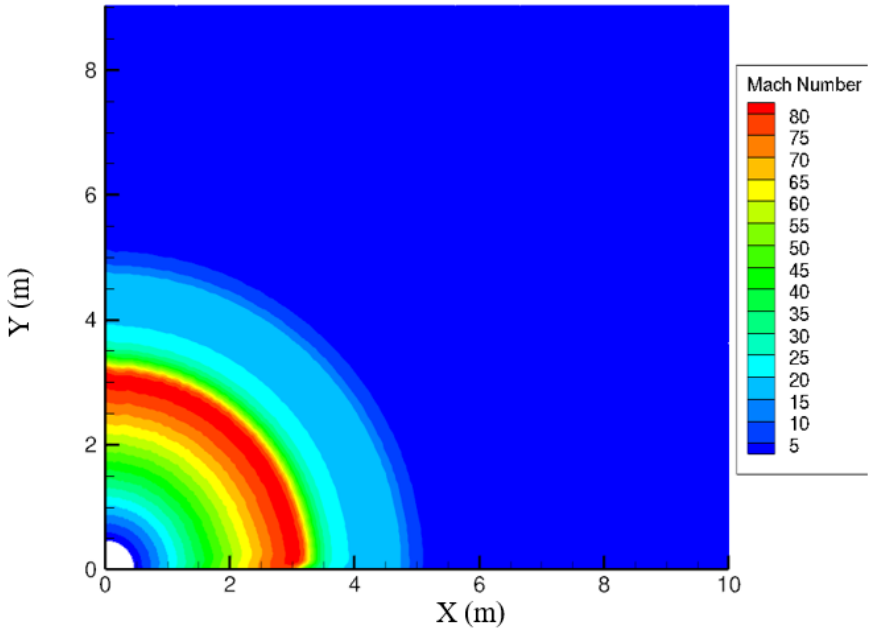

Figure 31. Mach Number Distribution at 0.5 ms for 500 kg DAF

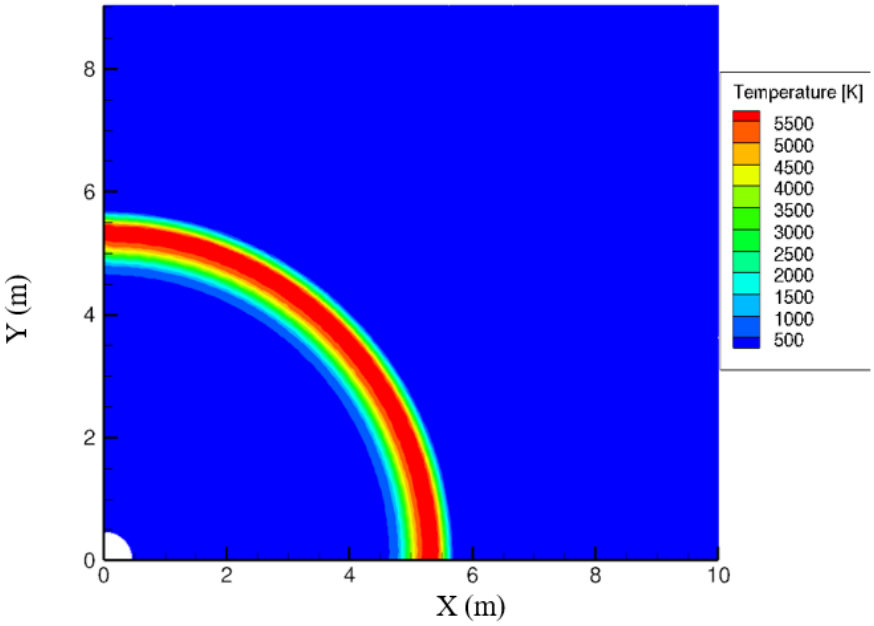

Figure 32. Temperature Distribution at **0.5 ms for 500 kg DAF**

The next set of results from the wave simulation shown below were from the 1.25 milliseconds time frame. The DAF pressure and Mach number distributions were comparable to the Runge-Kutta distributions at 1.25 milliseconds (see Figure 33 and

Figure 35). There was only a slight difference between the two schemes' Mach results in distance the profiles traveled from the origin, with DAF's Mach profile traveling 2.5 m farther. Additionally, the DAF's highest Mach number was higher than Runge-Kutta's highest Mach number by a value of 20. The temperature distribution was again different in the additional layer than the one found using Runge-Kutta (see Figure 34). The DAF temperature profile was also smaller in thickness by 2 m compared to the Runge-Kutta temperature profile.

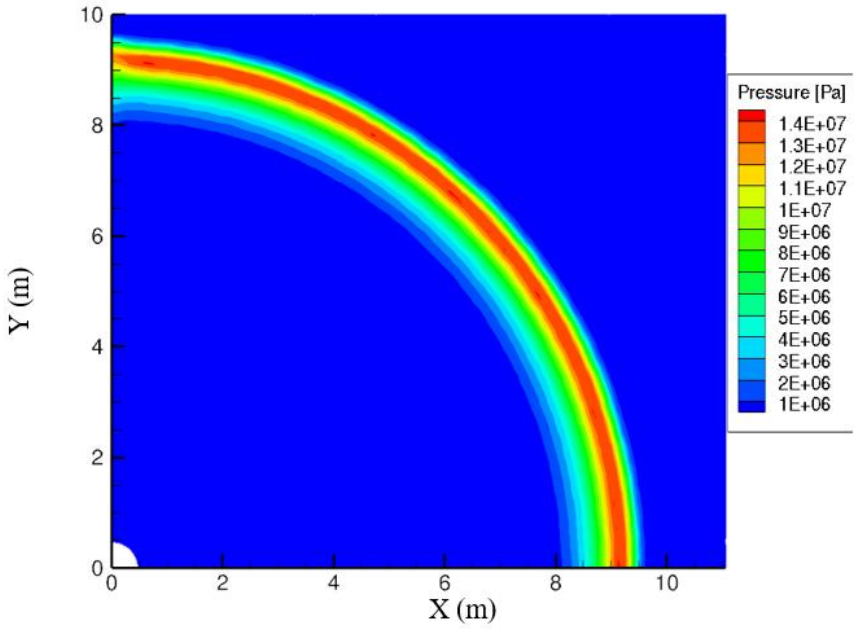

Figure 33. Pressure Distribution at 1.25 ms for 500 kg DAF

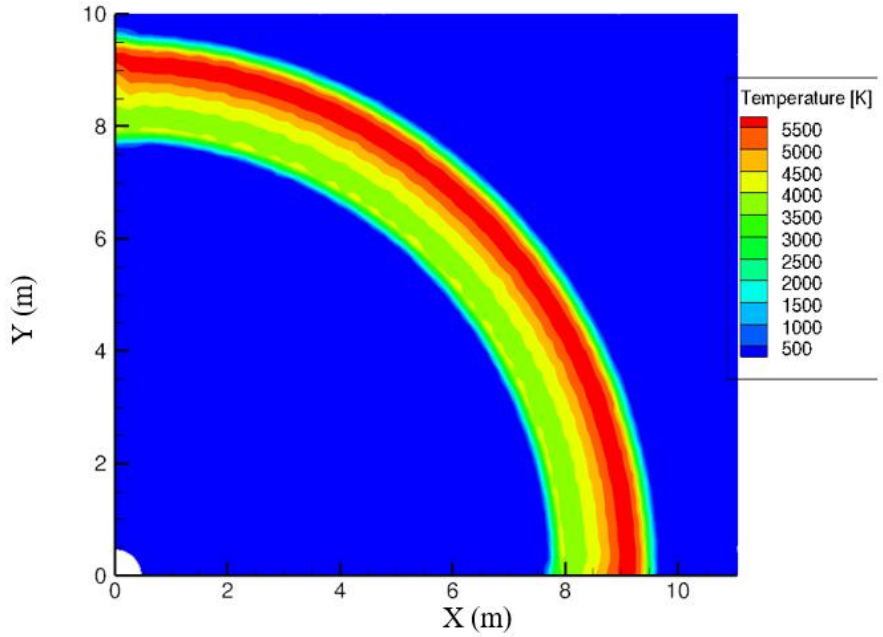

Figure 34. Temperature Distribution at 1.25 ms for 500 kg DAF

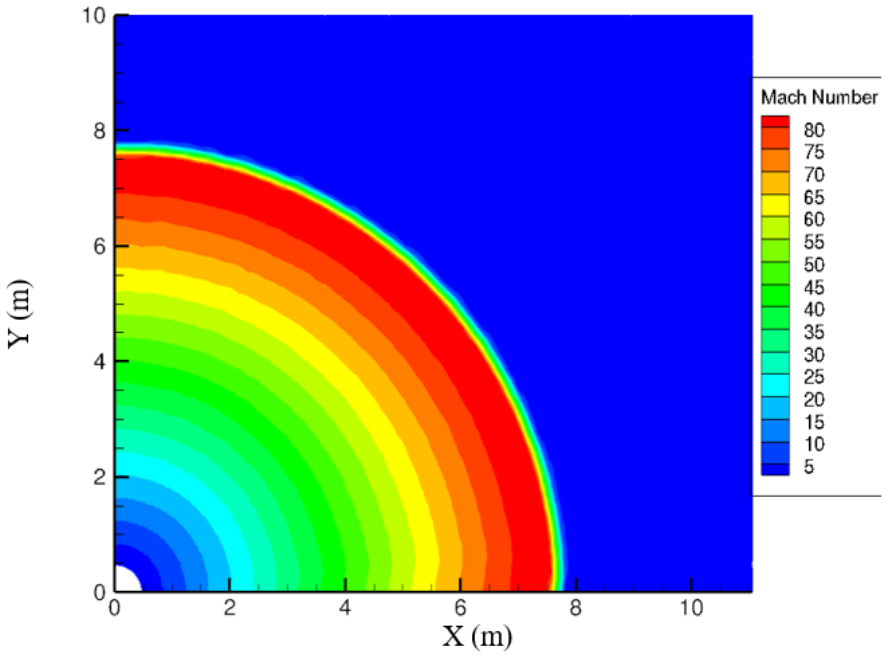

Figure 35. Mach Number Distribution at 1.25 ms for 500 kg DAF

1000 kg Runge-Kutta

For the 1000 kg explosion case, the final products from the RDX explosive, N_2, CO, and H_2O, were reported for a total of 44.1 microseconds, using a time step of 0.2205 microseconds, to show the complete expenditure of the explosive material. The resulting pressure, temperature, and Mach distributions were almost identical to the results from the 500 kg simulation. The only slight difference between the two was the 1000 kg profiles traveled a farther distance from the origin for each. This difference in distance is explained by the increase in mass size from 500 kg to 1000 kg. See Figure 36 to Figure 38 for the pressure, temperature, and Mach number results for the 1000 kg explosion simulation.

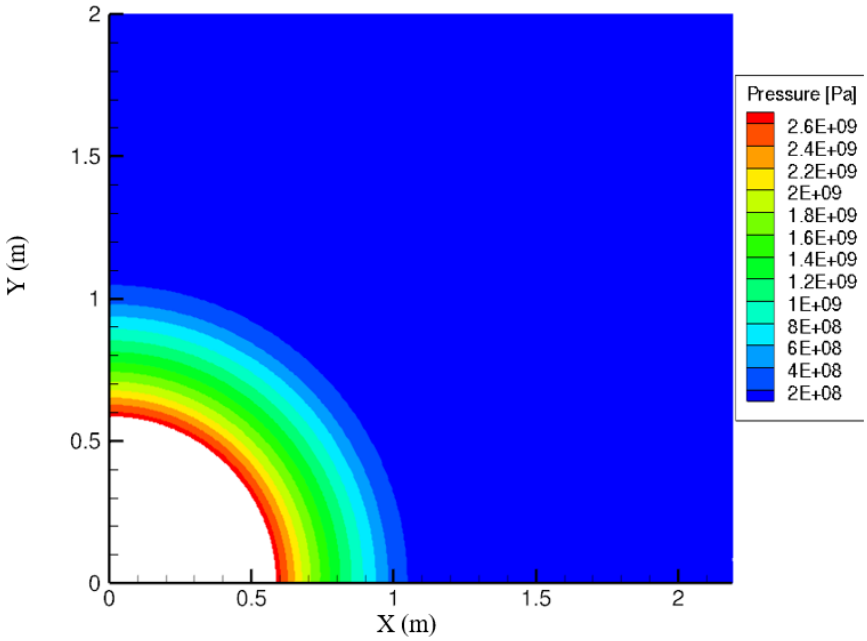

Figure 36. Pressure Distribution at 44.1 μs for 1000 kg

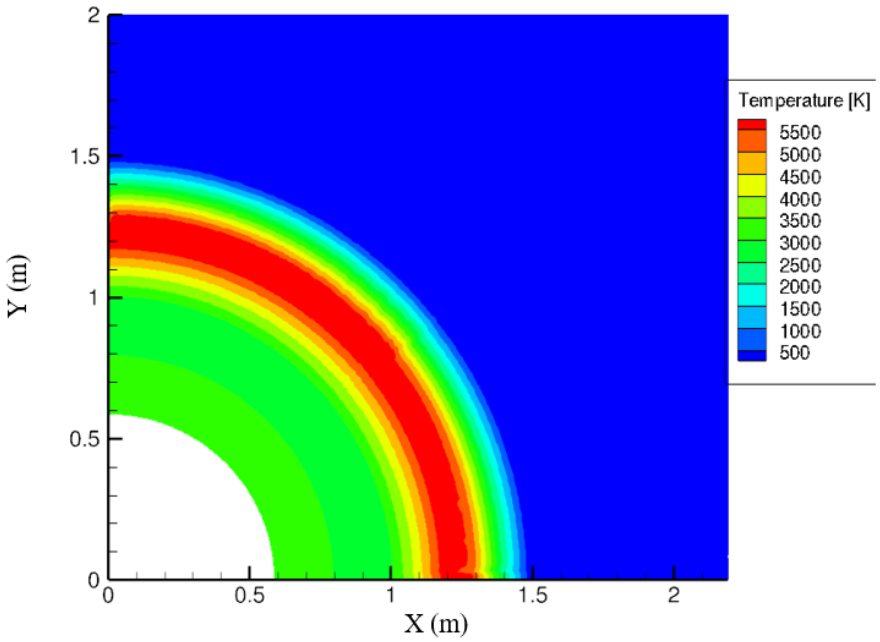

Figure 37. Temperature Distribution at 44.1 µs for 1000 kg

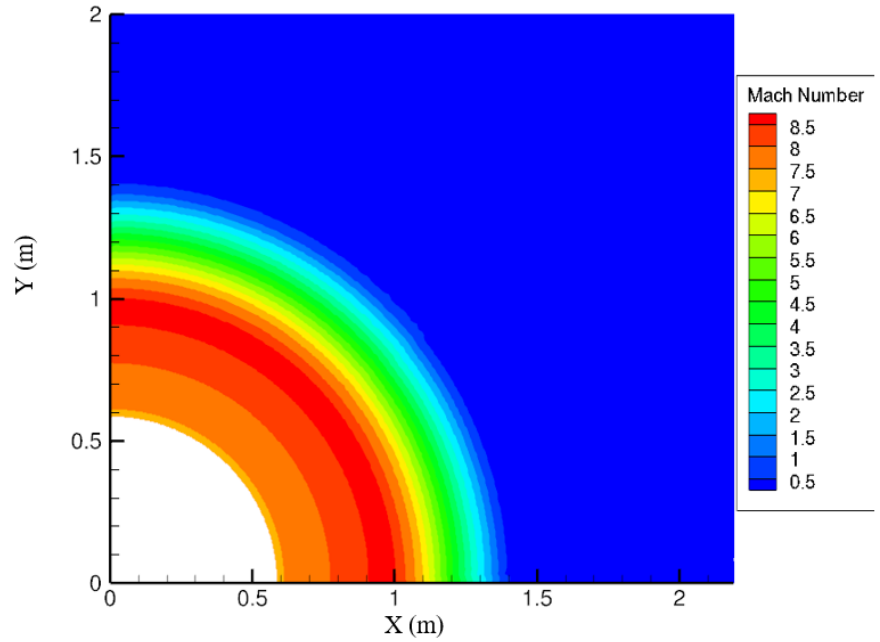

Figure 38. Mach Number Distribution at 44.1 µs for 1000 kg

After the explosion simulation was complete, the wave input file was run. The total run time of the wave simulation was 0.5 milliseconds due to the small time steps, 25 nanoseconds, required for the simulation to run as well as the long computation time

requirement. The pressure distribution for the 1000 kg wave simulation at 0.5 milliseconds looked almost identical to the 500 kg Runge-Kutta pressure distribution (see Figure 39). The Mach number profile showed a layer of slightly lower values than the highest value sandwiched in the middle of the profile by the highest Mach number layers (see Figure 40). The Mach number distribution followed the trend of very high Mach number values at the beginning time frame of the wave simulation. The temperature profile distribution matched with the results shown for the 500 kg Runge-Kutta simulation (see Figure 41). However, a second temperature located at the origin was also present. This second temperature profile was the result of afterburn occurring. The first time the second temperature profile was seen in the 1000 kg results was at 0.225 milliseconds (see Figure 42). The second temperature profile distribution was almost identical looking to the pressure profile found at the end of the explosion simulation.

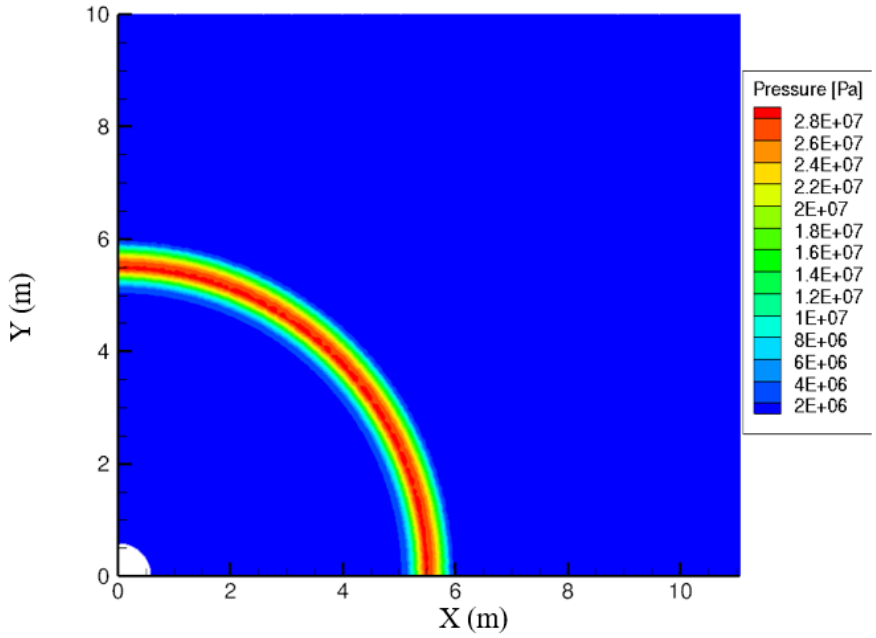

Figure 39. Pressure Distribution at 0.5 ms for 1000 kg

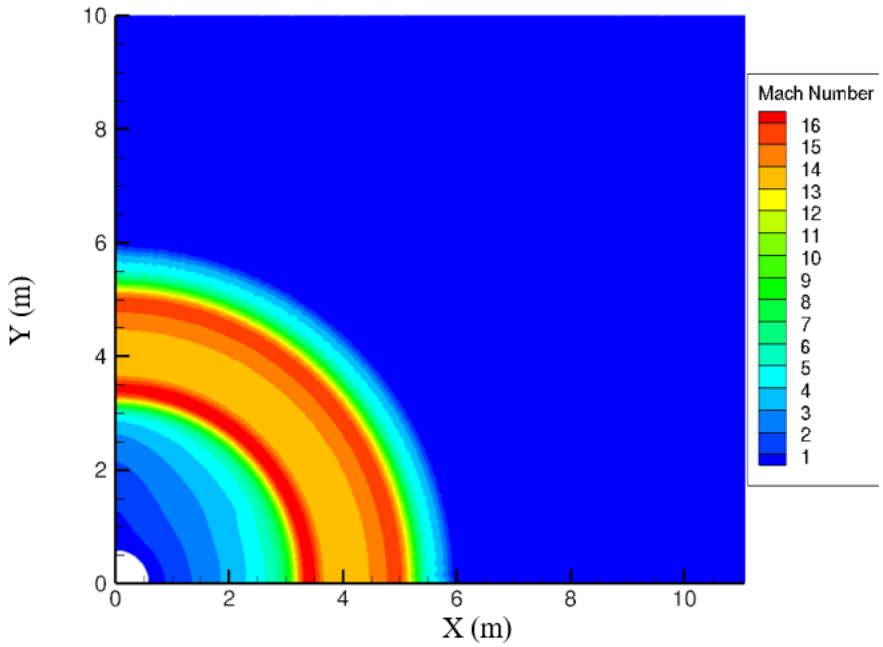

Figure 40. Mach Distribution at 0.5 ms for 1000 kg

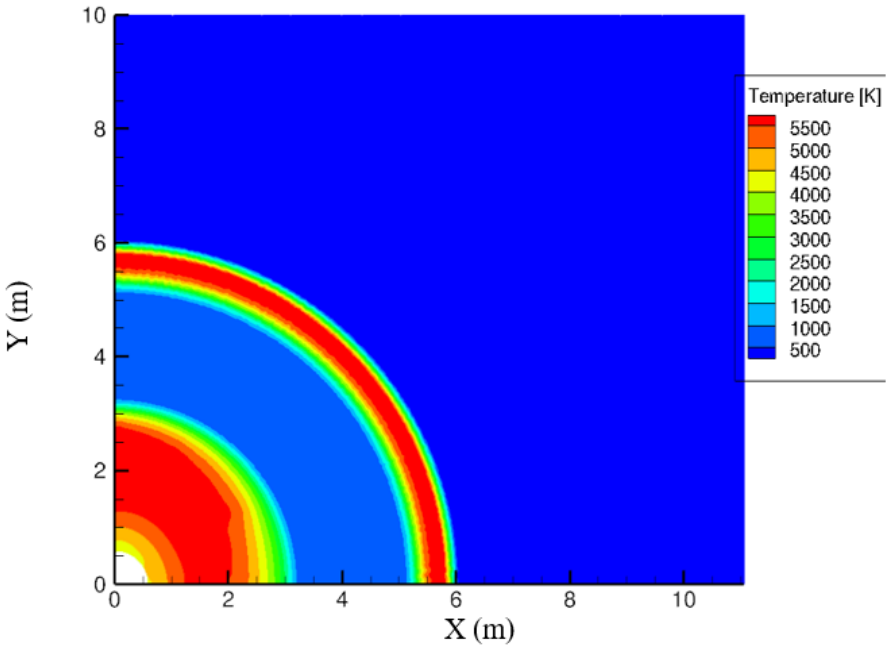

Figure 41. Temperature Distribution at 0.5 ms for 1000 kg

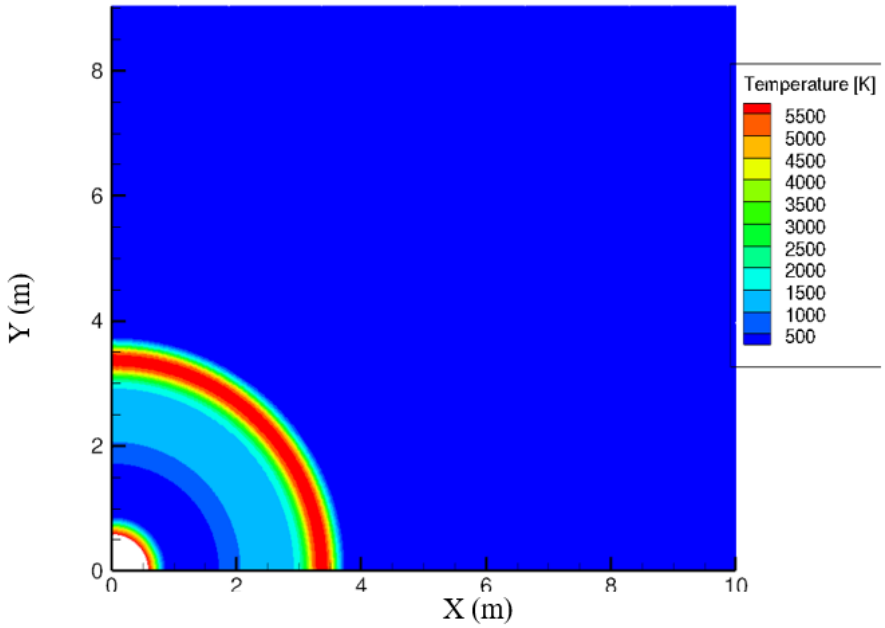

Figure 42. Temperature Distribution at 0.225 ms for 1000 kg

2000 kg Runge-Kutta

For the 2000 kg explosion input file, the final products from the RDX explosive, N_2, CO, and H_2O, were reported for a total of 55.6 microseconds, using 0.278 microseconds time steps, to show the complete expenditure of the explosive material. The resulting pressure, temperature, and Mach distributions were almost identical to the results from the 500 kg and 1000 kg simulations. Comparable to the 1000 kg pressure, temperature, and Mach number results, a slight difference in the distance traveled was seen. However, there was also another difference found in the temperature and Mach number distributions. The outer edge of the profile was not completely smooth along the entire edge. These slight dips along the profile were explained by the 2000 kg grid having a larger radial spacing compared to the 1000 kg grid. See Figure 43 to Figure 45 for the pressure, temperature, and Mach number results for the 2000 kg explosion simulation.

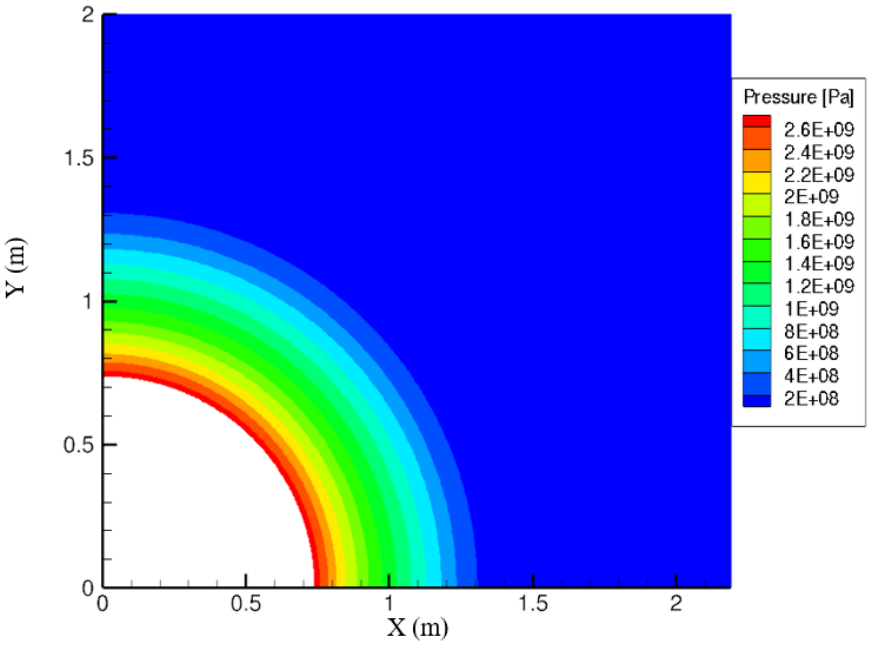

Figure 43. Pressure Distribution at 55.6 μs for 2000 kg

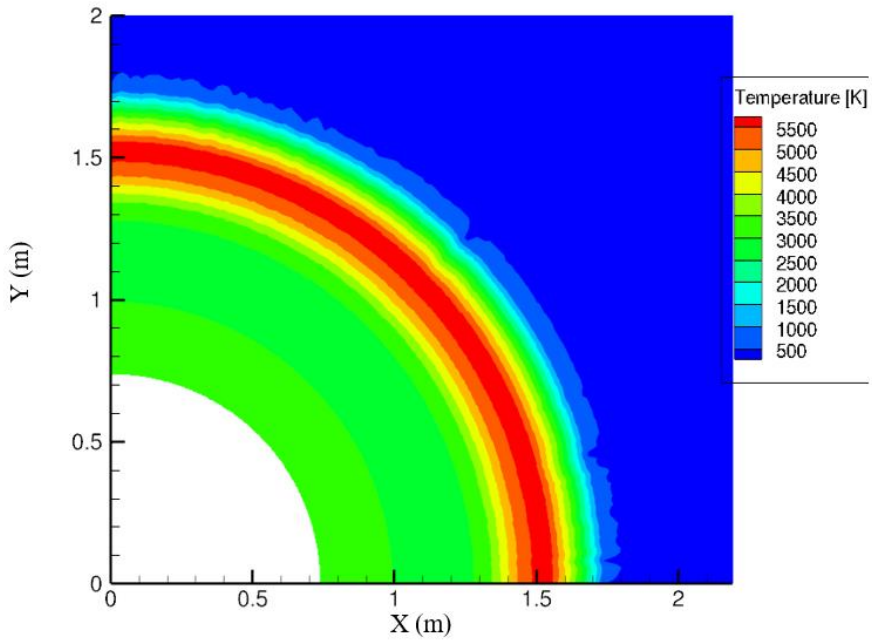

Figure 44. Temperature Distribution at 55.6 μs for 2000 kg

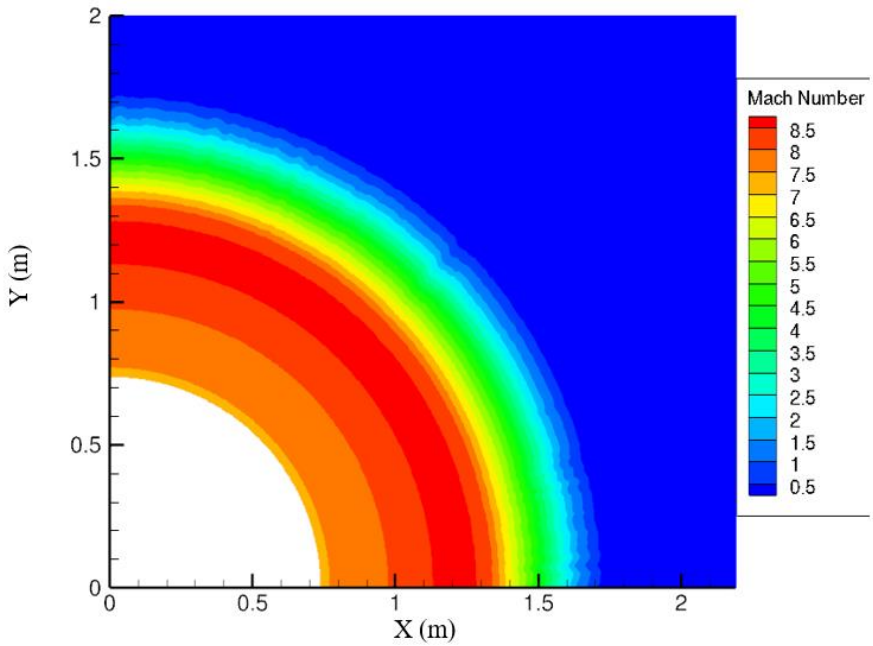

Figure 45. Mach Number Distribution at 55.6 μs for 2000 kg

After the explosion simulation was complete, the wave input file was run. The total run time and time steps used in the wave simulation were identical to the 1000 kg wave simulation. The pressure, Mach number, and temperature profile distribution patterns for the 2000 kg simulation matched almost identically to the 1000 kg profile distribution patterns at 0.5 milliseconds (see Figure 46 to Figure 49). The only difference between the results from the two masses was caused from the differences noted from the increase in mass. The second temperature profile, matching with the 1000 kg results, was first seen at 0.225 milliseconds.

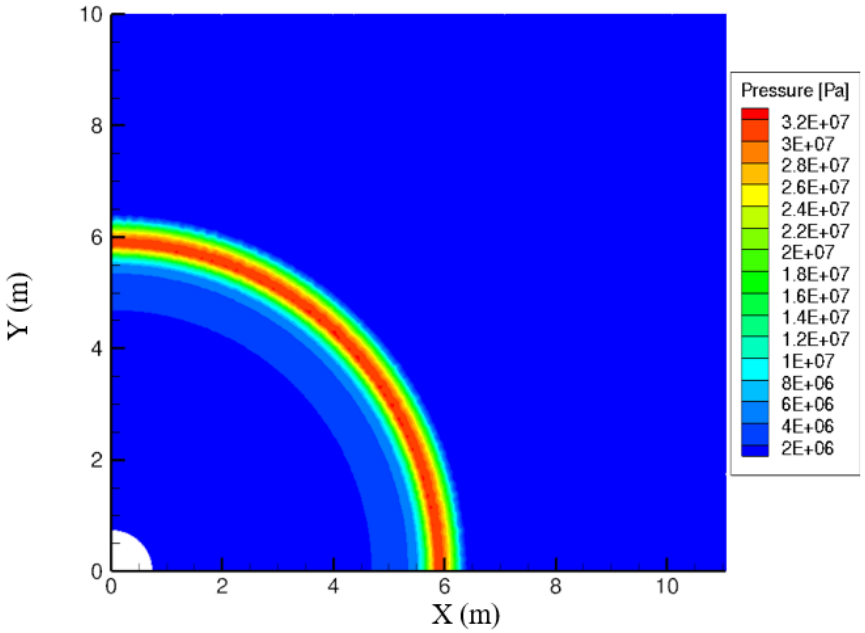

Figure 46. Pressure Distribution at 0.5 ms for 2000 kg

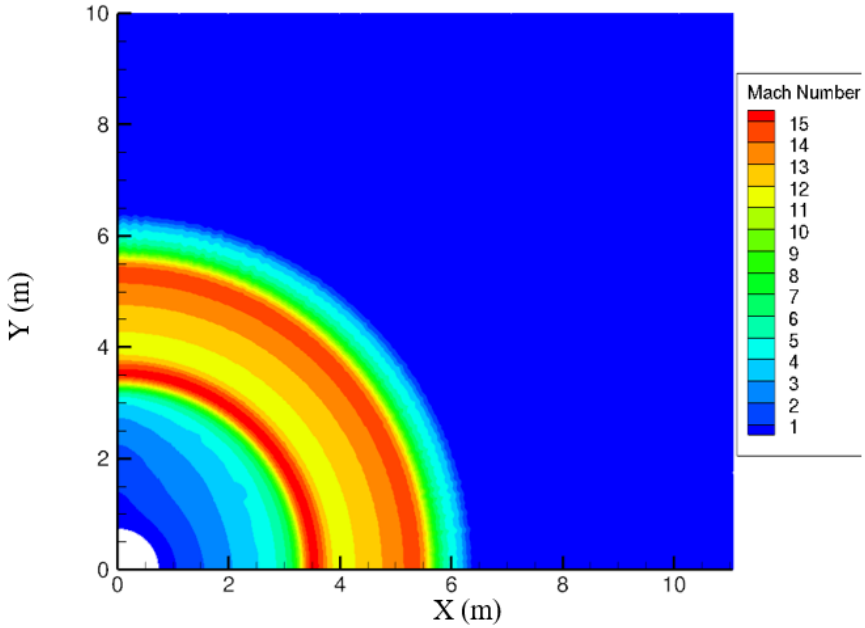

Figure 47. Mach Number Distribution at 0.5 ms for 2000 kg

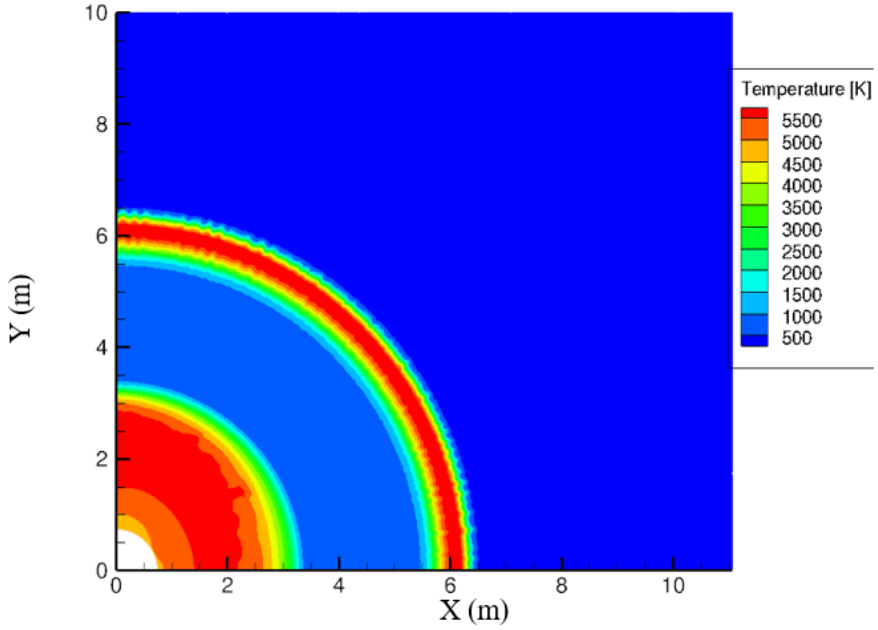

Figure 48. Temperature Distribution at 0.5 ms for 2000 kg

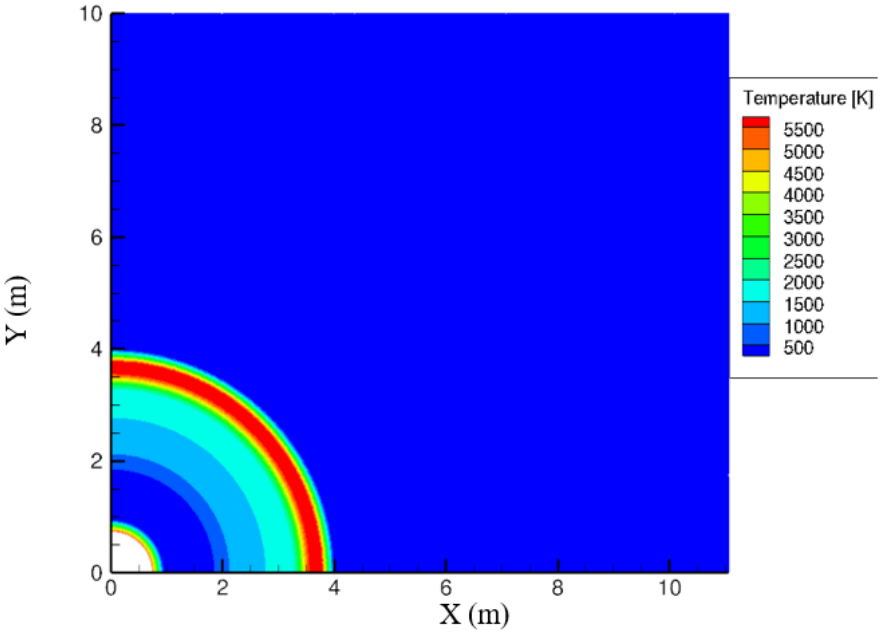

Figure 49. Temperature Distribution at 0.225 ms for 2000 kg

Chemical Results

Chemical results were the second type of important results reported by the thermophysics simulations. This thesis research specifically looked at the CO, CO_2, and

H_2O mass fractions. CO_2, and H_2O mass fractions were selected because they could be used in the future when predicting with explosive's infrared signatures. CO was also examined as a sort of sanity check, because it was one of the original product species from RDX before it reacted and became CO_2.

500 kg Runge-Kutta

At the end of running the explosion simulation, the mass fraction of 0.378 for CO was located at the origin, with the mass fraction decreasing when traveling in the direction away from the origin (see Figure 50). This distribution in CO was to be expected, because CO does not want to stay that species. Instead, CO wants to react with O_2 to become CO_2. The results of this reaction can be seen in Figure 51, with the CO_2 having been formed already during the 35 microseconds. The amount of H_2O mass fraction (see Figure 52) found at the end of the explosion simulation followed the same pattern as CO. However, its overall values were decreased, because a mass fraction of only 0.244 H_2O was produced from the explosive.

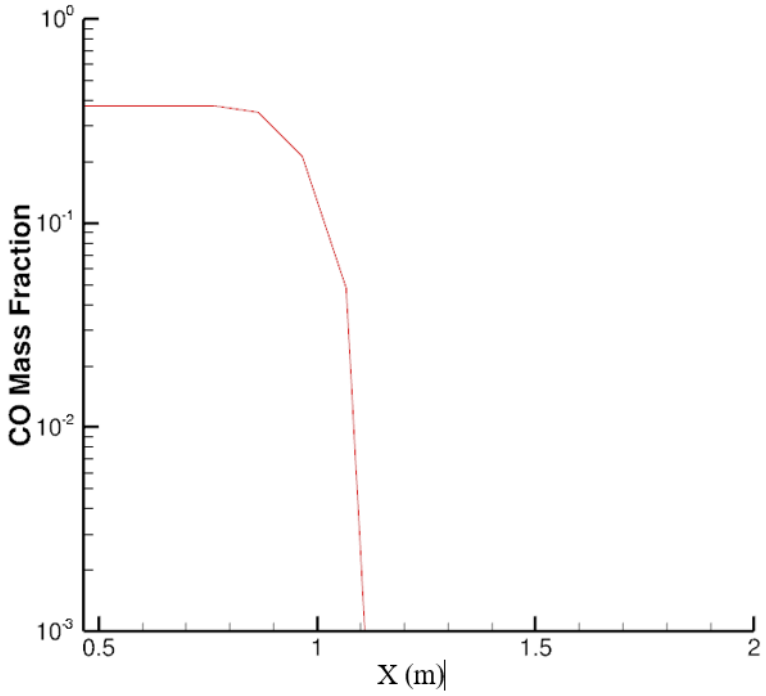

Figure 50. CO Mass Fraction Distribution at 35 μs for 500 kg R-K

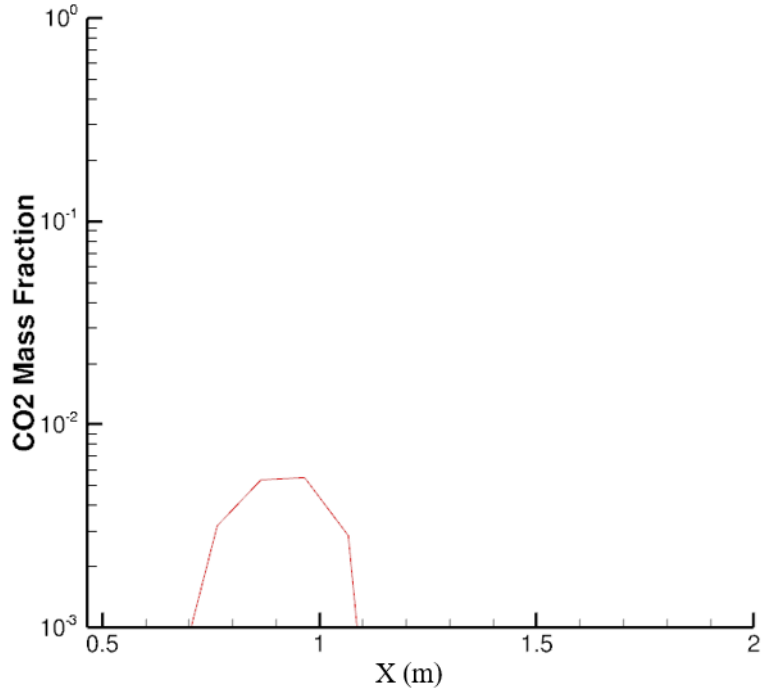

Figure 51. CO_2 Mass Fraction Distribution at 35 μs for 500 kg R-K

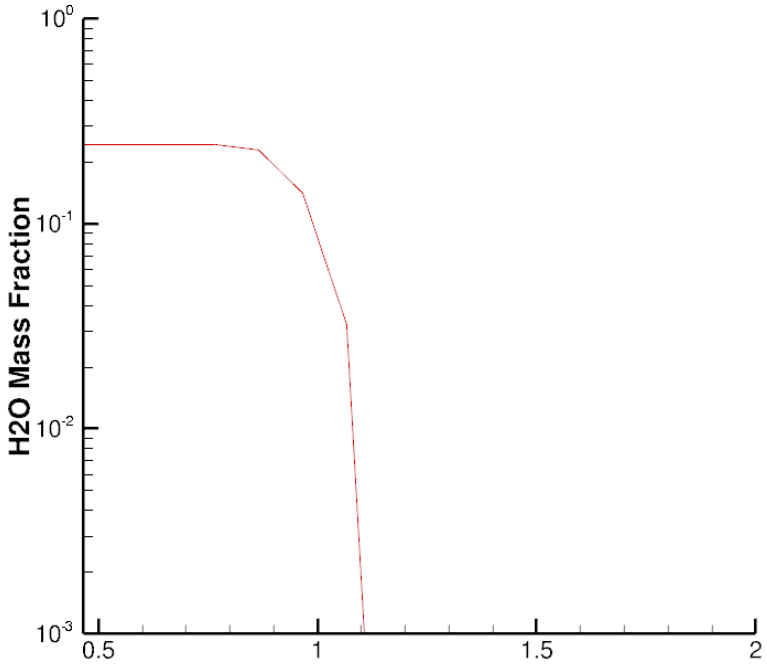

Figure 52. H_20 Mass Fraction Distribution at 35 μs for 500 kg R-K

At 0.5 milliseconds, all three species have traveled around the same distance as the aerothermal results. The distribution patterns for CO and H_2O at 0.5 milliseconds were the same as right after the explosive completely expended (see Figure 53 and Figure 55). The only difference between the two time frames was the distance the mass fraction profiles had expanded outwards. The pattern for the mass fraction of CO_2 also remained the same, but its concentration increased slightly due to more CO reacting and becoming CO_2 (see Figure 54). This increase in CO_2 corroborates the 500 kg Runge-Kutta aerothermal results in having an afterburn occur.

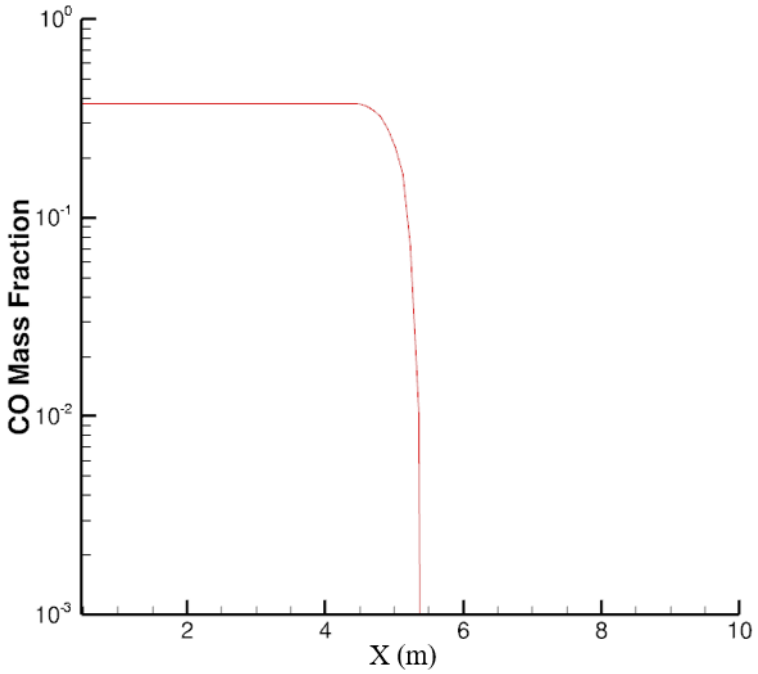

Figure 53. CO Mass Fraction Distribution at 0.5 ms for 500 kg R-K

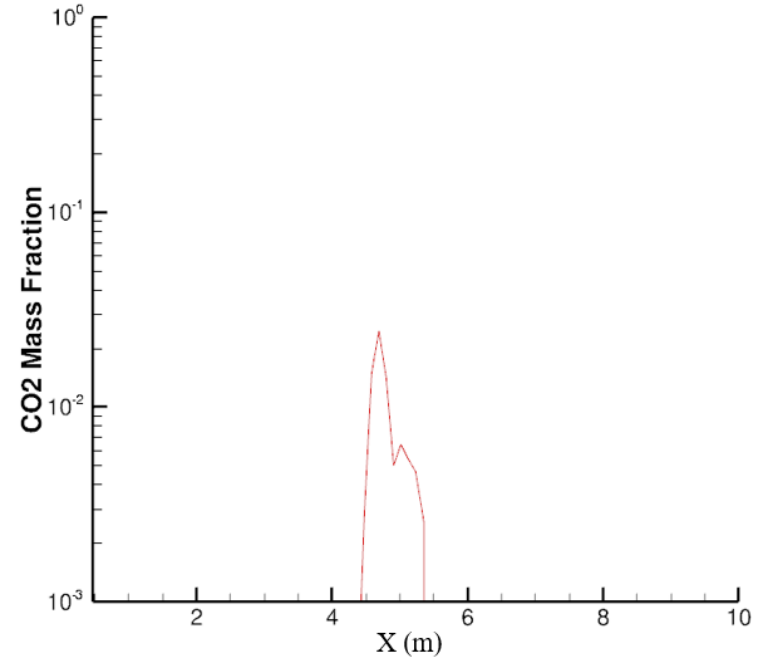

Figure 54. CO_2 Mass Fraction Distribution at 0.5 ms for 500 kg R-K

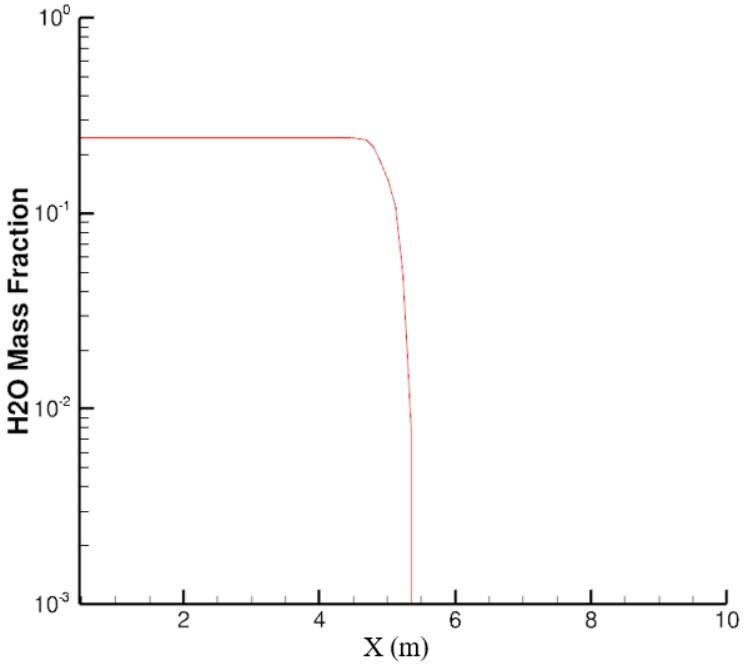

Figure 55. H_2O Mass Fraction Distribution at 0.5 ms for 500 kg R-K

At 1.25 milliseconds, all three species have traveled around the same distance as the aerothermal results. The distribution patterns for CO and H_2O at 1.25 milliseconds were the same as the 0.5 millisecond results (see Figure 56 and Figure 58). The only difference between the two time frames was the distance the mass fraction profiles had expanded outwards. The pattern for the mass fraction of CO_2 continued to increase and expand due to more CO reacting and becoming CO_2 (see Figure 57).

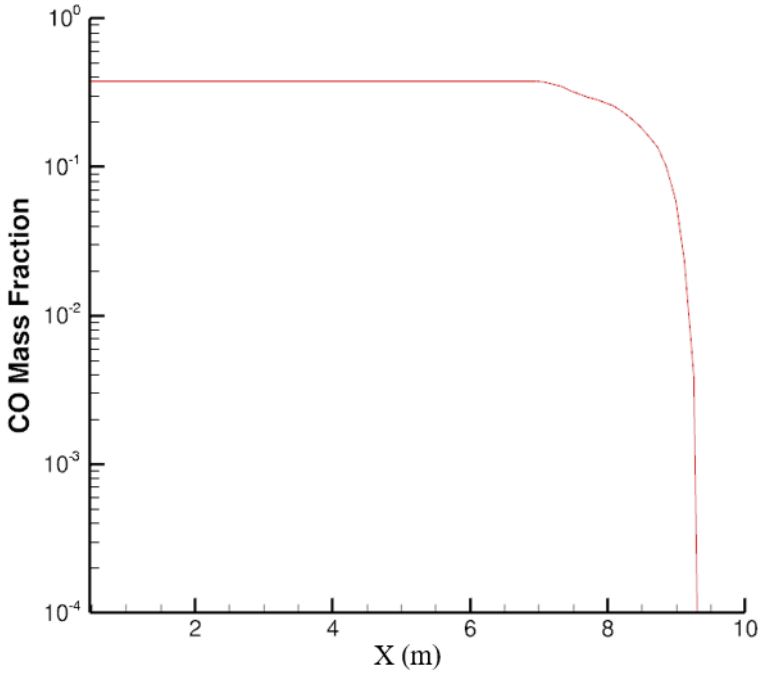

Figure 56. CO Mass Fraction Distribution at 1.25 ms for 500 kg R-K

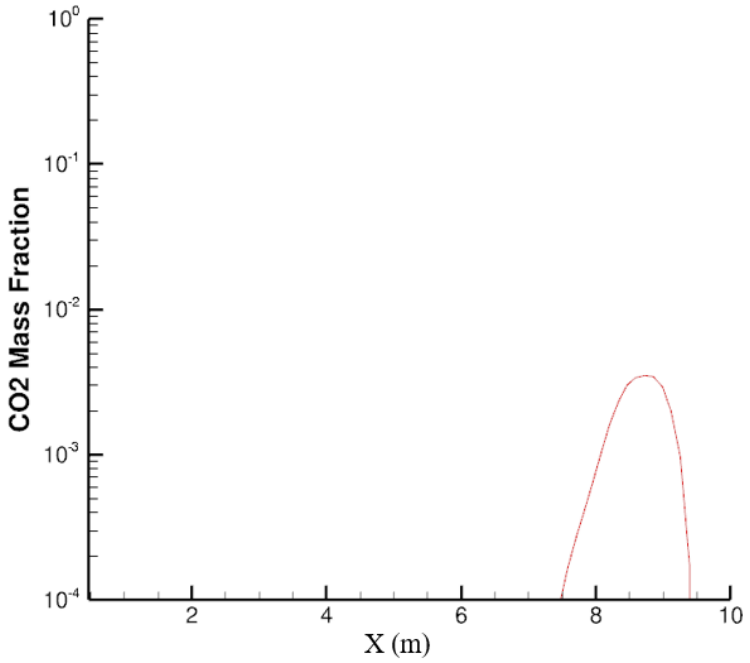

Figure 57. CO_2 Mass Fraction Distribution at 1.25 ms for 500 kg R-K

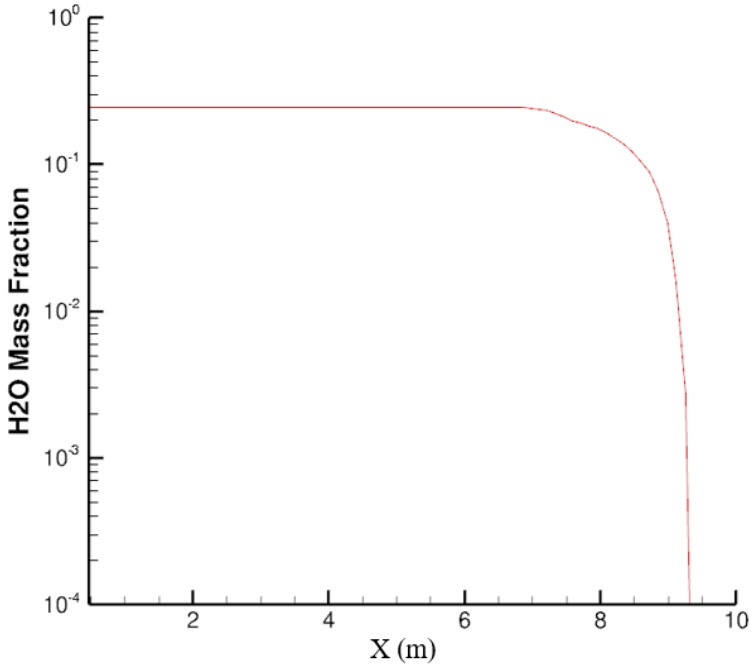

Figure 58. H_20 Mass Fraction Distribution at 1.25 ms for 500 kg R-K

At 25 milliseconds, the mass fraction of CO found in the air had further been reduced, and the beginning concentration of 0.378 was no longer seen (see Figure 59). However, some of the CO was still able to travel through the air. The concentration of CO_2 further increased during the time frame and expanded to cover more distance (see Figure 60). The mass fraction profile distribution pattern of H_2O continued to follow the same trend that was found between the explosive being completely expended and 2.5 milliseconds (see Figure 61). The three species' distributions did not reach the same distance as the aerothermal distributions during the same time step. There was a difference of around 14 meters. This trend started at 6.25 milliseconds.

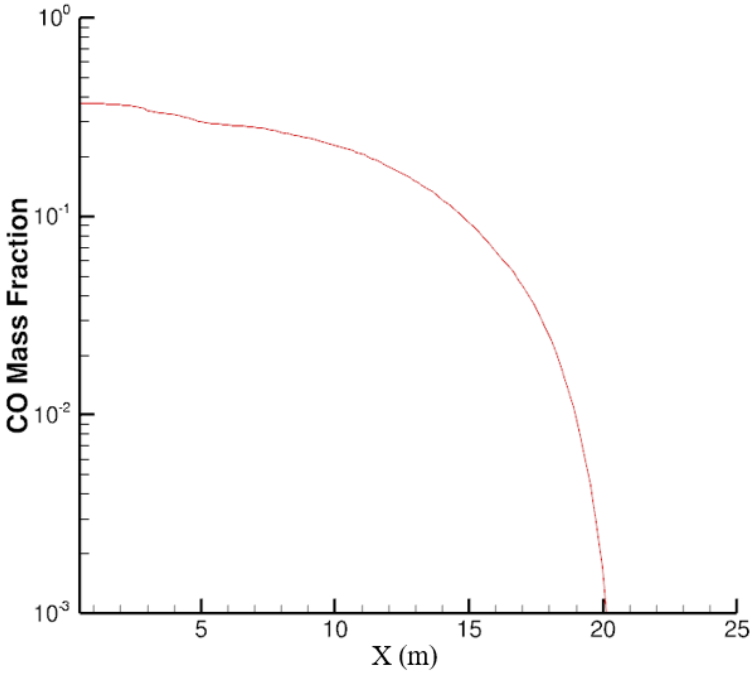

Figure 59. CO Mass Fraction Distribution at 25 ms for 500 kg R-K

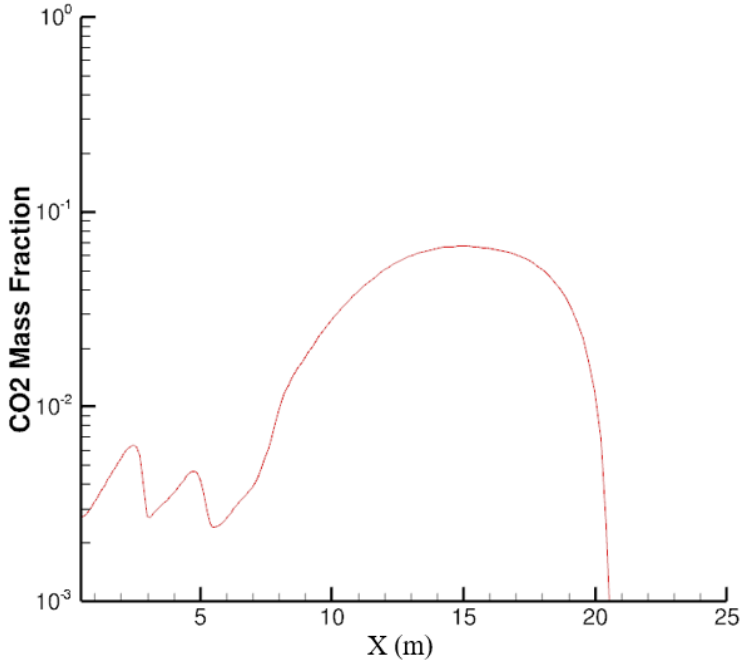

Figure 60. CO_2 Mass Fraction Distribution at 25 ms for 500 kg R-K

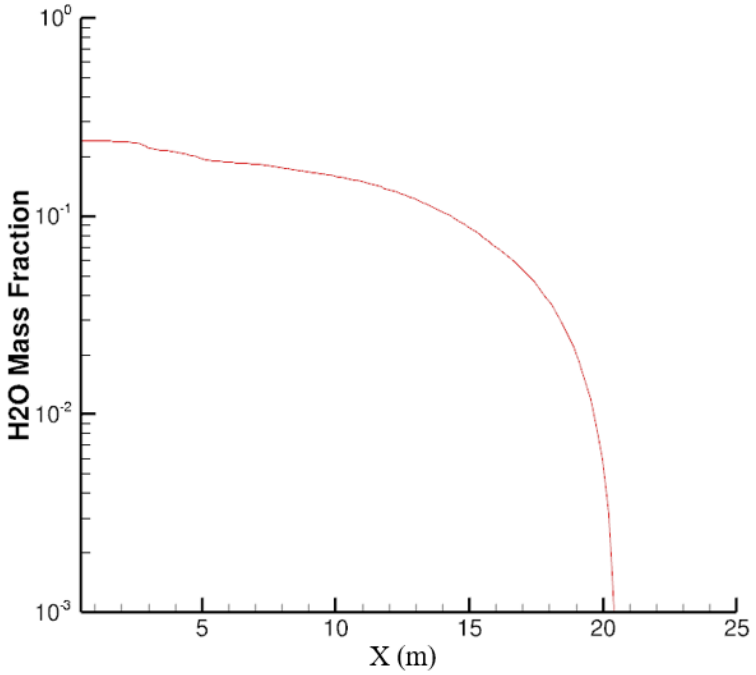

Figure 61. H_2O Mass Fraction Distribution at 25 ms for 500 kg R-K

500 kg Diagonalized Approximate Factorization

The mass fractions found at the end of the explosion simulation for the DAF solving scheme were slightly different compared to the Runge-Kutta results. For CO, the highest mass fraction value of CO, 0.378, remained the same (see Figure 62), but all other mass faction values were lower compared to the Runge-Kutta results. To match with the decrease in CO found in the DAF simulation, the mass fraction values for CO_2 were higher than the Runge-Kutta results (see Figure 63). The differences in the H_2O mass fraction values followed the same pattern as the CO mass fraction values between DAF and Runge-Kutta (see Figure 64). These differences in mass fraction values were caused by the differences found in temperature distributions between the two simulations.

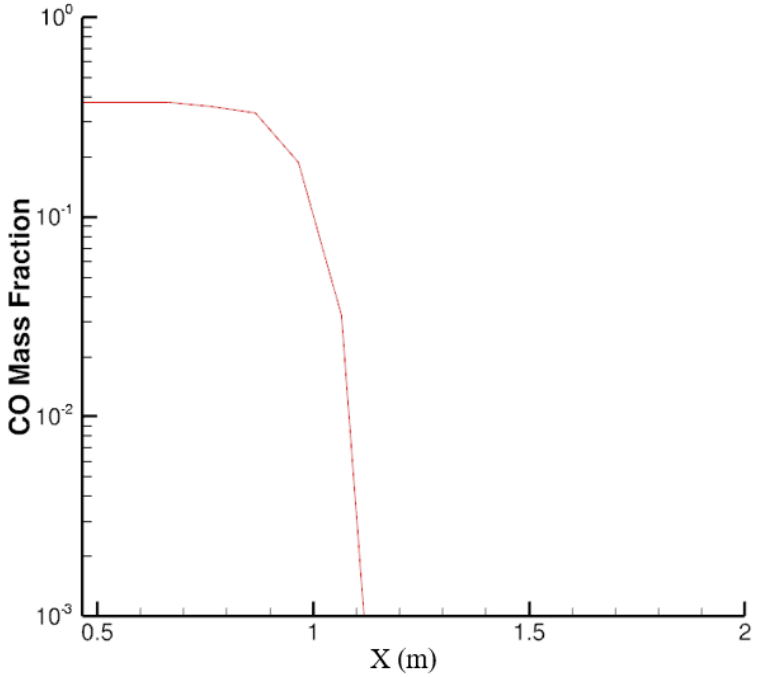

Figure 62. CO Mass Fraction Distribution at 35 μs for 500 kg DAF

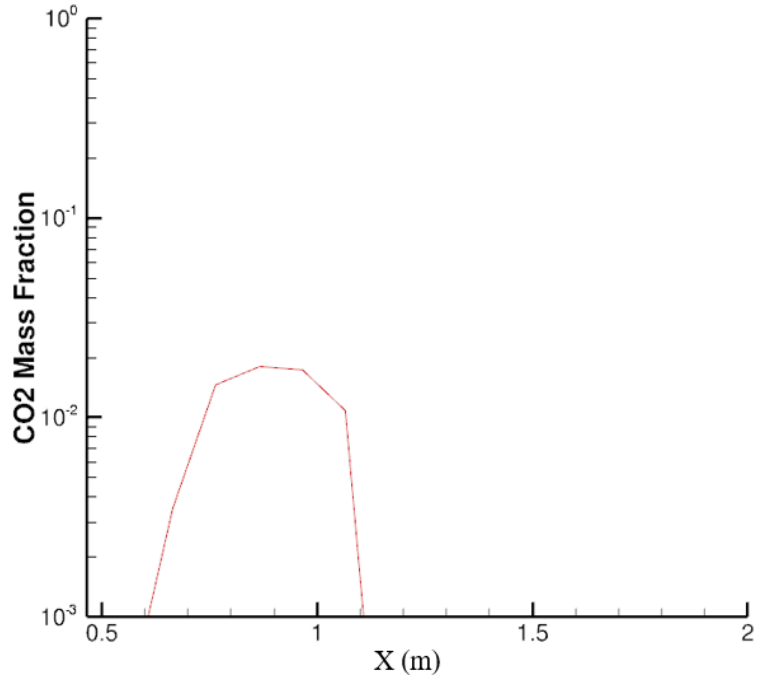

Figure 63. CO_2 Mass Fraction Distribution at 35 μs for 500 kg DAF

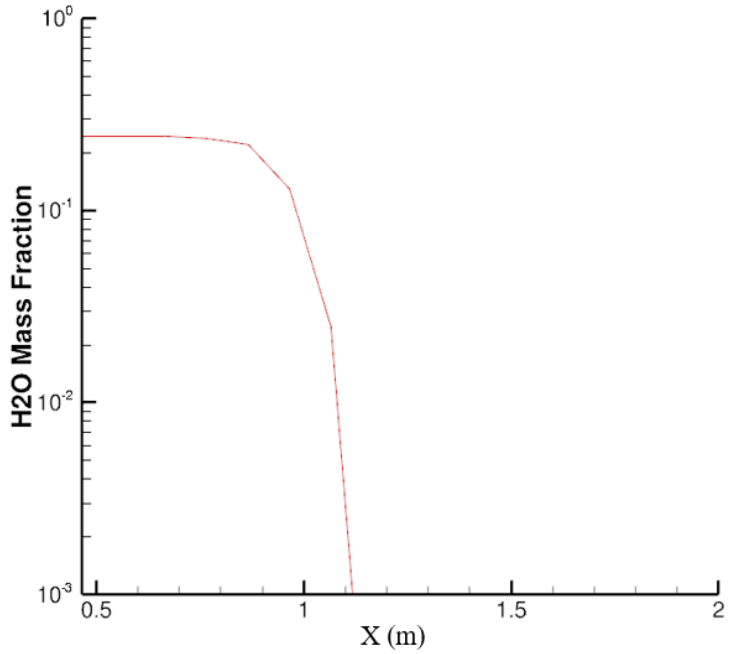

Figure 64. H_2O Mass Fraction Distribution at 35 μs for 500 kg DAF

The trends for the three mass fractions in the Runge-Kutta wave simulation were also seen throughout the DAF wave simulation, except for CO_2 at 1.25 milliseconds (see Figure 65 to Figure 70). At 1.25 milliseconds, the CO_2 mass fractions decreased. The DAF chemical result distances were farther from the center of the explosive than the Runge-Kutta distances. The difference in distances traveled matched with the differences found between the aerothermal results. The difference between the DAF and Runge-Kutta mass fraction value for CO_2 continued throughout the simulation as well.

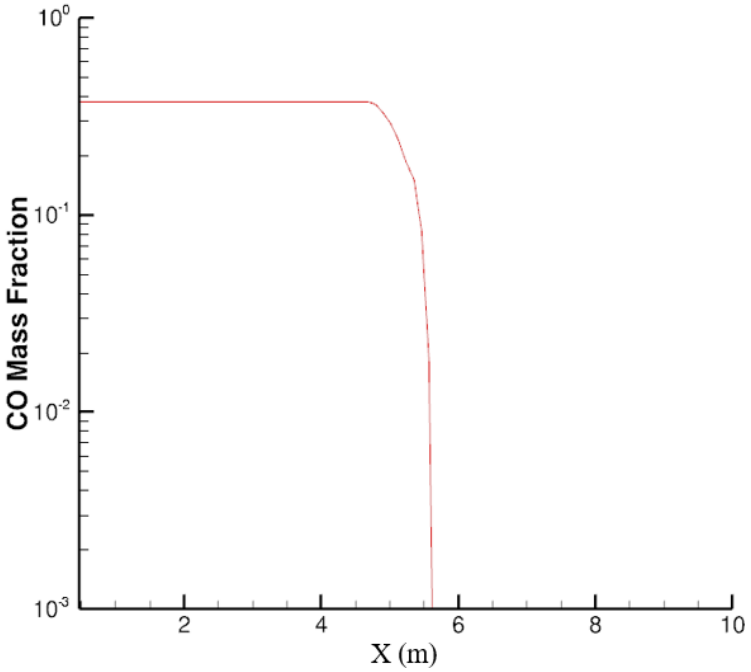

Figure 65. CO Mass Fraction Distribution at 0.5 ms for 500 kg DAF

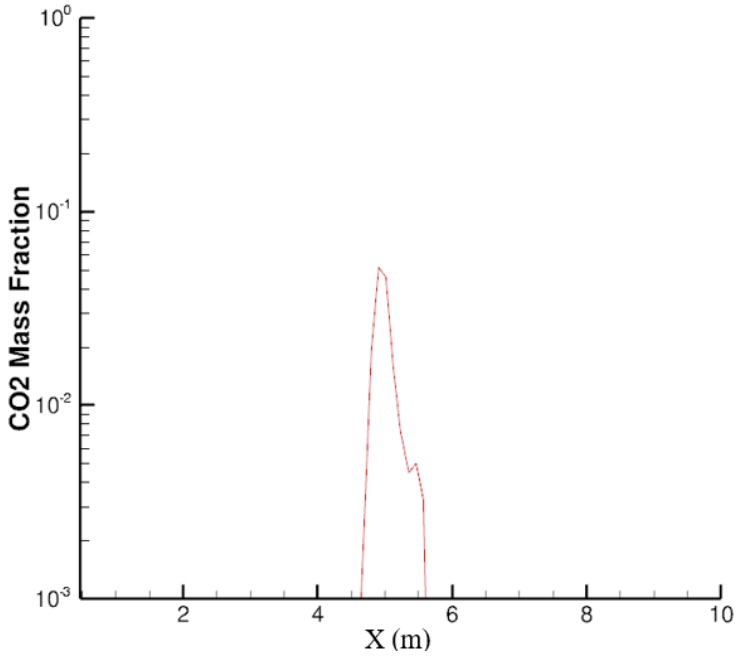

Figure 66. CO_2 Mass Fraction Distribution at 0.5 ms for 500 kg DAF

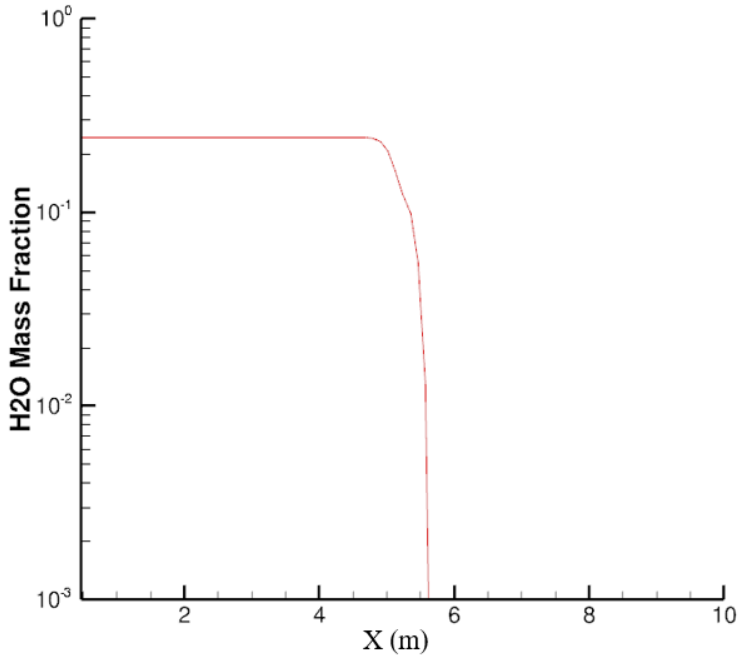

Figure 67. H_2O Mass Fraction Distribution at 0.5 ms for 500 kg DAF

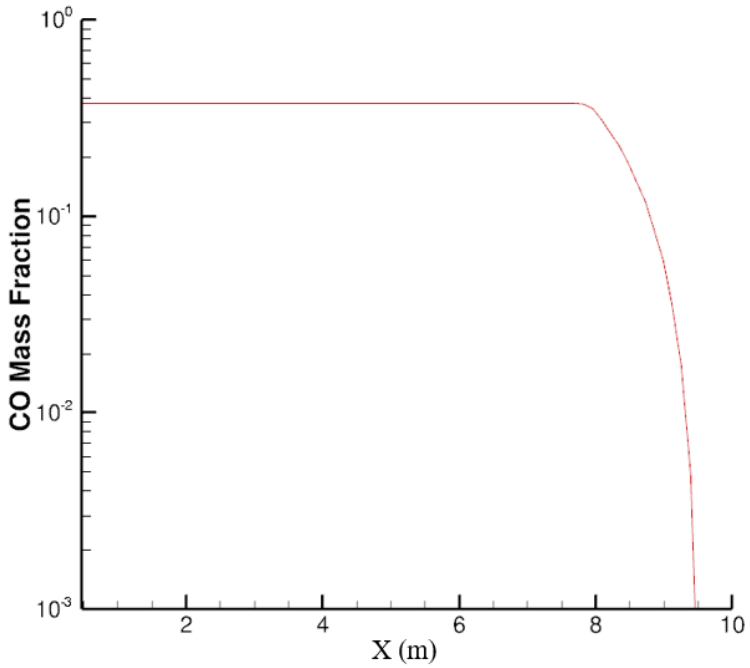

Figure 68. CO Mass Fraction Distribution at 1.25 ms for 500 kg DAF

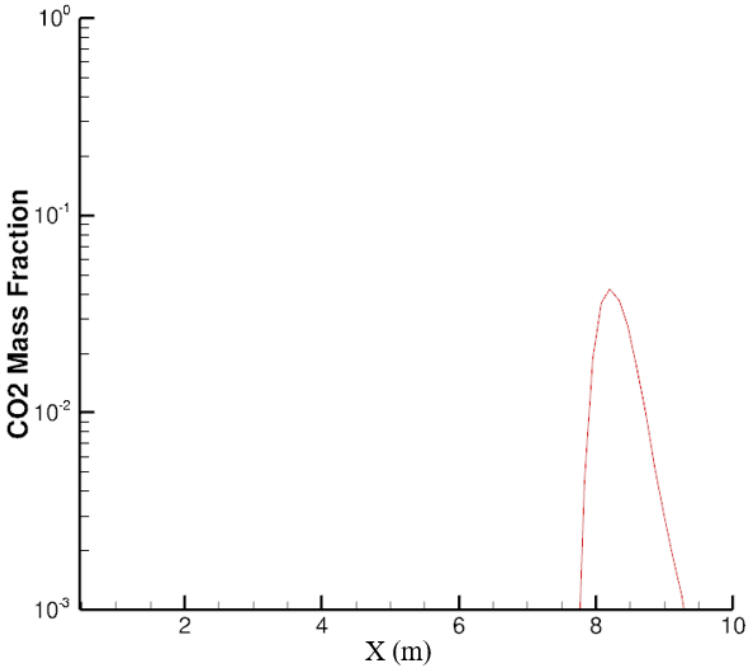

Figure 69. CO_2 Mass Fraction Distribution at 1.25 ms for 500 kg DAF

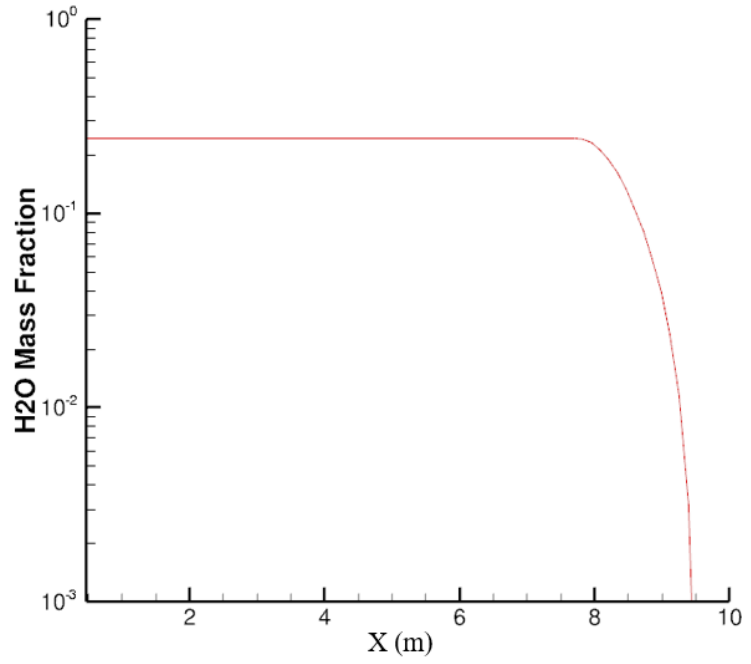

Figure 70. H_2O Mass Fraction Distribution at 1.25 ms for 500 kg DAF

1000 kg Runge-Kutta

The mass fraction distribution patterns for all three species were similar in the 1000 kg simulation to the 500 kg simulation (see Figure 71 to Figure 73). One of the slight differences was the distance the species could travel, but this difference was expected due to the results seen in the aerothermal distributions. A second slight difference between the two simulations was the 1000 kg results had additional mass fraction values found in its profile. This difference was another error caused by the physical results traveling faster than the numerical results.

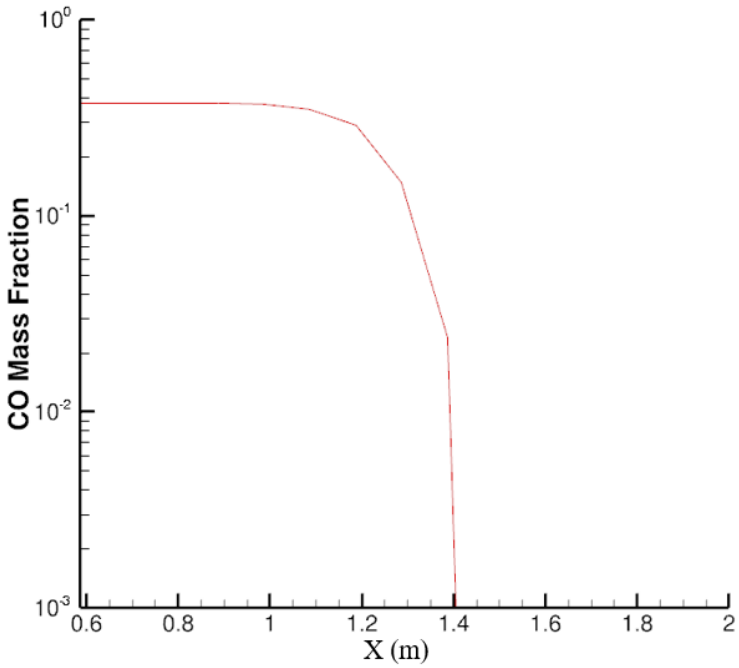

Figure 71. CO Mass Fraction Distribution at 44.1 μs for 1000 kg

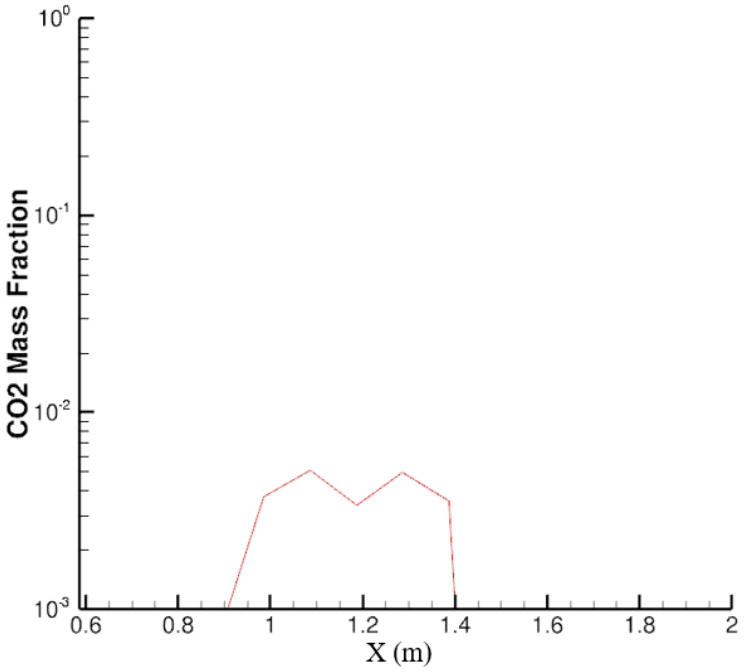

Figure 72. CO_2 Mass Fraction Distribution at 44.1 µs for 1000 kg

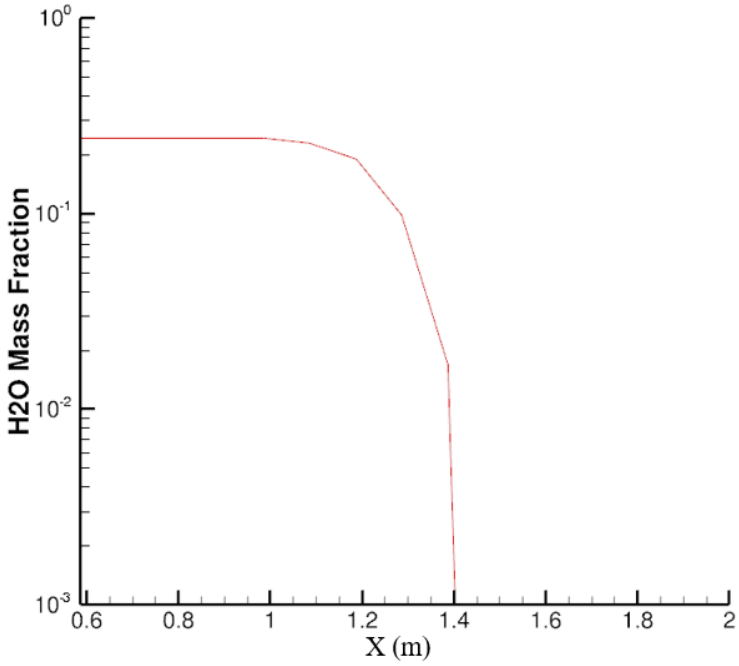

Figure 73. H_2O Mass Fraction Distribution at 44.1 µs for 1000 kg

Along with the addition of a second temperature profile at 0.225 milliseconds, the 1000 kg wave input simulation saw a spike in both CO and H_2O mass fractions (see

Figure 74 and Figure 75). The highest CO mass fraction tripled from the original 0.378 output from the explosive, while the H_2O mass fraction doubled its value. When the highest mass fraction value was ignored, the rest of the CO and H_2O mass fraction values followed the trend seen in the previous simulations.

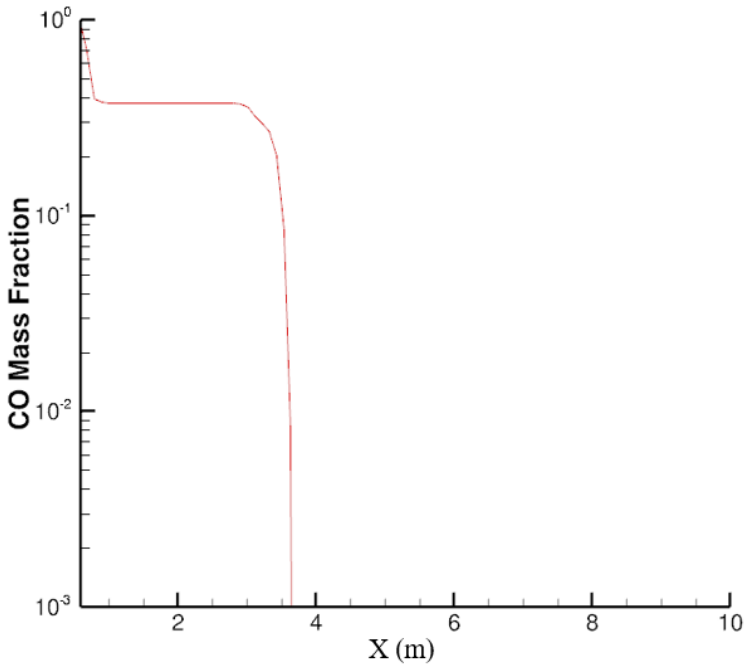

Figure 74. CO Mass Fraction Distribution at 0.225 ms for 1000 kg

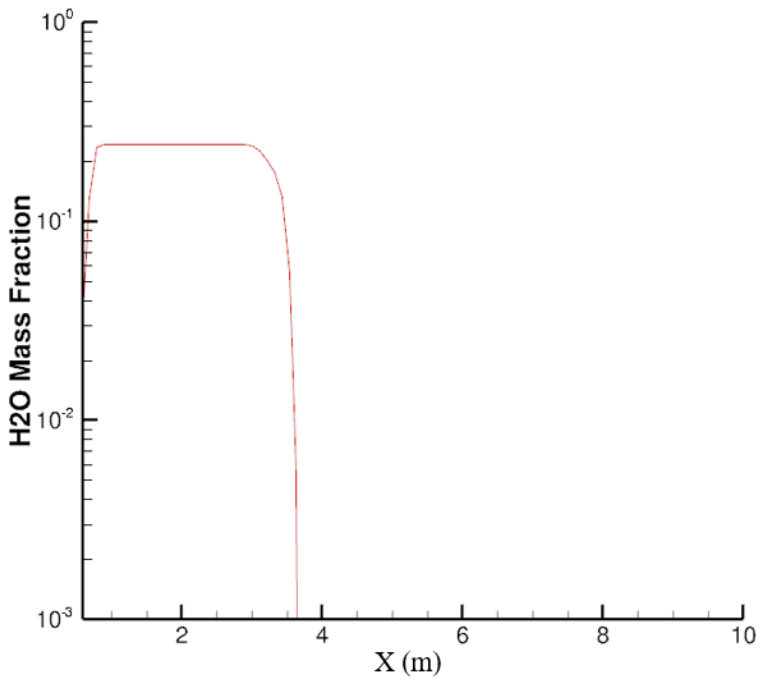

Figure 75. H_2O Mass Fraction Distribution at 0.225 ms for 1000 kg

The H_2O mass fraction highest value increased again, at the 0.25 millisecond time frame, to a value of 0.7, while the CO mass fraction value decreased. At the end of the wave simulation, the largest mass fraction value for CO and H_2O had decreased (see Figure 76 and Figure 78). However, the highest mass fraction values were still higher than the original 0.378 and 0.24 values. The overall trend of the mass fraction decreasing when traveling away from the origin was still maintained. The CO_2 mass fraction continued to increase over the 0.5 milliseconds (see Figure 77).

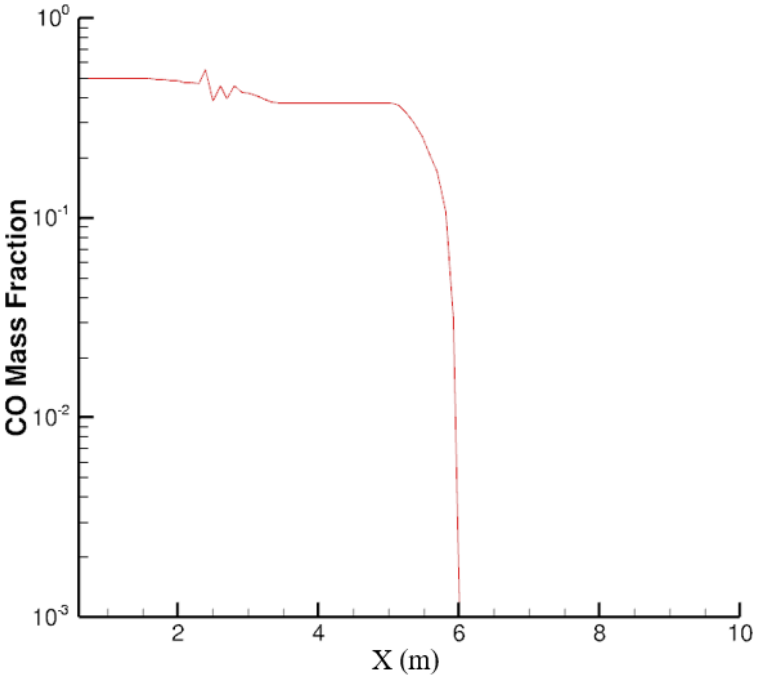

Figure 76. CO Mass Fraction Distribution at 0.5 ms for 1000 kg

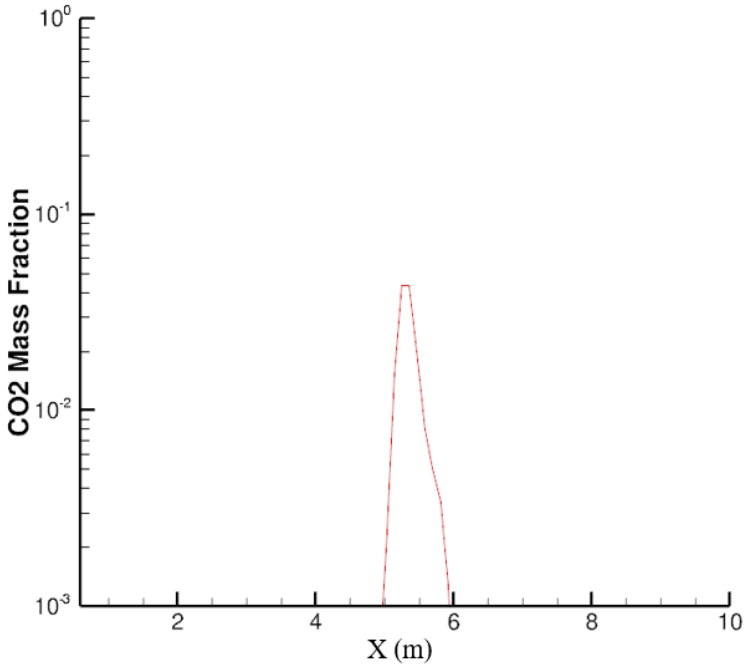

Figure 77. CO_2 Mass Fraction Distribution at 0.5 ms for 1000 kg

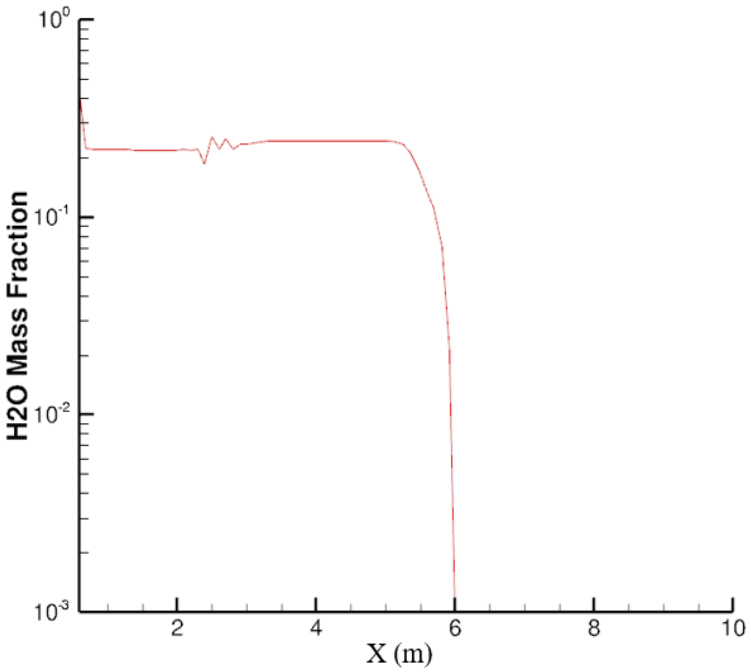

Figure 78. H_2O Mass Fraction Distribution at 0.5 ms for 1000 kg

2000 kg Runge-Kutta

The mass fraction distribution patterns, at the end of the explosion simulation, for all three species were similar in the 2000 kg simulation to both the 500 kg and 1000 kg simulations (see Figure 79 to Figure 81). The two slight differences between all three results were the same differences found between the 500 kg chemical results and the 1000 kg chemical results.

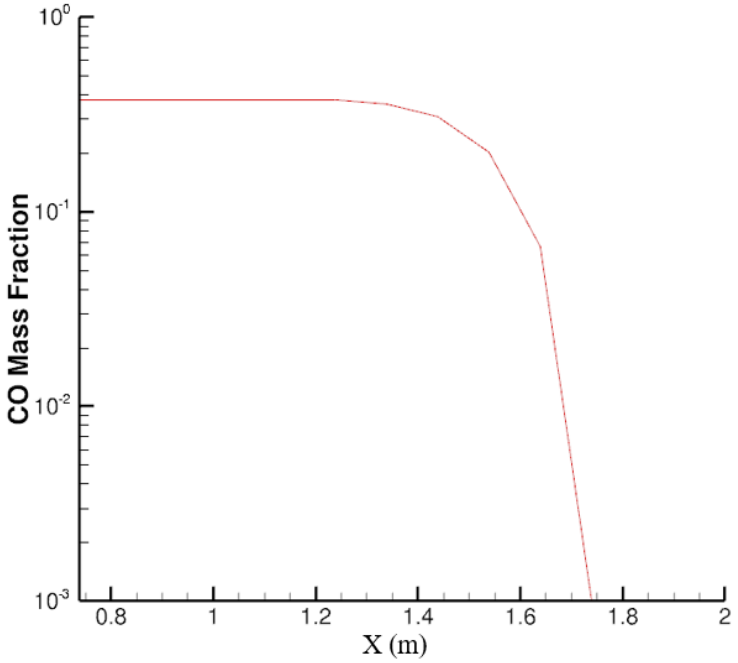

Figure 79. CO Mass Fraction Distribution at 55.6 μs for 2000 kg

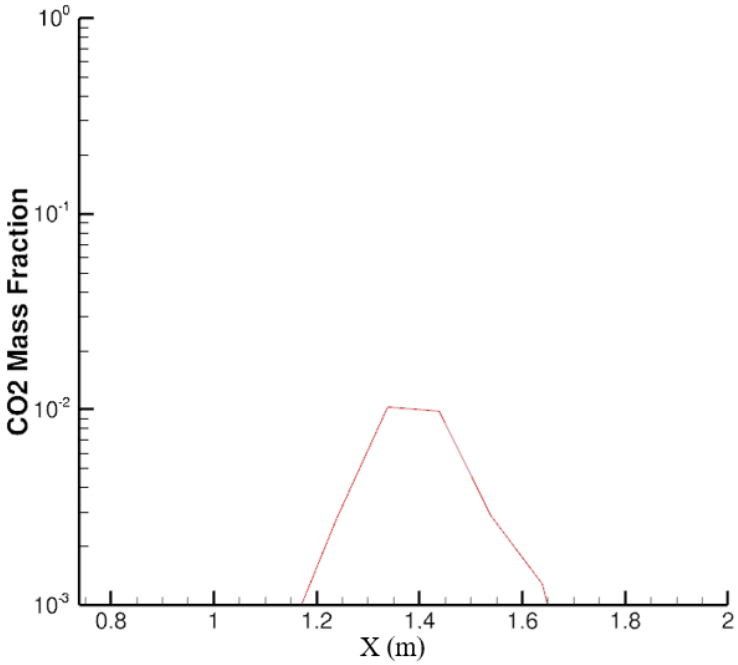

Figure 80. CO_2 Mass Fraction Distribution at 55.6 μs for 2000 kg

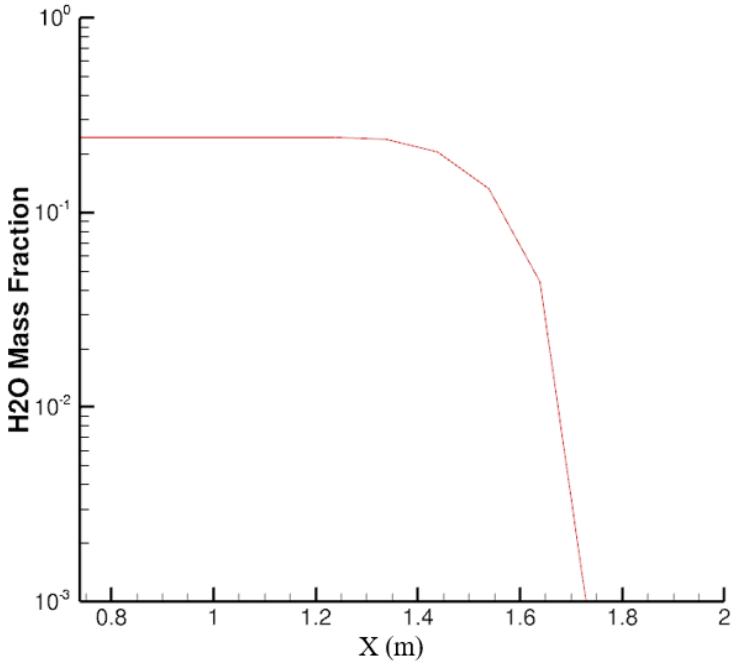

Figure 81. H_2O Mass Fraction Distribution at 55.6 μs for 2000 kg

The jump in CO and H_2O mass fraction values occurred 25 microseconds after the time it occurred in the 1000 kg simulation (see Figure 82 and Figure 83). Additionally, the CO mass fraction did not increase to as large a value as the one in the 1000 kg simulation, while the H_2O mass fraction increased to a larger value than the one in the 1000 kg simulation. When the spikes in mass fraction were ignored, the pattern of the mass fraction distributions remained the same as seen in all previous simulation results.

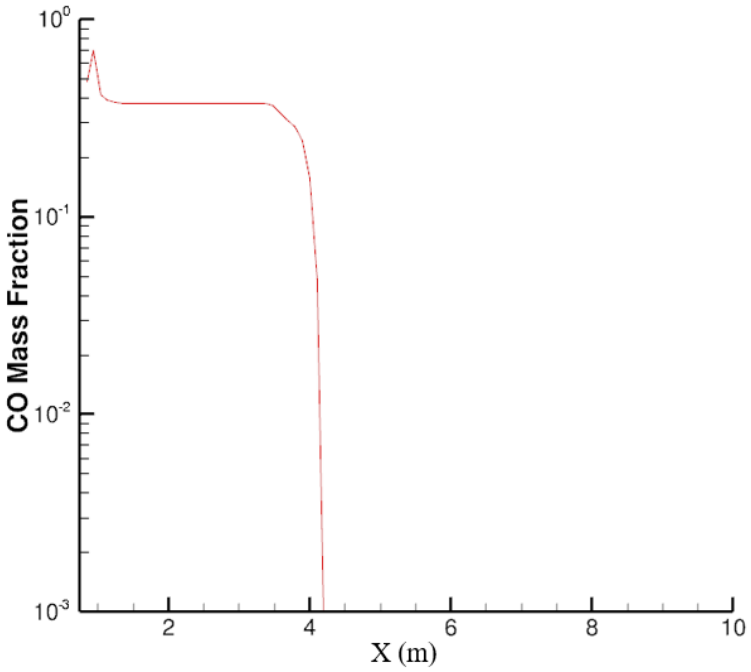

Figure 82. CO Mass Fraction Distribution at 0.25 ms for 2000 kg

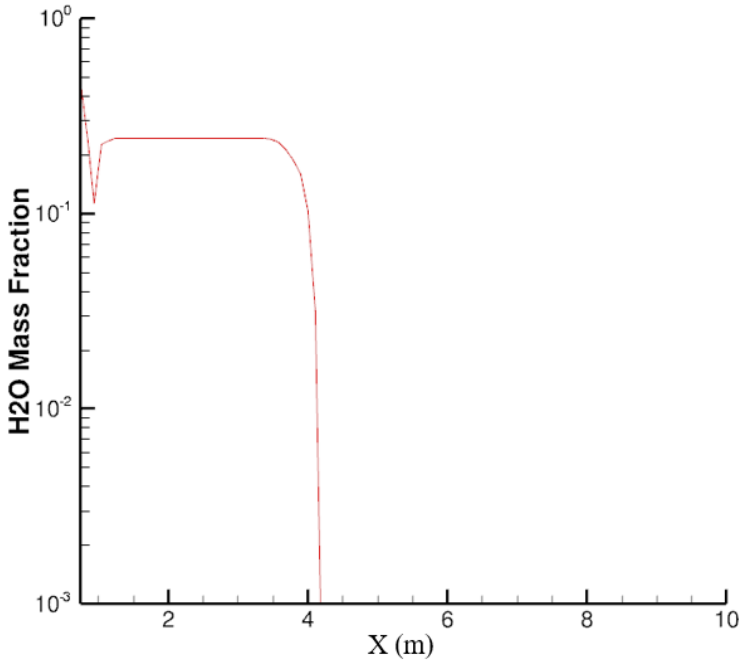

Figure 83. H2O Mass Fraction Concentration at 0.25 ms for 2000 kg

The H_2O mass fraction's highest value increased again, at the 0.275 millisecond time frame, to a value of 0.93, while the CO mass fraction value decreased. The overall trend of the mass fraction decreasing when traveling away from the origin was

maintained throughout the wave simulation. At 0.5 milliseconds, the shape of the mass fraction distribution was similar to the CO mass fraction distribution seen at the end of the explosion simulation, except that the 2000 kg mass fraction profile was a further distance from the center of the explosive (see Figure 84). The CO_2 mass fraction continued to increase over the 0.5 milliseconds, but the highest 2000 kg CO_2 mass fraction value remained lower than the 1000 kg CO_2 mass fraction value (see Figure 85). This difference was caused from the 1000 kg simulation having a higher CO mass fraction throughout the simulation compared the values seen in the 2000 kg simulation. The value of the highest H_2O mass fraction after 0.5 milliseconds remained above 0.9 (see Figure 86). The overall profile shapes found for CO and H_2O mass fractions in the 2000 kg simulation were the exact opposite shapes for CO and H_2O mass fractions in the 1000 kg simulation. This difference follows the difference in highest value spike behavior between the two.

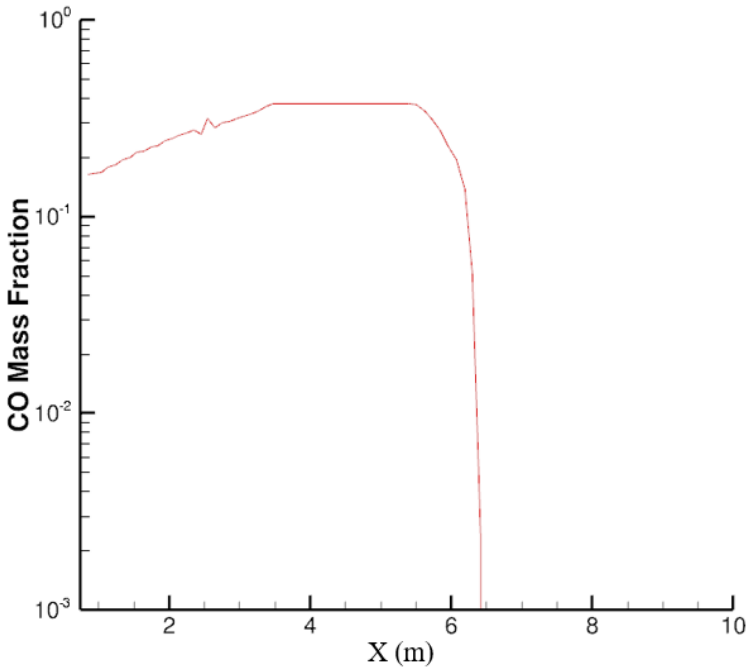

Figure 84. CO Mass Fraction Distribution at 0.5 ms for 2000 kg

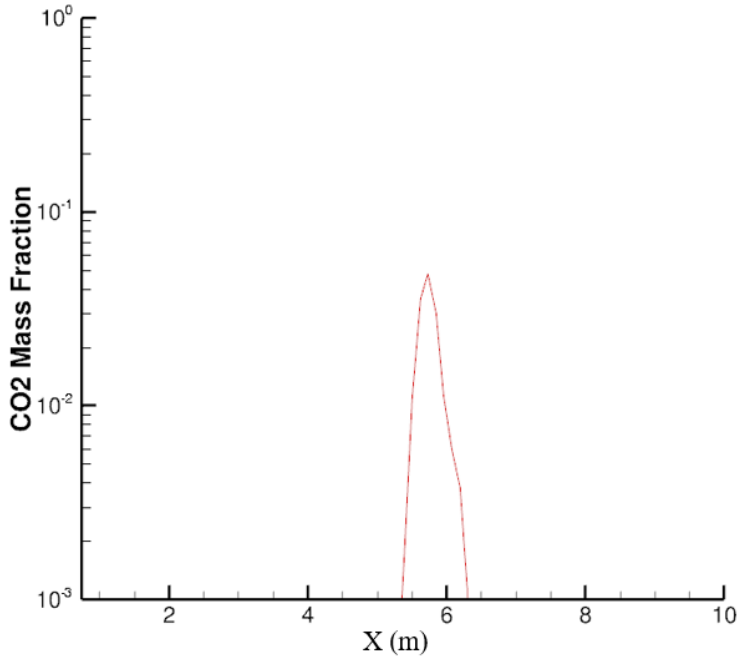

Figure 85. CO_2 Mass Fraction Distribution at 0.5 ms for 2000 kg

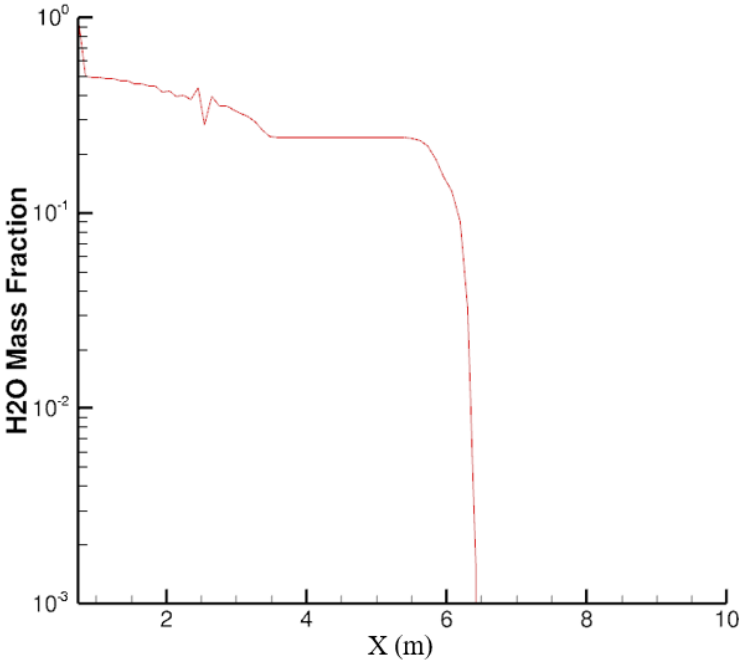

Figure 86. H_2O Mass Fraction Distribution at 0.5 ms for 2000 kg

Summary

This chapter presented the results from the thermophysics simulation of an RDX explosion. First, the chapter showed the changes in pressure, temperature, and Mach number distributions for both the explosion and wave simulations for 500 kg, 1000 kg, and 2000 kg during different time frames. Second, the chapter showed the chemical concentrations for CO, CO_2, and H_2O for the three different RDX masses.

V. Conclusions and Recommendations

Chapter Overview

This chapter addresses the conclusions and recommendations derived from this thesis research. The first section will be a summary of the aerothermal and chemical concentration results for the different RDX simulations. Finally, a discussion on future research is presented.

Summary

The objective of this thesis was to develop a framework for the simulation of aerothermal and chemical concentrations of an explosion, which was accomplished. Three different masses (500 kg, 1000 kg, and 2000 kg) of RDX were used in the simulation runs in VULCAN. Additionally, the 500 kg RDX went through two different solving schemes (Runge-Kutta and DAF).

Several problems were found during this research when running the wave simulation. The first problem dealt with the rapid spike in Mach number to an extremely high value before decreasing back down to a normal value range. The second problem identified was the high mass fraction values of CO and H_2O in the 1000 kg and 2000 kg simulations. These errors were caused from the physical model traveling faster than the numerical model. To correct this error, the time steps used in all explosion and wave simulations should be reduced to the lower end of the nanosecond timescale.

Differences were found between the Runge-Kutta and DAF aerothermal and chemical results for the 500 kg simulation. These differences were caused from the DAF

simulation only using one time step. To decrease or eliminate these differences, a dual time step needs to be utilized in future DAF simulations.

Suggestions for Further Research

This research showed a starting point for creating a model that could accurately simulate aerothermal and chemical concentrations of an RDX explosion. However, more work and research needs to be conducted to obtain aerothermal and chemical results that more accurately portray what is seen in the field. The first effort should be to decrease the time steps used in the simulation, so the errors found during this research would be fixed.

Given the short simulation run time, longer thermophysic simulations need to be accomplished. By extending the thermophysic simulation run time, conclusions could be obtained about how long it takes for there to be no significant chemical or aerothermal reactions after detonation. This knowledge in turn would help determine how long a remote sensor had to capture relevant data that could help with identifying the type and size of explosive used in an explosion. Additionally, the added run time results could provide further evidence of the trends already seen in the aerothermal and chemical results.

The assumptions (e.g. pure RDX used) used in this thesis for the thermophysic simulations need to be reduced. No weapon containing explosive material that is used today only contains the explosive. This thesis's thermophysics simulation needs to be taken to the next step to more accurately represent what is seen in battle. One major assumption that needs to be included is the use of casing (e.g. metal, plastic, etc.). The

type of casing used in a weapon has a significant impact on the aerothermal and chemical concentration results. By reducing the number of assumptions used in the simulation, the closer the results could get to matching real field data.

Finally, the aerothermal and chemical concentration results found from this research need to be taken to the next step before the data can be used to determine explosives remotely. The results data needs to be used to model the infrared signature. The infrared spectrum is one region where data sensing technology is useful in remote sensing. Additionally, previous work has proven that identification of explosives is possible using infrared. By converting the results from this research to infrared data, more information pertaining to the unique identification technique of explosives can occur.

Appendix A: Cheetah® Results

```
################################################################################
# #
# CHEETAH 7.0 SUMMARY SHEET #
# Energetic Materials Center #
# Lawrence Livermore National Laboratory #
# Email: cheetah@llnl.gov #
# Copyright 2012, Lawrence Livermore National Security #
# All Rights Reserved #
# #
################################################################################
################################################################################################
################################################################################################
Product library title: exp6.v7.0 $revision: 2264 $
Reactant library title: The Cheetah GUI XML file
COMPOSITION:
Heat of Molar
Name % wt % mol % vol formation weight TMD Formula
[cal/mol] [g] [g/cc]
rdx 100.00 100.00 100.00 1.6730e+004 222.117 1.816 c3h6n6o6
Molecular formula: c 3 h 6 n 6 o 6
Oxygen balance (by mass) = -21.609%
Heat of formation = 7.5323e+001 cal/g
################################################################################################
################################################################################################
Density = 1.8160 g/cc Mixture TMD = 1.8160 g/cc % TMD = 100.0000
CHAPMAN-JOUGUET CONDITION:
Pressure = 33.459 GPa
Volume = 0.421 cc/g
Density = 2.373 g/cc
Energy = 3.924 kJ/cc explosive
Temperature = 3434.4 K
Shock velocity = 8.862 km/s
Particle velocity = 2.079 km/s
Speed of sound = 6.783 km/s
Gamma = 3.263
CYLINDER DATA: % of standards
V/V0 Energy TATB PETN HMX CL-20 TNT
[kJ/cc] 1.83g/cc 1.76g/cc 1.89g/cc 2.04g/cc 1.64g/cc
1.00 -1.35 124 115 94 82 184
2.20 -7.26 141 115 93 80 176
4.40 -8.55 144 112 94 81 171
7.20 -9.01 144 110 94 81 169
10.00 -9.23 144 109 95 82 167
20.00 -9.60 143 108 95 82 164
50.00 -9.95 142 106 95 82 161
100.00 -10.16 142 105 95 83 159
200.00 -10.31 141 104 96 83 157
Chemistry "freeze" occurs at T = 1800.0 K and relative V = 2.104
Freeze command: freeze
```

PERFORMANCE:

Units	This explosive	TNT	TNT equivalence	
Total energy	kJ/cc	-1.0422e+001	-6.9959e+000	1.490 (per cc)
of detonation	kJ/g	-5.7391e+000	-4.2297e+000	1.357 (per gram)
Mechanical energy	kJ/cc	-1.0422e+001	-6.9766e+000	1.494 (per cc)
of detonation	kJ/g	-5.7391e+000	-4.2180e+000	1.361 (per gram)
Thermal energy	kJ/cc	0.0000e+000	< 0.1	N/A
of detonation	kJ/g	0.0000e+000	< 0.1	N/A
Heat	cal/g	2.1305e+003	3.4725e+003	0.614 (per gram)
of combustion	kJ/g	8.9138e+000	1.4529e+001	0.614 (per gram)

JWL FIT RESULTS:

E0 = -10.4221 kJ/cc

A = 2866.5584 GPa, B = 64.5706 GPa , C = 2.4688 GPa

R[1] = 6.8004, R[2] = 2.0000, omega = 0.5695

RMS fitting error = 0.997 %

Appendix B: MATLAB Code

```
% Thesis
% RDX calculations

% Info obtained from Cheetah 100% RDX
rhoTMD = 1.816; %g/cc
mw = 222.117; %g
OB = -21.609; %%
Pcj = 33.459; %GPa
Volumecj = 0.421; %cc/g
rhocj = 2.373; %g/cc
Tcj = 3434.4; %K
Dcj = 8.862; %km

% mass of explosive
prompt = 'What is the mass of the explosive?  ';
m = input(prompt)

% Calculations for grid info
% Volume_sphere = 4/3*pi*r^3
% Volume_hemisphere = 2/3*pi*r^3
Volumeexp = Volumecj*(m*1000); %cc
r_in = (Volumeexp/(2/3*pi))^(1/3) %cm

% Calculations for amount of time inlet should be on
mdot = rhocj*(Dcj*1000*100)*pi*r_in^2; %g/s
t = (m*1000)/mdot %sec
```

Appendix C: VULCAN Explosion Input File

```
$****************** Beginning of general control data ******************$
$---------- Dimensionality of problem ----------$
AXISYM              (TWOD=2D, AXISYM=Axisymmetric, THREED=3D)
$------------------------ Input control data ------------------------$
GRID                    0.0   (0=plot3d->3d ; plot2d->2d/axi, 1=plot3d->all)
  500kggridshort.grd
GRID FORMAT         3.0   (1=sb fmt, 2=sb unf, 3=mb fmt, 4=mb unf)
RESTART IN                (input restart file name to follow)
  500kg.restart
RESTART OUT         0.0   (output restart file name to follow)
  500kg.restart
$------------------------ Output control data ------------------------$
PLOT ON                 3.0   (1=sb fmt, 2=sb unf, 3=mb fmt, 4=mb unf)
32 BIT BINARY               (write plot files as 32 or 64 bit binary)
PLOT FUNCTION       5.0   (no. of plot function names)
  DENSITY
  MACH NO.
  PRESSURE
  TEMPERATURE
  MASS FRACTION
  8
  N N2 O O2 NO CO CO2 H2O
PLOT PLANAR         0.0
OUTPUT TIME HISTORY  10.0
  500kg_time
$-------------------------- Equation set data -------------------------$
GLOBAL VISCOUS            (solve N-S equations using global algorithm)
$---------- Gas and thermodynamic data ----------$
GAS/THERMO MODEL     1.0   (0=calorically perfect, 1=thermally perfect)
$------------------------ Chemistry model data ------------------------$
CHEMISTRY MODEL      1.0   (0=frozen, 1=finite rate, 3=CARM, 4=ISAT)
IMPLICIT CHEMISTRY   1.0   (1=analytic jacobian, 2=numerical jacobian)
$-------------------- Chemical species information --------------------$
NO. OF CHEMICAL SPECIES    8.0
  gas_mod.ceranski
N       N2         O     O2        NO    CO    CO2   H2O
0.0     0.7686    0.0    0.2314   0.0    0.0    0.0     0.0
NO. OF CHEMICAL REACTIONS  7.0
  reac_mod.ceranski
$---------------------- Reference condition data ----------------------$
NONDIM                      2.0   (1=static conditions, 2=total conditions)
MACH NO.                    0.01
TOTAL TEMPERATURE     288.15
```

```
TOTAL PRESSURE          101325.0
PRANDTL NO.             0.72
SCHMIDT NO.             0.22
TURB. PRANDTL NO.       0.90
TURB. SCHMIDT NO.       0.50
$---------------------- Turbulence model data ----------------------$
TURB. MODEL
  MENTER-BSL
TURB. INTENSITY     1.0e-02
TURB. VISC. RATIO   1.0e-01
$------------------ Runge-Kutta Integration Control ------------------$
NSTAGE              3.0   (no. of Runge-Kutta stages)
0.333333333333  0.5  1.0
RESMTYP             0.0   (residual smoothing model)
$---------------------- Boundary and cut control ---------------------$
BLOCKS              1.0   (no. of blocks in input grid)
BCGROUPS            4.0   (no. of boundary condition groups)
BCOBJECTS           0.0   (no. of boundary condition objects)
FLOWBCS             4.0   (no. of boundary conditions)
CUTBCS              0.0   (no. of cut connectivity conditions)
TIME HISTORY I/O    1.0   (no. of time history spatial windows)
BLOCK CONFIG.       1.0   (no. of lines of block configurations input)
BLK  I-VISC J-VISC K-VISC (N, T, or F)  TURB  REAC  PLOT  REGION
  1        T        T        N                    Y       Y       Y       1
$----------------- Solution Methodology for Region 1 -----------------$
SOLVER  LDFSS  KAPPA  LIMITER  LIMITER COEFFICIENT  ENT FIX (U)  ENT FIX (U+a)
  E/A             3 3 3   5  5  5    2.000   2.000  2.000   0.0  0.0  0.0  0.0  0.0  0.0
FMGLVLS    NITSC  NITSM  NITSF    1ST-ORDER LEVELS   REL RES   ABS RES
  1                          100                 0              -99.0      -99.0
M.G. CYCLE   COARSE GRIDS   DQ SMOOTH   DQ COEFF   DAMP MEAN   DAMP TURB
   I                  0              0.25          0.25           1.0           1.0
TURB CONVECTION   DT RATIO   NON EQUIL   POINT IMP   COMP MODEL   CG WALL BC
    2ND                1.0         10.0          Y           N           STW
SCHEME TIME-STEP IT-STATS MIN-CFL VAR-CFL CFL-VALUES VISC-DT IMP-BC REG-REST
 R-K      DELTAT    10         0.5       Y          3          Y       N       N
  1           100     1000
3.50e-07   3.50e-07  3.50e-07
!******************** End of general control data ********************!
BC GROUP:  NAME          TYPE       OPTION
                EXP-IN        AFIXED    PHYSICAL
N   N2      O   O2  NO  CO    CO2 H2O    Rhot  Uvel  Vvel   Wvel    Tt     Turb Int   Vis Ratio
0.0 0.378 0.0 0.0 0.0 0.378 0.0 0.244  2373.0  0.0  8862.0  0.0  3434.4  0.01       0.1
                OUTFLOW   EXTRAP   PHYSICAL
                BOTTOM     AXCIL     PHYSICAL
                LEFT          SWALL    PHYSICAL
```

BC NAME	BLK	FACE	PLACE	IND1	BEG	END	IND2	BEG	END	IN-ORD
EXP-IN	1	J	MIN	I	MIN	MAX	K	MIN	MAX	0
OUTFLOW	1	J	MAX	I	MIN	MAX	K	MIN	MAX	0
BOTTOM	1	I	MAX	J	MIN	MAX	K	MIN	MAX	0
LEFT	1	I	MIN	J	MIN	MAX	K	MIN	MAX	0

TIM NAME	BLK	DIR1	BEG	END	DIR2	BEG	END	DIR3	BEG	END
EXPLOSION	1	I	MIN	MAX	J	MIN	MAX	K	MIN	MAX

Appendix D: VULCAN Wave Input File

```
$****************** Beginning of general control data ******************$
$---------- Dimensionality of problem ----------$
AXISYM              (TWOD=2D, AXISYM=Axisymmetric, THREED=3D)
$------------------------ Input control data ------------------------$
GRID                    0.0   (0=plot3d->3d ; plot2d->2d/axi, 1=plot3d->all)
  500kggridshort.grd
GRID FORMAT         3.0   (1=sb fmt, 2=sb unf, 3=mb fmt, 4=mb unf)
RESTART IN                (input restart file name to follow)
  500kg.restart
RESTART OUT         0.0   (output restart file name to follow)
  500kgwall.restart
$------------------------ Output control data ------------------------$
PLOT ON                 3.0   (1=sb fmt, 2=sb unf, 3=mb fmt, 4=mb unf)
32 BIT BINARY               (write plot files as 32 or 64 bit binary)
PLOT FUNCTION       5.0   (no. of plot function names)
  DENSITY
  MACH NO.
  PRESSURE
  TEMPERATURE
  MASS FRACTION
  8
  N N2 O O2 NO CO CO2 H2O
PLOT PLANAR         0.0
OUTPUT TIME HISTORY  5000.0
  500kg_time
$------------------------- Equation set data -------------------------$
GLOBAL VISCOUS            (solve N-S equations using global algorithm)
$---------- Gas and thermodynamic data ----------$
GAS/THERMO MODEL     1.0   (0=calorically perfect, 1=thermally perfect)
$------------------------ Chemistry model data ------------------------$
CHEMISTRY MODEL      1.0   (0=frozen, 1=finite rate, 3=CARM, 4=ISAT)
IMPLICIT CHEMISTRY   1.0   (1=analytic jacobian, 2=numerical jacobian)
$---------- Chemical species information ----------$
NO. OF CHEMICAL SPECIES    8.0
  gas_mod.ceranski
N       N2         O     O2        NO    CO    CO2   H2O
0.0     0.7686    0.0    0.2314   0.0    0.0    0.0     0.0
NO. OF CHEMICAL REACTIONS  7.0
  reac_mod.ceranski
$---------- Reference condition data ----------$
NONDIM                      2.0   (1=static conditions, 2=total conditions)
MACH NO.                    0.01
TOTAL TEMPERATURE     288.15
```

```
TOTAL PRESSURE          101325.0
PRANDTL NO.             0.72
SCHMIDT NO.             0.22
TURB. PRANDTL NO.       0.90
TURB. SCHMIDT NO.       0.50
$---------------------- Turbulence model data ----------------------$
TURB. MODEL
  MENTER-BSL
TURB. INTENSITY     1.0e-02
TURB. VISC. RATIO   1.0e-01
$------------------ Runge-Kutta Integration Control ------------------$
NSTAGE              3.0   (no. of Runge-Kutta stages)
0.333333333333  0.5  1.0
RESMTYP             0.0   (residual smoothing model)
$---------------------- Boundary and cut control ---------------------$
BLOCKS              1.0   (no. of blocks in input grid)
BCGROUPS            4.0   (no. of boundary condition groups)
BCOBJECTS           0.0   (no. of boundary condition objects)
FLOWBCS             4.0   (no. of boundary conditions)
CUTBCS              0.0   (no. of cut connectivity conditions)
TIME HISTORY I/O    1.0   (no. of time history spatial windows)
BLOCK CONFIG.       1.0   (no. of lines of block configurations input)
BLK  I-VISC J-VISC K-VISC (N, T, or F)  TURB  REAC  PLOT  REGION
  1        T        T        N                    Y       Y       Y       1
$----------------- Solution Methodology for Region 1 -----------------$
SOLVER  LDFSS  KAPPA  LIMITER  LIMITER COEFFICIENT  ENT FIX (U)  ENT FIX (U+a)
  E/A           3 3 3   5 5 5    2.000   2.000 2.000   0.0 0.0 0.0  0.0 0.0 0.0
FMGLVLS    NITSC  NITSM  NITSF    1ST-ORDER LEVELS   REL RES   ABS RES
  1                          100000                0              -99.0      -99.0
M.G. CYCLE   COARSE GRIDS   DQ SMOOTH   DQ COEFF   DAMP MEAN   DAMP TURB
   I                  0          0.25        0.25          1.0          1.0
TURB CONVECTION   DT RATIO   NON EQUIL   POINT IMP   COMP MODEL   CG WALL BC
    2ND               1.0        10.0           Y           N          STW
SCHEME TIME-STEP IT-STATS MIN-CFL VAR-CFL CFL-VALUES VISC-DT IMP-BC REG-REST
 R-K      DELTAT    10         0.5       Y           3           Y       N       Y
  1           100     1000
2.50e-07   2.50e-07  2.50e-07
!******************** End of general control data ********************!
BC GROUP:  NAME          TYPE       OPTION
               EXP-IN        SWALL    PHYSICAL
               OUTFLOW    EXTRAP   PHYSICAL
               BOTTOM      AXCIL     PHYSICAL
               LEFT          SWALL    PHYSICAL

BC  NAME  BLK  FACE  PLACE  IND1  BEG   END  IND2  BEG   END  IN-ORD
EXP-IN        1       J      MIN       I     MIN   MAX   K     MIN   MAX      0
```

OUTFLOW	1	J	MAX	I	MIN	MAX	K	MIN	MAX	0
BOTTOM	1	I	MAX	J	MIN	MAX	K	MIN	MAX	0
LEFT	1	I	MIN	J	MIN	MAX	K	MIN	MAX	0

TIM NAME	BLK	DIR1	BEG	END	DIR2	BEG	END	DIR3	BEG	END
EXPLOSION	1	I	MIN	MAX	J	MIN	MAX	K	MIN	MAX

Bibliography

[1] C. Hughes, "Battle for Mosul: 'Mad Max' suicide squads are blown to oblivion on the road to hell," *Mirror Online*, 23-Oct-2016.

[2] M. Bennett, "BBC - History - World Wars: War and Technology Gallery," 2011. [Online]. Available: http://www.bbc.co.uk/history/worldwars/war_tech_gallery_04.shtml#one. [Accessed: 30-Oct-2016].

[3] C. Elachi and J. Van Zyl, *Introduction to the Physics and Techniques of Remote Sensing, Second Edition*. John Wiley & Sons.

[4] J. A. Orson, "Collection of Detonation Signatures and Characterization of Spectral Signatures," Masters Thesis, Air Force Institute of Technology, 2000.

[5] S. Tzu, *The Art of War*. Sheba Blake Publishing, 2015.

[6] V. Dunn, *Safety and Survival on the Fireground, Second Edition*. PennWell Corporation, 2015.

[7] "GLOBAL INTEGRATED ISR ENDURING CAPABILITIES," 2014. [Online]. Available: https://doctrine.af.mil/DTM/dtmisroperations.htm. [Accessed: 23-Oct-2016].

[8] P. W. Cooper, *Explosives Engineering*. Wiley-VCH, Inc., 1996.

[9] S. Bastea L. E. Fried, K. R. Glaesemann, W. M. Howard, I-F. W. Kuo, P. C. Souers, and P. A. Vitello, "Cheetah 7.0 User's Manual." 2012.

[10] A. Creese, "Vulcan 6.3.0 User's Manual." National Aeronautics and Space Administration, 2014.

[11] C. L. Mader, *Numerical Modeling of Explosives and Propellants, Third Edition*. Taylor and Francis Group, 2008.

[12] W. E. Baker, *Explosions in Air*. University of Texas Press, 1973.

[13] A. L. Kuhl, J.-C. Leyer, A. A. Borisov, and W. A. Sirignano, "Dynamic Aspects of Detonations," *Progress in Astronautics and Aeronautics*, vol. 153, 1993.

[14] A. L. Kuhl, J.-C. Leyer, A. A. Borisov, and W. A. Sirignano, "Dynamic Aspects of Explosion Phenomena," *Progress in Astronautics and Aeronautics*, vol. 154, 1993.

[15] Y. B. Zel'dovich and Y. P. Raizer, *Physics of Shock Waves and High-Temperature Hydrodynamic Phenomena*. Academic Press, Inc., 1970.

[16] K. C. Gross, "Phenomenological Model for Infrared Emissions from High-Explosive Detonation Fireballs," PhD Dissertation, Air Force Institute of Technology, 2007.

[17] E. L. Dereniak and G. D. Boreman, *Infrared Detectors and Systems*. John Wiley & Sons, 1996.

[18] J. M. Gordon, "Shock Wave Dynamics of Novel Aluminized Detonations and Empirical Model of Temperature Evolution from Post-Detonation Combustion Fireballs," Air Force Institute of Technology, Wright-Patterson AFB OH, 2011.

[19] K. J. Vanden and P. D. Orkwis, "Comparison of Numberical and Analytical Jacobians," *AIAA*, vol. 34, no. 6, 1996.

[20] A. Mazaheri, P. A. Gnoffo, C. O. Johnston, and B. Kleb, "LAURA Users Manual: 5.5." National Aeronautics and Space Administration, Langley Research Center, 2013.

[21] R. T. Biedron, J-R Carlson, J. M. Derlaga, P. A. Gnoffo, D. P. Hammond, W. T. Jones, B. Kleb, E. M. Lee-Rausch, E. J. Nielsen, M. A. Park, C. L. Rumsey, J. L. Thomas, and W. A. Wood, "FUN3D Manual: 12.9." National Aeronautics and Space Administration, Langley Research Center, 2016.

REPORT DOCUMENTATION PAGE

Form Approved
OMB No. 074-0188

1. REPORT DATE *(DD-MM-YYYY)*	**2. REPORT TYPE**	**3. DATES COVERED** *(From – To)*
24-03-2017	Masters Thesis	March 2016 – March 2017

TITLE AND SUBTITLE

Simulation of Aerothermal and Chemical Concentrations for an RDX Explosion

5a. CONTRACT NUMBER

5b. GRANT NUMBER

5c. PROGRAM ELEMENT NUMBER

6. AUTHOR(S)

Ceranski, Alison M., Captain, USAF

5d. PROJECT NUMBER

5e. TASK NUMBER

5f. WORK UNIT NUMBER

7. PERFORMING ORGANIZATION NAMES(S) AND ADDRESS(S)
Air Force Institute of Technology
Graduate School of Engineering and Management (AFIT/ENY)
2950 Hobson Way, Building 640
WPAFB OH 45433-8865

8. PERFORMING ORGANIZATION REPORT NUMBER

AFIT-ENY-MS-17-M-250

9. SPONSORING/MONITORING AGENCY NAME(S) AND ADDRESS(ES)
AGENCY: National Air and Space Intelligence Center
ADDRESS:
PHONE and EMAIL: DSN 672-6238, jonathan.mautz@us.af.mil
ATTN: POC Jonathan Mautz

10. SPONSOR/MONITOR'S ACRONYM(S)

NASIC

11. SPONSOR/MONITOR'S REPORT NUMBER(S)

12. DISTRIBUTION/AVAILABILITY STATEMENT
DISTRUBTION STATEMENT A. APPROVED FOR PUBLIC RELEASE; DISTRIBUTION UNLIMITED.

13. SUPPLEMENTARY NOTES
This material is declared a work of the U.S. Government and is not subject to copyright protection in the United States.

14. ABSTRACT
The aerothermal and chemical concentrations of an RDX explosive were simulated using VULCAN, a NASA owned and operated program. The Chapman-Jouguet properties from an RDX explosion were obtained using pure RDX at theoretical maximum density in Cheetah®. The values obtained from Cheetah® were used to determine the inner radius of the grid used in VULCAN as well as the required time to run the explosive's products into the grid. Four different axisymmetric simulations were run in VULCAN. The simulation of 500 kg, 1000 kg, and 2000 kg of RDX using the Runge-Kutta solving scheme were three of those four simulations. The last simulation was of a 500 kg RDX using Diagonalized Approximation Factorization solving scheme. The aerothermal and chemical results showed several errors. One error was a massive spike in Mach numbers found in all four simulations. The second error was the addition of CO and H_2O in both the 1000 kg and 2000 kg simulations. However, these errors occurred due to the numerical results not being able to keep up with the physical results in the simulation. In the future, small time steps will be required to keep these errors from occurring. The research successfully developed a framework for simulating the aerothermal and chemical concentrations for an explosion.

15. SUBJECT TERMS
RDX explosive, aerothermal and chemical concentration simulation

16. SECURITY CLASSIFICATION OF:			**17. LIMITATION OF ABSTRACT**	**18. NUMBER OF PAGES**	**19a. NAME OF RESPONSIBLE PERSON**
a. REPORT	**b. ABSTRACT**	**c. THIS PAGE**			Robert Greendyke, AFIT/ENY
U	**U**	**U**	**UU**	116	**19b. TELEPHONE NUMBER** *(Include area code)* (937) 255-6565, ext xxxx (NOT DSN) (Robert.greendyke@afit.edu)

Standard Form 298 (Rev. 8-98)
Prescribed by ANSI Std. Z39-18